A SEARCH FOR LONG-LIVED, CHARGED, SUPERSYMMETRIC PARTICLES USING IONIZATION WITH THE ATLAS DETECTOR

BRADLEY AXEN

September 2016 – Version 0.59

The dissertation of Bradley Axen, titled *A Search for Long-Lived, Charged, Supersymmetric Particles using Ionization with the ATLAS Detector,* is approved:

Chair Date

Date

Date

University of California, Berkeley

Usually a quotation.

Dedicated to.

ABSTRACT

How to write a good abstract:

https://plg.uwaterloo.ca/~migod/research/beck00PSLA.html

PUBLICATIONS

Some ideas and figures have appeared previously in the following publications:

Put your publications from the thesis here. The packages `multibib` or `bibtopic` etc. can be used to handle multiple different bibliographies in your document.

optional quotation

ACKNOWLEDGEMENTS

Put your acknowledgements here.

And potentially a second round.

CONTENTS

LIST OF FIGURES

LIST OF TABLES

LISTINGS

ACRONYMS

SM Standard Model

CERN European Organization for Nuclear Research

SUSY Supersymmetry

MSSM Minimal Supersymmetric Model

cMSSM Constrained MSSM

pMSSM Phenomenological MSSM

LSP Lightest Supersymmetric Particle

LHC Large Hadron Collider

ATLAS A Toroidal LHC ApparatuS

CMS Compact Muon Solenoid

ALICE A Large Ion Collider Experiment

LHCb Large Hadron Collider beauty experiment

LEP the Large Electron Positron collider

PS Proton Synchrotron

PSB Proton Synchrotron Booster

SPS Super Proton Synchrotron

SCT silicon microstrip

TRT Transition Radiation Tracker

LAr liquid argon

EM electromagnetic

RPC Resistive Plate Chamber

TGC Thin Gap Chamber

MDT Monitored Drift Tube

CSC Cathode Strip Chamber

ToT time over threshold

RoI Region of Interest

LCW	local cluster weighted
MIP	minimally ionizing particle
IP	impact parameter
EPJC	European Physical Journal C
JES	jet energy scale
LLP	Long-Lived Particle
CR	Control Region
NLO	next-to-leading order
NLL	next-to-leading logarithmic
PDF	parton distribution function
ISR	initial state radiation
RMS	root mean square
IBL	Insertible B-Layer
CP	Combined Performance
MDT	Monitored Drift Tube
RF	radiofrequency
HLT	high level trigger
QCD	quantum chromodynamics
BSM	beyond the Standard Model

1 INTRODUCTION

As of 2012, with the discovery of the Higgs boson, the SM provides a complete and validated description of the interactions of fundamental particles. It describes a remarkable range of phenomena given its simple foundation, and has been successful in explaining high energy physics in all experiments yet performed. However, it is clear that the picture is incomplete: without a description of gravity or an explanation for dark matter, an extension is necessary to describe new physics at higher energies. These deficiencies motivate a wide range of experiments that search for new physics. The LHC provides the highest energy approach, seeking to discover unobserved particles or interactions in high energy proton collisions.

The experiments at the LHC have searched for a variety of new phenomena in the years since collisions began in 2010. A major focus of these searches has been on Supersymmetry (SUSY), an extension to the SM which has the potential to ameliorate many of its shortfalls. None of the searches have found evidence of new physics, and between them they have begun to rule out a number of models that would predict new particles at the TeV scale. This motivates searches for more exotic signals that may have been missed, using analysis techniques tuned specifically for those signals.

This dissertation presents a search for Long-Lived Particles (LLPs) using the 13 TeV collisions collected during 2015 at the LHC. Charged LLPs are predicted to exist in a subset of SUSY models, and have dramatically different detector signatures than both SM processes and other SUSY models. This search focuses on isolating that unique signature using ionization in the ATLAS detector.

Part I provides the theoretical context and motivation for a search for new physics in high energy collisions. Chapter 2 outlines the basic framework of the SM and describes its particles and interactions. It also discusses the limitations of the SM that motivate the existence of new physics. Chapter 3 discusses a possible solution to the shortcomings of the SM, the theory of Supersymmetry, and the ways that it can generate LLP.

Part II discusses the structure of the accelerator complex that provides collisions as well as the experiment that measures them. Chapter 4 summarizes the design and performance of the LHC and the features of the proton-proton collisions it produces. Chapter 5 then discusses the components of the ATLAS detector and how they can be used to measure the particles produced in LHC collisions. Chapter 6 describes the algorithms used to reconstruct physics particles and processes from the electronic signals in the detector.

Part III presents a measurement of calorimeter response, an important component of event reconstruction used in many physics analyses. Chapter 7 describes a direct, in situ measurement of calorimeter response using isolated hadrons, and investigates the modeling of that response in simulation. Chapter 8 uses those measurements to construct a correction for the energy of jets in simulation, the JES, and to estimate an uncertainty for that correction.

Part IV details the search for LLPs. It begins with a discussion of the simulation of LLPs in ATLAS, focusing on the detector signatures and how they vary with the properties of those particles in Chapter 9. Then Chapter 10 discusses the strategy of the search and the requirements used to select LLPs and to reject SM backgrounds. Chapter 11 explains a method for predicting the background from SM processes, and shows a validation of the technique. Chapter 12 describes the systematic uncertainties on both the selection efficiency for signal events and the background method. The results of the search are presented in Chapter 13.

PART I

THEORETICAL CONTEXT

You can put some informational part preamble text here.

2 STANDARD MODEL

The SM of particle physics seeks to explain the symmetries and interactions of fundamental particles. The SM provides predictions in particle physics for interactions up to the Planck scale (10^{19} GeV). It has been tested by several generations of experiments and has been remarkably successful; no significant deviations from its predictions have been found.

The theory itself is a quantum field theory grown from an underlying symmetry, $SU(3) \times SU(2) \times U(1)$, that generates all of the interactions consistent with experimental observations[1]. These interactions are referred to as the Strong, Weak, and Electromagnetic forces. Each postulated symmetry necessitates the existence of an associated conserved charge, which appear as properties of the observed particles in nature.

Although this model has been very predictive, the theory is incomplete; for example, it is not able to describe gravity or astronomically observed dark matter. These limitations suggest a need for an extension or new theory to describe physics at higher energies.

2.1 ACTION AND THE LAGRANGIAN

Originally, both action and the Lagrangian were constructed for an integral reformulation of the laws of classical mechanics, which is a purely mathematical step: any differential equation can be re-expressed in terms of an integral equation. The Lagrangian, $\mathcal{L}$, is classically given by the difference of kinetic energy and potential energy. The Lagrangian is defined this way so that the action, $\mathcal{S}$, given by

$$\mathcal{S}[\mathbf{q}(t)] = \int_{t_1}^{t_2} \mathcal{L}(\mathbf{q}, \dot{\mathbf{q}}, t)\, dt \tag{1}$$

returns the classical equations of motion when one requires it to be stationary in the path, $\mathbf{q}(t)$. This formulation of classical mechanics is extremely useful in calculations, and generalizes beautifully to cover all types of physics.

In particular, with the development of quantum mechanics in the twentieth century, the concepts of action and the Lagrangian were found to generalize to more complicated physics for which the classical laws do not hold. Quantum mechanics and quantum field theory can be constructed from the action, using the path integral formulation, by assuming that a particle undergoes all possible paths $\mathbf{q}(t)$ with an imaginary phase given by $e^{i\mathcal{S}[\mathbf{q}(t)]/\hbar}$. This reduces to classical mechanics in the limit as $\hbar$ goes to zero, as all paths for which the action is not stationary interfere with each other so as to cancel their contributions. Because

1 excluding gravity

the wavefunction of a particle can be completely determined through the action and the action depends only on the Lagrangian, the Lagrangian itself is sufficient to describe the physics governing the particle.

So, in both classical and quantum mechanics, the Lagrangian of a system contains everything there is to know about the system, apart from initial conditions. Thus, the most natural way to express that a system has a certain symmetry is to require that the Lagrangian is invariant under a corresponding symmetry transformation. This makes the Lagrangian the central piece of the discussion of gauge invariance; the mathematical representation of gauge invariance is that a gauge transformation on the appropriate components of the Lagrangian returns an identical Lagrangian. That is,

$$\mathcal{L}(\psi, D^{\mu}) = \mathcal{L}(U\psi, D'^{\mu}) \tag{2}$$

where ψ is the wavefunction and D^{μ} is the derivative operator, both of which may transform under a symmetry operation. There are a number of immediate and surprisingly powerful consequences of requiring that the Lagrangian is invariant under a symmetry operation.

2.2 GAUGE INVARIANCE AND FORCES

The simplest possible relativistic, quantum Lagrangian for matter particles is the free Dirac Lagrangian, which describes a relativistic fermion in a vacuum.

$$\mathcal{L} = i\bar{\psi}\partial\!\!\!/\psi - m\bar{\psi}\psi \tag{3}$$

A fermion denotes a particle with spin-1/2, and the kinematic term ($i\bar{\psi}\partial\!\!\!/\psi$) is chosen to correctly describe the free propagation of a fermionic particle with mass m. This equation is clearly invariant under a global $U(1)$ transformation, that is changing ψ by a complex phase has no effect. The derivative operator commutes with a constant phase factor, and wherever ψ appears its complex conjugate also appears so as to cancel out the change of phase. However, the Lagrangian as written is not invariant under the local $U(1)$ symmetry postulated for the SM, which can be written as $U = e^{i\alpha(x)}$. The piece of the Lagrangian involving a derivative will return an extra term that will break the invariance of the Lagrangian under this transformation:

$$\begin{aligned}
\mathcal{L}' &= i(\bar{\psi}U^{\dagger})\partial\!\!\!/(U\psi) - m(\psi U^{\dagger})(U\psi) \\
&= i(\bar{\psi}U^{\dagger})U(\partial\!\!\!/ - \gamma^{\mu}\partial_{\mu}\alpha(x))\psi - m(\psi U^{\dagger})(U\psi) \\
&= i\bar{\psi}\partial\!\!\!/\psi - m\bar{\psi}\psi - i\gamma^{\mu}\partial_{\mu}\alpha(x)\bar{\psi}\psi \\
&= \mathcal{L} - i\gamma^{\mu}\partial_{\mu}\alpha(x)\bar{\psi}\psi \\
&\neq \mathcal{L}
\end{aligned}$$

So, in order to enforce the required symmetry, the typical approach is to construct a covariant derivative, that is to add a term to the derivative operator so that the unwanted term in $\mathcal{L}'$ is exactly canceled. A generic form for such a derivative is given by

$$D^\mu = \partial^\mu - iqA^\mu$$

where at this point A^μ is an arbitrary field that transforms under the $U(1)$ operator and q is a scaling factor. Adding this component to the above Lagrangian gives

$$\mathcal{L}' = i(\bar{\psi}U^\dagger)U(\partial\!\!\!/ - \gamma^\mu\partial_\mu\alpha(x) - iq\gamma^\mu A'_\mu)\psi - m(\psi U^\dagger)(U\psi) \tag{4}$$

$$\mathcal{L}' = \mathcal{L} + \gamma^\mu(-i\partial_\mu\alpha(x) - iqA'_\mu + iqA_\mu)\bar{\psi}\psi \tag{5}$$

and because the transformation of A^μ is unspecified, $\mathcal{L} = \mathcal{L}'$ whenever

$$A'_\mu = A_\mu - \frac{1}{q}\partial_\mu\alpha(x)$$

The above procedure demonstrated that beginning with the Lagrangian for a free fermion and imposing a local $U(1)$ symmetry required the existence of a vector field A^μ, and specified its transformation under the $U(1)$ gauge group. The additional term in the derivative can be expanded to form a completely separate term in the Lagrangian,

$$\mathcal{L} = i\bar{\psi}\partial\!\!\!/\psi - m\bar{\psi}\psi - (q\bar{\psi}\gamma^\mu\psi)A^\mu \tag{6}$$

and in this form it is clear that the A^μ term has the exact form of the electromagnetic interaction. That is, this is the Lagrangian which reproduces the relativistic form of Maxwell's equations for a particle interacting with an electromagnetic field. It is natural to also introduce a term to the Lagrangian at this point to describe the free propagation of the vector A field, where the propagation of a vector field has the form of

$$-\frac{1}{16\pi}F^{\mu\nu}F_{\mu\nu} \quad \text{with} \quad F_{\mu\nu} = \partial_\mu A_\nu - \partial_\nu A_\mu \tag{7}$$

This then also describes the electromagnetic interactions in a vacuum and the propagation of a photon. This component of the Lagrangian should also potentially include a mass term, but such a term would not be gauge invariant and so must be excluded. The photon is an example of a gauge boson, a spin-1 particle required to exist by a gauge symmetry of the Lagrangian and one that corresponds to a force. In summary, requiring the $U(1)$ symmetry was enough to recover all of electromagnetism and to predict the existence of a photon in the SM.

The interaction term that was placed into the Lagrangian by this procedure can be conveniently summarized with Feynman diagrams, which diagrammatically represent a transition from an initial state to a final state. The contribution

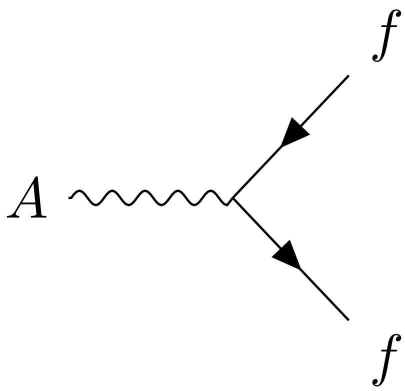

Figure 1: A Feynman diagram representing the interaction of the A field with a generic fermion, f.

of all diagrams that start with the same initial state and end with the same final state must be summed, but more complicated diagrams can be built by linking together the simplest versions. A diagram that corresponds to the above term, $(q\bar{\psi}\gamma^{\mu}\psi)A^{\mu}$, is shown in Figure 1, for an interaction with a generic fermion.

2.2.1 SU(2) × U(1) AND THE ELECTROWEAK FORCE

The full picture of the electroweak section of the SM is more complicated than the simplified explanation of the electromagnetic piece described above. In practice, it is necessary to consider the entire $SU(2) \times U(1)$ symmetry together, but the procedure is the same. Enforcing the symmetry on the Lagrangian requires the introduction of a covariant derivative, this time with four total distinct terms, one for each of the generators of $SU(2) \times U(1)$. The result is a series of terms in the Lagrangian which describe the interaction of a fermion with four vector (spin-1) fields, the W_1, W_2, W_3, and B fields. These fields can mix in the quantum sense, and linear combinations form the W^+, W^-, Z, and A fields that are considered actual particles in the SM[2].

2.2.2 $SU(3)$ AND THE STRONG FORCE

The same procedure can be applied starting with the $SU(3)$ symmetry requirement, where eight additional fields must be introduced, one for each of the generators of $SU(3)$. The resulting Lagrangian describes quantum chromodynamics (QCD) and predicts the existence of eight gauge bosons known collectively as gluons. The complexity of the interactions of those eight gluons leads to surprising phenomena, discussed in Section 2.5.2.

2 These states are the actual particles because they are mass eigenstates, but the full explanation of this will have to wait for the discussion of the Higgs mechanism.

2.3 NOETHER'S THEOREM, CHARGES, AND MATTER

Another direct consequence of the symmetries stipulated in the SM are a series of conserved quantities, Noether charges, named after the mathematician and physicist Emmy Noether. The charges arise as a direct consequence of Noether's theorem, which can be informally stated as

> *For every symmetry of the Lagrangian, there exists a corresponding physical quantity whose value is conserved in time.*

Or, stated another way, symmetries of the Lagrangian mathematically require the conservation of specific quantities taken from the Lagrangian. This relationship can also be thought of as operating in the other direction, the existence of a conserved charge can be shown to generate the symmetry in the Lagrangian. This theorem is actually quite striking in a somewhat unexpected relation between simple geometric symmetries and physically observable conservation laws. For example, the theorem connects the translation invariance of the Lagrangian in space to the conservation of momentum and the translation invariance in time to the conservation of energy.

In the context of the SM, the required symmetries of $U(1) \times SU(2) \times SU(3)$ correspond to the charges that are considered properties of all elementary particles. The most familiar of these properties is the electric charge, Q, which is one of the conserved quantities of $SU(2) \times U(1)$. The remaining pieces of $SU(2) \times U(1)$ correspond to weak isospin, T and T_3, where T has only non-negative values and T_3 can be positive and negative. The $SU(3)$ symmetry is generated by the three colors of QCD, red, green, and blue, each with a corresponding opposite color, anti-red, anti-green, and anti-blue.

The matter in the observable universe consists of a collection of particles which carry these charges, in addition to spin and mass. The particles typically thought of as matter are all fermions: particles with spin-$1/2$. All of the fermions belong to one of two groups, quarks and leptons, and one of three generations. Each of the generations have similar properties but significantly different masses; the particles in consecutive generations have increasing mass. Quarks are distinguished from leptons in that they carry color charge, in addition to electric charge and weak isospin. The particles in the SM are summarized in Figure 2, and the matter particles are the twelve types of fermions displayed on the left side of the graphic.

2.3.1 QUARKS

The three generations of quarks each consist of a quark with electric charge $+2/3$ and one with charge $-1/3$. They are called up and down, charm and strange, and top and bottom respectively, and these are referred to as the quark flavors. Although Figure 2 only shows these six flavors, there is a unique particle for each combination of the three colors and flavor. And each quark has an anti-particle with the opposite electric and color charge values.

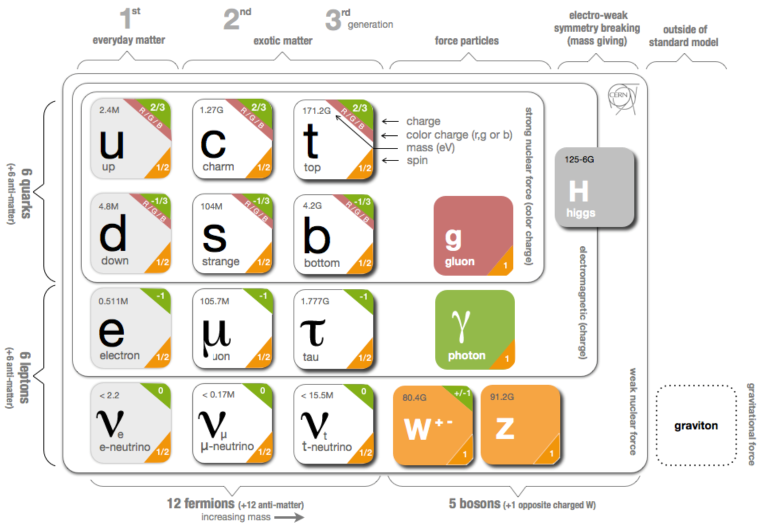

Figure 2: The particle content of the SM.

However, individual quarks are never observed in nature, but instead form color-neutral bound states. This is a consequence of interaction of gluons with color charge called confinement, discussed in Section 2.5.2. One way to form a color neutral combination is a bound state of three quarks with three different color charges, called a baryon. Baryons are the most common type of quark configuration in conventional matter, and include protons and neutrons. The other common configuration is a bound state of a quark and an anti-quark, called a meson, where the two quarks have opposite colors. Although there is no direct conservation law resulting from the symmetries of the SM Lagrangian, an accidental symmetry results in the approximate conservation of baryon number, B, where baryons have $B = 1$ and mesons have $B = 0$. That is, no interactions are present which directly[3] alter baryon number

2.3.2 LEPTONS

The remaining fermions, the leptons, do not carry color charge. Each generation contains an electrically charged lepton, the electron, muon, and tau, and an electrically neutral lepton called a neutrino. For the charged leptons, the flavors are mass eigenstates, with the masses listed in Figure 2. The flavors of the neutrinos, on the other hand, are not mass eigenstates: their propagation in quantum superpositions of flavor states leads to oscillations between different flavors. The absolute masses of the neutrinos are not currently known, but the phenomenon of oscillations shows that they have three different mass values. Another accidental symmetry leads to an approximate[4] conservation of lepton number L, the differ-

3 There are combinations of interactions which can modify either B or L individually, but the combination $B - L$ appears to be conserved in the SM.

4 See footnote 3.

ence in the number of leptons and anti-leptons; again there are no interactions present in the SM which directly alter lepton number.

2.3.3 CHIRALITY

All of the fermions described above have two possible values of the magnitude of weak isospin, T, either 0 or $1/2$. The fermions with $T = 0$ are called right-handed, while those with $T = 1/2$ are called left-handed. Because T is the charge corresponding to the weak force, right-handed particles do not interact with the weak gauge bosons in the same way that neutral particles do not interact with photons. For left-handed fermions, each of the quark and lepton generations have one particle with $T_3 = -1/2$ and one with $T_3 = +1/2$. The neutrinos have $T_3 = +1/2$, while the charged leptons have $T_3 = -1/2$. Similarly, the positively charged quarks have $T_3 = +1/2$ and the negatively charged quarks have $T_3 = -1/2$. Because the right-handed neutrinos would have no charge of any type, it is not clear if they exist at all.

2.4 HIGGS MECHANISM AND MASS

The description of the electroweak forces above left out an important part of the observed nature of the electroweak force. Many physical experiments observed phenomena corresponding to the interaction of the weak bosons that were best explained if they had significant masses. But as mentioned before, massive bosons would break the gauge invariance of the Lagrangian. A large mass for the W and Z bosons would explain the relative weakness of their interactions compared to the electromagnetic field. The Lagrangian's discussed above did not include a mass term for the gauge bosons, and in fact such a term would not be allowed by the requirement of gauge invariance. This was a significant problem for the SM, and the symmetry of the electroweak sector would have to be broken in order to allow for non zero masses for some of the gauge bosons.

One mechanism to allow for this spontaneous symmetry breaking is the Higgs mechanism, which posits the existence of an additional scalar field. It begins with a $SU(2) \times U(1)$ invariant Lagrangian of the form

$$\mathcal{L} = |D_\mu \phi|^2 - \frac{1}{2}\mu^2 \phi^+ \phi - \frac{1}{4}\lambda(\phi^+ \phi)^2 \tag{8}$$

where ϕ is the new scalar field with two components and, importantly, μ^2 is negative. This leads to a minimum value of the field at a non-zero value of ϕ, specifically where

$$\langle \phi \rangle = \frac{1}{\sqrt{2}} \begin{pmatrix} 0 \\ v \end{pmatrix} \quad \text{with} \quad v = \frac{2\mu^2}{\lambda} \tag{9}$$

Expanding the original Lagrangian about its expectation value in terms of the perturbation H,

$$\langle\phi\rangle = \frac{1}{\sqrt{2}}\begin{pmatrix}0\\ v+H\end{pmatrix} \tag{10}$$

gives potential terms in the Lagrangian like

$$\mathcal{L}_H = -\frac{1}{2}m_H^2 H^2 - \sqrt{\frac{\lambda}{2}}m_H H^3 - \frac{1}{4}\lambda H^4 \tag{11}$$

where $m_H = \sqrt{2}\mu$. The form of this Lagrangian shows that the non-zero expectation value of the ϕ field has introduced a massive scalar field H with self interaction terms. It has an additional important consequence on the description of the gauge bosons, through the expansion of the term involving the covariant derivative:

$$|D_\mu\phi|^2 \supset \frac{1}{8}\left(g^2(W_{1\mu}W_1^\mu + W_{2\mu}W_2^\mu) + (g'B_\mu - gW_3\mu)^2\right) \tag{12}$$

where the W_i and B fields are the original $SU(2) \times U(1)$ gauge fields mentioned previously. The above equation can be rearranged using linear combinations of the fields to from mass terms for the gauge bosons, and the mass eigenstates are exactly the $W^\pm$, Z, and A fields. Only the A field, corresponding to the photon, results in a zero mass, and the remaining three fields acquire masses. Because the previously introduced Lagrangian, written in terms of ϕ, was clearly gauge invariant, this resulting configuration must also be gauge invariant.

This is the Higgs mechanism, where the introduction of a gauge invariant scalar field with a non-zero expectation value can generate masses for the gauge bosons without violating the underlying symmetries. The particle that is associated with the perturbations of this field, H, is called the Higgs boson, and is said to generate the masses of the remaining bosons because the vacuum expectation value introduces mass-like terms for each of the bosons. The resulting masses are listed in Figure 2. Because this mechanism was so successful in describing the observed properties of the W and Z bosons, it has been considered part of the SM for decades, although the actual Higgs boson was only recently observed in 2012, confirming the theory.

The Higgs mechanism is also responsible for generating the masses of the fermions. The original mass terms that were listed in the Lagrangian for fermions are replaced with Yukawa coupling terms, which introduce interactions between the ϕ field and the fermions. Like with the gauge bosons, the non-zero expectation value of the field yields mass terms, and the expansion about that value introduces interaction terms between the fermions and the Higgs boson. The masses are different between each fermion because each has a different Yukawa coupling, which results in the masses listed in Figure 2.

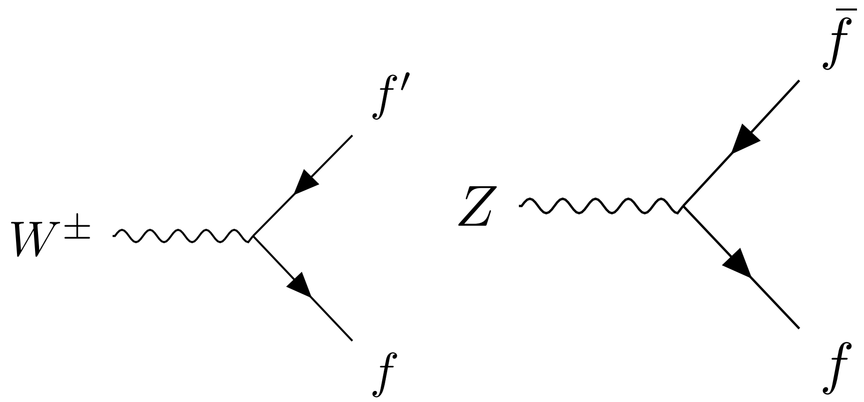

Figure 3: The Feynman diagrams representing the decays of the W and Z bosons to fermions. Here f indicates a generic fermion, $\bar{f}$ its antiparticle, and f' the partner of that fermion in the same generation.

2.5 PHENOMENOLOGY

The SM Lagrangian described above contains all of the information necessary to describe particle physics through the path integral formulation. However, a tremendous amount of complexity emerges from that description because of the diverse allowed interactions between the ensemble of particles in the SM. A qualitative understanding of the phenomenology produced by those interactions is immensely helpful in understanding the analysis of particle physics.

2.5.1 ELECTROWEAK PHYSICS

The masses of the W and Z bosons result in significantly different processes for the weak fields than the electromagnetic field, despite their interactions being similar before symmetry breaking. The massless photon is stable, and can propagate in a vacuum, resulting in the familiar long range interactions of electromagnetism. The W and Z bosons, however, are unstable, as they have large enough masses to decay to fermions, such as the decays shown in Figure 3. For this reason, photons can be observed directly, while the other bosons are sufficiently short-lived that they can only be measured from their decay products.

Because the electroweak bosons interact with both quarks and leptons, they are responsible for the production of leptons in proton-proton collisions. Z bosons and photons produce pairs of opposite sign, same flavor leptons. W bosons, on the other hand, produce a single lepton and the corresponding neutrino.

2.5.2 STRONG PHYSICS

The phenomenology of the strong sector differs significantly from the weak sector because the gluons are massless but color charged. Because of this, gluons can interact with each other, and contributions from multiple gluon interactions lead to a significant growth in the strength of the field at low energies. The dependence of the field strength on the energy scale is described by renormalization, and in QCD the coupling is only small at high energies. Below approximately 1 GeV, the strength of those interactions results in confinement: the interactions are so strong that when quark-antiquark pairs separate, the fields between them generate additional quarks to form color neutral bound states. Above around the GeV scale, the interactions of quarks become perturbative, similar to the electroweak fields; this phenomenon is known as asymptotic freedom.

At lower energies, however, the strength of the strong interaction is so significant that the interactions of color-charged particles create additional particles until they form neutral bound-states. This process is known as hadronization, and explains why no quarks are observed isolated in nature: they all form bound states of hadrons like protons, neutrons, and pions. The hadronization process can produce a significant number of particles, so that a single energetic quark recoiling against another quark can generate a cascade of dozens of hadrons. Because of the initial boost of such an energetic configuration, the resulting hadrons are collimated, and conical spray of particles often referred to as a jet.

2.5.3 PROTON-PROTON COLLISIONS

Proton-proton collisions are a convenient way to generate high energy interactions to probe the SM and to search for new physics. At the energies that will be discussed in this analysis, the substructure of the protons is very important to the description of the resulting interactions. At lowest order, protons are composed of two up quarks and one down quark, but this description is incomplete. The actual bound state includes a chaotic sea of additional quarks and gluons, each of which carries a variable fraction of the proton's energy. When a proton-proton collision takes place, it is these constituents that interact with each other, resulting in a highly variable collision energy even when the proton-proton energy is consistent.

The fraction of the energy carried by each constituent varies moment to moment, but can be modelled probabilistically by PDFs. These are difficult to predict theoretically, as the QCD calculations are extremely complex, and instead are measured in hard-scattering experiments. They are usually represented by how often a given type of particle carries a fraction x of the total proton energy. Those fraction change significantly with the scale of the interaction, Q; the PDFs of proton-proton collisions at both $Q^2 = 10$ GeV^2 and $Q^2 = 10^4$ GeV^2 are shown in Figure 4.

2.6 LIMITATIONS

Despite the great success of the relatively simple SM in describing such a broad range of emergent phenomena, it is clear that the picture it presents of the interactions of fundamental particles is incomplete. The SM contains concerning coincidences that suggest a more ordered underlying substructure that is not ex-

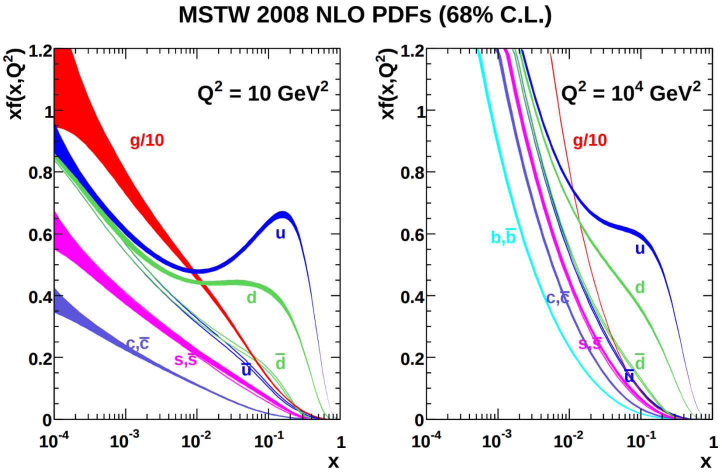

Figure 4: The PDFs for proton-proton collisions at $Q^2 = 10$ GeV ^{2} and $Q^2 = 10^4$ GeV ^{2}. Each shows the fraction of particles which carry a fraction x of the total proton energy at the specified scale [1].

pressed in the current form. It also fails to explain a number of cosmological measurements of the nature of matter in the universe. These limitations suggest the need for new, beyond the Standard Model (BSM) physics that would provide a more complete description at higher energies.

2.6.1 THEORETICAL CONCERNS

There have been no successful integrations of the SM's description of the electroweak and strong forces with the description of gravity, and it is still unclear how to account for the effects of gravity at the Planck scale of approximately 10^{19} GeV, where its interactions are as strong as the remaining forces. The Planck scale is an important cutoff for the SM, as it is clear that the SM must break down somewhere between the current highest energy tests of the SM, around 1 TeV, and the Planck scale.

One example of this is the Higgs mass, which is determined in the SM by a sum of it's bare mass and the interactions in the vacuum with all massive particles. As there must be new physics at the Planck scale to describe gravity, some of those corrections would include contributions at a scale seventeen orders of magnitude above the mass of the Higgs. Either the bare mass of the Higgs boson precisely cancels those contributions to leave a remainder seventeen orders of magnitudes smaller, or a new theory exists at a lower scale the shields the Higgs mass from those terms. A theory where such a unlikely cancellation of free parameters occurs is called fine-tuned, and one that is free from such cancellations is called natural. Theories where the mass of the Higgs is natural are usually preferred, as the suggest an underlying, coherent structure. The enormous difference in scales between the weak scale (including the Higgs mass), and the Planck scale, is often referred to as the hierarchy problem.

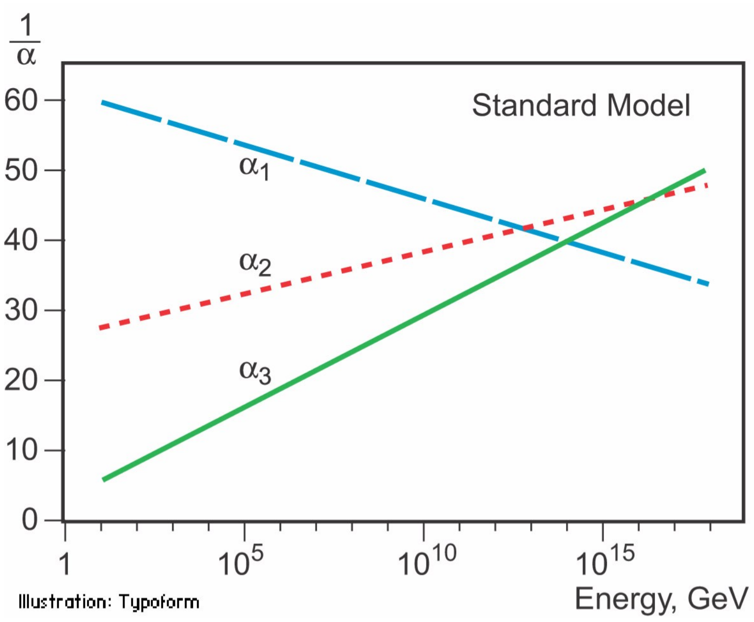

Figure 5: An approximation of the running of the coupling constants in the SM up to the Planck scale [2].

There is also a compelling argument that the $SU(3) \times SU(2) \times U(1)$ gauge structure of the SM might originate from a single, unified gauge theory. For example, it is possible to represent that gauge structure as a $SU(5)$ gauge group with only a few inconsistencies with the current implementation. This unification is suggested by the scaling of the coupling constants for each of the forces under renormalization; they come close to converging to a single value at higher energies, as seen in Figure 5. An additional correction to the scaling of the coupling constants from new physics above the TeV scale could cause them to merge into a single value at high energies.

2.6.2 COSMOLOGICAL OBSERVATIONS

The SM contains a symmetry in the description of matter and antimatter that is not reflected in cosmological observations. The processes of the standard model create or remove matter and antimatter in equal amounts, so a universe that begins with an equal quantity of each should result in a universe with an approximate[5] balance of matter and antimatter. However, cosmological observations of the relative amount of each type clearly show that the directly observable mass of the universe is overwhelmingly made of matter. As this difference is largely a difference in the generation of baryons and anti-baryons, this discrepancy is often referred to as the baryogenesis problem.

A number of astrophysical observations of large scale gravitational interactions suggest the presence of a significant amount of non-luminous matter that interacts with the normal matter only gravitationally. The first evidence of this

5 There are some processes in the standard model which can result in a small imbalance of matter and antimatter, but not at the scale observed cosmologically.

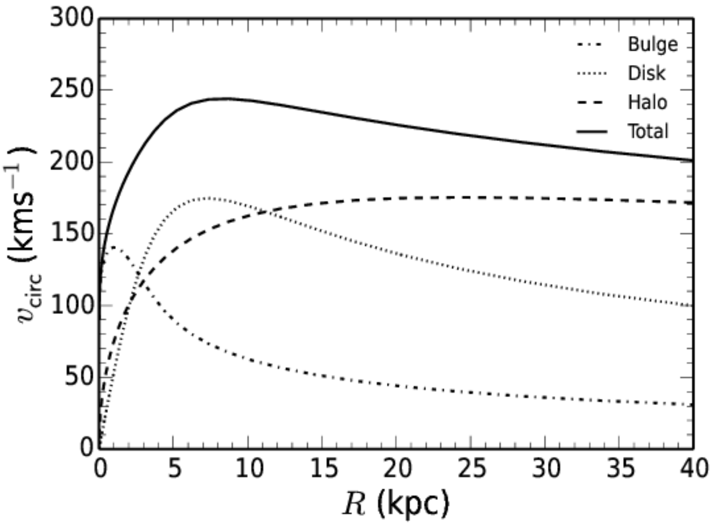

Figure 6: The distribution of velocities of stars as a function of the radius from the center of the galaxy. The contributions to the velocity from the various components of matter in the galaxy are shown [3].

came from the observation of galactic rotation curves, the velocities of stars as a function of the radius from the center of a galaxy. These can be directly predicted from the amount of matter contained within the sphere up to the radius of the star. An estimate of velocity based only on the luminous matter in the galaxies would predict a dependence that falls off with the radius, but the observed curves show a mostly constant distribution of velocities [3], as seen in Figure 6. The higher velocities than predicted by the luminous matter can be explained by a halo of dark matter that extends significantly outside the galactic disk.

This dark matter accounts for a majority of the matter in the universe, and is incompatible with the matter particles predicted by the SM. Many observations support its existence, but there have been no direct detections of a particle which could account for the large quantity of gravitationally interacting dark matter. The SM would have to require a significant extension to include the particles needed to explain dark matter and the processes needed to explain the observed matter-antimatter asymmetry.

3 SUPERSYMMETRY

The theory of SUSY presents an extension to the SM that solves a number of the outstanding issues. It is based an another proposed symmetry, one which introduces an equality between the fermionic particles and proposed bosonic partners and also between bosonic particles and their proposed fermionic partners. The symmetry is defined by extending spacetime into a superspace, which includes one dimension that describes a particle's spin: a transformation in this space moves a fermion with spin-1/2 to a boson with spin-0 or vice-versa. Requiring the SM to be symmetrical under these transformations requires the existence of a bosonic partner for every current matter fermion in the SM and a fermionic partner for every boson. The partners are called superparticles (sparticles), where quarks partner with squarks and leptons partner with sleptons, and each boson has a fermionic partner called a gaugino. The superpartners, in the original form of the theory, should be identical to the original particle in every way except for spin; that is they would have the same quantum charges and the same mass.

However, the simplest version of the theory, where the symmetry is unbroken, is incompatible with current observations of physics in a number of systems. The most striking example comes from the electron, as the superpartner of an electron would introduce a stable, negatively charged, and bosonic particle. Such a particle would drastically alter atomic properties by providing a way to create atoms without the valence structure of electrons that results from the Pauli exclusion principle for fermions. Various high energy physics measurements have also confirmed the spin of the W and Z bosons, for example, and a fermionic gaugino has never been produced at those masses. The solution to this incompatibility with observation is to conjecture that the symmetry exists but is spontaneously broken, where the masses of the supersymmetric particles are significantly larger than those of the current SM particles. Like the spontaneous symmetry breaking of the electroweak system, this symmetry breaking can be accomplished by introducing an additional Higgs mechanism.

3.1 STRUCTURE

There are a number of ways to model the particulars of SUSY, but many of the resulting phenomena are similar, and a discussion of an example is sufficient describe the structure and results of the theory. The MSSM is one example of a complete description that includes the necessary symmetry breaking to result in the different masses between particles and sparticles [4]. It is called minimal because it is designed to use the simplest possible extension to the SM that incorporates SUSY. However even a minimal version includes a remarkable number of free parameters, over 100, and the MSSM is often further constrained to include

Sector	Particles	Sparticles
Baryonic Matter	(u,d)	$(\tilde{u},\tilde{d})$
	(c,s)	$(\tilde{c},\tilde{s})$
	(t,b)	$(\tilde{t},\tilde{b})$
Leptonic Matter	(ν_e,e)	$(\tilde{\nu_e},\tilde{e})$
	(ν_μ,μ)	$(\nu_{\tilde{m}}u,\tilde{\mu})$
	(ν_τ,τ)	$(\tilde{\nu_\tau},\tilde{\tau})$
Higgs	(H_u^+,H_u^0)	$(\tilde{H}_u^+,\tilde{H}_u^0)$
	(H_d^0,H_d^-)	$(\tilde{H}_d^0,\tilde{H}_d^-)$
Strong	g	$\tilde{g}$
Electroweak	$(W^\pm,W^0)$	$(\tilde{W}^\pm,\tilde{W}^0)$
	B^0	$\tilde{B}^0$

Table 1: The particles in the SM and their corresponding superpartners in the MSSM.

fewer parameters in models such as the Phenomenological MSSM (pMSSM) and the Constrained MSSM (cMSSM) [5].

The theory includes a sparticle partner for every SM particle, which are listed in Table 1. To then provide the different masses for those sparticles, the MSSM introduces a second Higgs interaction. The resulting scalar field, along with the original Higgs field, generates five total particles, h^0, the original Higgs boson, A^0, H^0, and $H^\pm$, where the last two are electrically charged. These Higgs bosons can mix with the supersymmetric gauginos to form a series of mass eigenstates. These are usually referred to by the order of their masses, where the neutral gauginos (neutralinos) are labeled $\tilde{\chi}_1^0$, $\tilde{\chi}_2^0$, $\tilde{\chi}_3^0$, and $\tilde{\chi}_4^0$. The charged gauginos (charginos) are similarly labeled $\tilde{\chi}_1^\pm$ and $\tilde{\chi}_2^\pm$. Table 1, lists the gauginos which are direct partners of the original gauge bosons in the SM rather than these resulting mass eigenstates.

In addition to the new particle content, the MSSM introduces new interactions for the gauge bosons and gauginos. All interaction terms are added to the Lagrangian which describe the interaction of a gauge boson or gaugino with a particle or sparticle with the appropriate charge. Such terms include a few interactions which would violate the observed $B-L$ symmetry that prevents proton decay. Either the couplings on these terms must be extremely small to match the experimental limits on those decays, or an additional symmetry must be imposed to exclude the terms. The MSSM and several other SUSY models choose to introduce a new symmetry known as R-parity, where the conserved quantity, P_R is defined as

$$P_R = (-1)^{2s+3(B-L)}$$

with s as the spin of the particle. Sparticles are R-parity odd while SM particles are R-parity even. And by requiring that each term in the supersymmetric Lagrangian conserves R-parity, it is enforced that sparticles are produced in pairs.

The conservation of R-parity removes the $B - L$ violating terms from the Lagrangian. The remaining terms include all of the interactions of the SM where two of the particles are replaced with their SUSY partners, so that R-parity is conserved in the interactions. This also has an important significance in making the Lightest Supersymmetric Particle (LSP), the $\tilde{\chi}_1^0$, stable, as it cannot decay to only SM particles without violating the conservation of R-parity. The heavier sparticles then decay in chains, emitting an SM particle in each step, and leave behind the LSP at the end of the chain.

3.2 MOTIVATION

SUSY models, including the MSSM, ameliorate many of the issues in the SM discussed in Section 2.6. SUSY is particularly well motivated as a natural extension to the SM because the simple underlying assumption solves three major, seemingly unrelated concerns. And these benefits all require that at least some of the sparticles exist at the TeV scale, within the reach of modern collider experiments.

The first, a solution to the hierarchy problem, comes as a direct consequence of the introduction of massive superpartners for each SM particle. The contributions to the Higgs mass from the much higher energy Planck scale come from a series of loop diagrams in the SM, where each massive SM particle has a loop contribution. The introduction of superpartners generates a series of corresponding diagrams for correction to the Higgs mass, with opposite sign contributions because the superpartners have different spins. Those opposite sign contributions cancel the divergences from the original loop diagrams at high energies, leaving behind a correction to the Higgs mass that is at the same scale as the masses of the superpartners. If the superpartners exist at the TeV scale, then the Higgs mass of 125 GeV can be explained without significant fine-tuning, and the theory becomes natural.

SUSY also has the potential to precisely enable the unification of the coupling constants at high energy. Without supersymmetric contributions, the coupling constants come close to a single value near the Planck scale suggesting an underlying trend, as shown in Figure 5, but they do not exactly merge. With the addition of the MSSM, they can join almost exactly at a single point, enabling a unification into a single gauge theory at high energy, as shown in Figure 7. This precise unification, like the naturalness argument, also requires that the masses of the superpartners be near the TeV scale.

The presence of R-parity in a SUSY model also provides an explanation for dark matter. The LSP, as discussed in Section 3.1, is a massive, neutral, and stable particle as long as R-parity is conserved. In the early universe, when the energy density was extremely high, LSPs could be spontaneously produced just as often as other particles like photons, and would result in a thermal equilibrium. Then, as the universe cooled, the average energy would be too low to create additional LSPs, and they would be left behind and only interact with the remaining matter gravitationally, a process called freeze out. Since those particles are stable, they would remain indefinitely. With the existence of an LSP at around the TeV scale, this process can explain the observed amount of dark matter in the universe. A

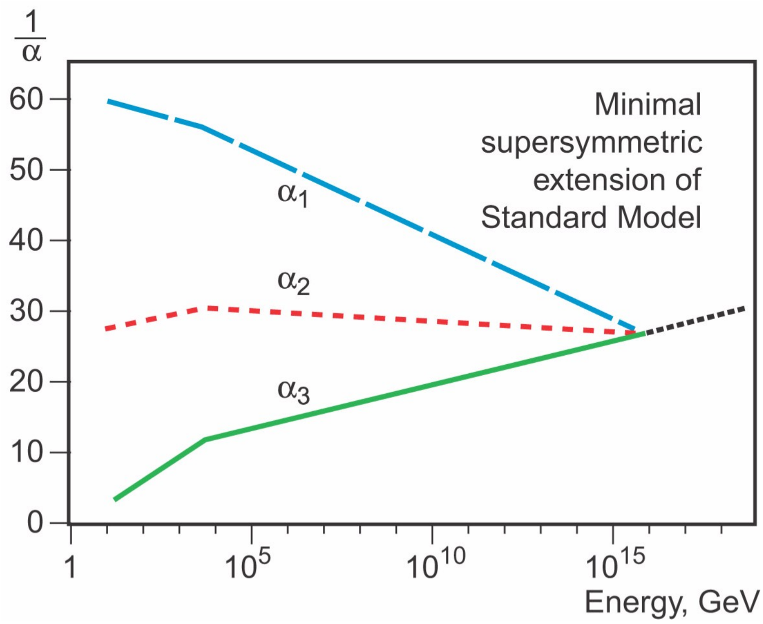

Figure 7: An approximation of the running of the coupling constants in the MSSM up to the Planck scale [2].

WIMP! (**WIMP!**), exactly what is proposed in the LSP, provides the correct interaction rate to predict the currently observed ratio of dark matter to baryonic matter.

Together, this variety of solutions to existing problems provides strong theoretical support for the existence of SUSY near the TeV scale. The LHC is the first collider experiment to be able to probe into TeV scale interactions, providing a new opportunity to search for this extension to the SM. A range of models have begun to be excluded with masses above 1 TeV [6], leading to a motivation to explore a wider variety of models with phenomena that may have been missed by the most direct search strategies.

3.3 SIMPLIFIED MODELS

The MSSM is just one example of a large suite of SUSY models with similar results. Each of those models can have hundreds of individual parameters that ultimately determine the masses and interactions of the supersymmetric particles. To avoid this complexity in making experimental measurements, the analyses of high energy collisions often rely on simplified models. These models focus on a single process predicted by a theory, and the observable parameters such as the mass of the particles and their lifetimes are controlled directly, rather than tuning the hundreds of underlying parameters. This allows straightforward simulation of a specific event topology with control over the parameters that most directly influence the experimental signatures.

Experimental analyses use these models to search for new physics and to set limits on the production rates for a given type of process with working points of a few observable parameters. As one example, a simplified model may specify

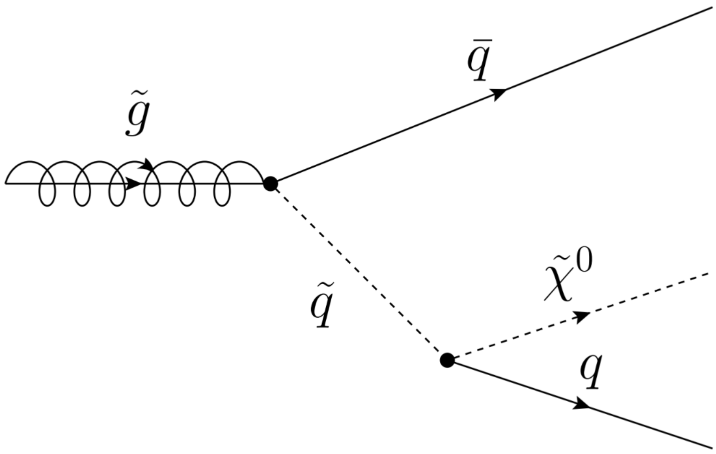

Figure 8: The decay of a gluino to quarks and an LSP, which precedes through a squark.

pair production of gluinos where the free parameters are the mass of the gluino and the types and masses of the particles it can decay into. The small number of parameters allows the phase space to be searched in a grid by simulating events with a few examples for the parameters and interpolating between them. The resulting analysis can set cross sectional limits as a function of the simplified parameters, and this allows for an easy interpretation of the result in a number of SUSY models.

3.4 LONG-LIVED PARTICLES

Some proposed SUSY models can produce LLPs other than just the LSP. The most direct search strategies for SUSY often assume that the various non-stable sparticles decay promptly, rather than propagating through some fraction of the detector. Although the processes involved are very similar, the long-lifetime of the produced particles can lead to very different experimental signatures, and often require separate dedicated searches. It is important to design and execute search strategies for LLPs in order to completely cover possible production of new physics.

There are a several ways to generate long lifetimes for the massive SUSY particles, depending on the specific model. In examples like Spread Supersymmetry [7] and Split Supersymmetry [8, 9], the introduction of a split between two mass scales suppresses the decay of gluinos. In these and similar models, the squarks are much heavier than the gluino, where the mass scale of the squarks is roughly 10^6 GeV while the mass scale of the gluinos is roughly 10^3 GeV. The gluino must decay through the production of a virtual squark, as shown in the diagram of Figure 8. The large mass of the squarks in the split models suppresses the decay rate, and can result in lifetimes of the order of 1 ns [7].

Nearly degenerate particles can also result in long lifetimes, again by suppressing decay rates. When a particle must decay to another particle with nearly the same mass, the phase space factor in the decay results in a low decay rate. For example, a neutron has a lifetime of roughly fifteen minutes because its mass is so close to the proton. Models which result in a nearly degenerate chargino and LSP provide a long-lived chargino as well.

Again, because of the wide variety of models which can produce LLPs and the large number of parameters which determine their masses and lifetimes, the analysis presented here focuses on simplified models rather than assuming any particular underlying theory. The models directly specify the decay mode of the LLPs as well as their masses and lifetimes, using a grid of values. The results of searches using these simplified models can be interpreted over a very wide range of models that predict LLPs, even including non-supersymmetric extensions to the SM.

PART II

EXPERIMENTAL STRUCTURE AND RECONSTRUCTION

You can put some informational part preamble text here.

4 THE LARGE HADRON COLLIDER

The LHC, a two-ring superconducting hadron accelerator, provides high energy proton-proton collisions for several large experiments at European Organization for Nuclear Research (CERN) in Geneva, Switzerland [10, 11]. It is the largest, highest-luminosity, and highest-energy proton collider ever built, and was constructed by a collaboration of more than 10,000 scientists from the more than 100 countries that contribute to CERN. The original design of the LHC focused on providing collision energies of up to 14 TeV and generating enough collisions to reveal physics beyond the SM which is predicted to exist at higher energy scales.

The LHC was installed in an existing 27 km tunnel at CERN which was originally designed to house the Large Electron Positron collider (LEP) [12]. This allows the collider to use existing accelerators at the same complex to provide the initial acceleration of protons up to 450 GeV before injecting into LHC. The injected hadrons are accelerated up to as much as 14 TeV while being focused into two beams traveling in opposite directions. During this process the protons circulate around the tunnel millions of times, while the beams are intermittently crossed at the four locations of the experiments to provide collisions. These collision points correspond to the four major LHC experiments: ATLAS, Compact Muon Solenoid (CMS), Large Hadron Collider beauty experiment (LHCb), and A Large Ion Collider Experiment (ALICE), and Figure 9 shows the layout of the experiments both on the surface and below. ATLAS and CMS are both general purpose, high-luminosity detectors which search for a wide range of new types of physics [13, 14]. LHCb studies the interactions of b-hadrons to explore the asymmetry between matter and antimatter [15]. ALICE focuses on the collisions of lead ions, which the LHC also provides, in order to study the properties of quark-gluon plasma [16].

During the first five years of continued operation, after the LHC turned on in 2010, the LHC has provided four major data collecting periods. In 2010 the LHC generated collisions at several energies, starting at 900 GeV. It increased the energy from 900 GeV to 2.76 TeV and then subsequently to 7 TeV, with a peak luminosity of 2×10^{32} cm$^{-2}s^{-1}$, and a total delivered luminosity of 50 pb^{-1}. The next run, during 2011, continued the operation at 7 TeV and provided an additional 5 fb^{-1}with a peak luminosity of 4×10^{33} cm$^{-2}s^{-1}$. The energy was then increased to 8 TeV for the data collection during 2012, which provided 23 fb^{-1}with a peak luminosity of 7.7×10^{33} cm$^{-2}s^{-1}$. After the first long shutdown for 2013 and 2014, the LHC resumed operation and increased the energy to 13 TeV in 2015, where it delivered 4.2 fb^{-1}with a peak luminosity of 5.5×10^{33} cm$^{-2}s^{-1}$. The LHC is currently providing additional 13 TeV collisions in 2016 with higher luminosities than during any previous data collection periods. These running periods are summarized in Figure 10, which shows the total delivered

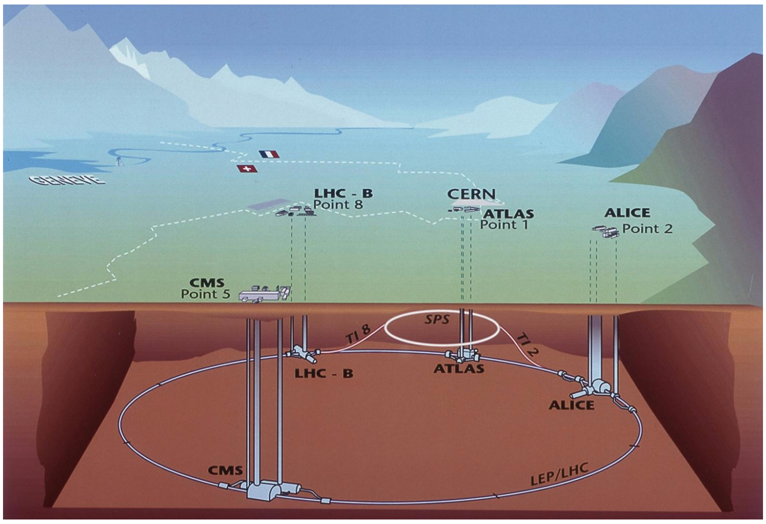

Figure 9: The four collision points and corresponding experiments of the LHC. The image includes the location of the nearby city of Geneva as well as the border of France and Switzerland.

luminosity over time for the ATLAS experiment during each of the four years of data collection since 2011.

4.1 INJECTION CHAIN

The LHC takes advantage of the presence of previously built accelerators at CERN to work up to the target energy in consecutive stages. The series of accelerators that feed into the LHC are known collectively as the injection chain, and together with the LHC form the accelerator complex. The full complex is illustrated in Figure 11, which details the complex series required to reach collisions of 13 or 14 TeV.

Protons at the LHC begin as hydrogen atoms in the Linac 2, a linear accelerator which replaced Linac 1 as the primary proton accelerator at CERN in 1978. In Linac 2, the hydrogen atoms are stripped of their electrons by a strong magnetic field, and the resulting protons are accelerated up to 50 MeV by cylindrical conductors charged by radio frequency cavities. The protons are then transferred to the Proton Synchrotron Booster (PSB), which uses a stack of four synchrotron rings to accelerate the protons up to 1.4 GeV. Then the protons are injected into the Proton Synchrotron (PS) which again uses synchrotron rings to bring the energy up to 25 GeV. The intermediate step between Linac 2 and the PS is not directly necessary, as the PS can accelerate protons starting from as low as 50 MeV. The inclusion of the PSB allows the PS to accept a higher intensity of injection and so increases the deliverable luminosity in the LHC. The penultimate stage of acceleration is provided by the Super Proton Synchrotron (SPS), a large synchrotron with a 7 km circumference that was commissioned at CERN in 1976. During this step the protons increase in energy to 450 GeV, after which they can be directly injected into the LHC.

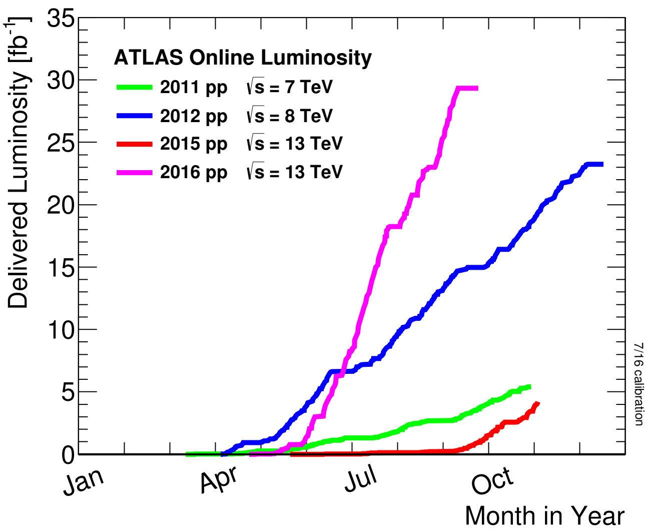

Figure 10: The cumulative luminosity over time delivered to the ATLAS experiment from high energy proton-proton collisions since 2011. The energies of the collisions are listed for each of the data-taking periods.

The final step is the LHC itself, which receives protons from the SPS into two separate beam pipes which circulate in opposite directions. The filling process at this steps takes approximately 4 minutes, and the subsequent acceleration to the final energy (6.5 TeV during 2015 and up to 7 TeV by design) takes approximately half an hour. At this point the protons circulate around the circumference tens of thousands of times a second and continue for up to two hours.

4.2 DESIGN

4.2.1 LAYOUT

Many of the aspects of the LHC design are driven by the use of the existing LEP tunnel. This tunnel slopes gradually, with a 1.4% decline, with 90% of its length built into molasse rock which is particularly well suited to the application. The circumference is composed of eight 2987 meter arcs and eight 528 meter straight sections which connect them; this configuration is illustrated in Figure 12. The tunnel diameter is 3.7 m throughout its length.

The design energy is directly limited by the size of this tunnel, with its radius of curvature of 2804 m. A significant magnetic field is required to curve the protons around that radius of curvature; the relationship is given by

$$p \simeq 0.3BR \tag{13}$$

where p is the momentum of the particle in GeV, B is the magnetic field in Tesla, and R is the radius of curvature in meters. From the target design energy of 14 TeV, or 7 TeV of momentum for protons in each beam, the required magnetic field is 8.33 Tesla. This is too large a field strength to be practical with iron electromagnets, because of the enormous power required and the resulting

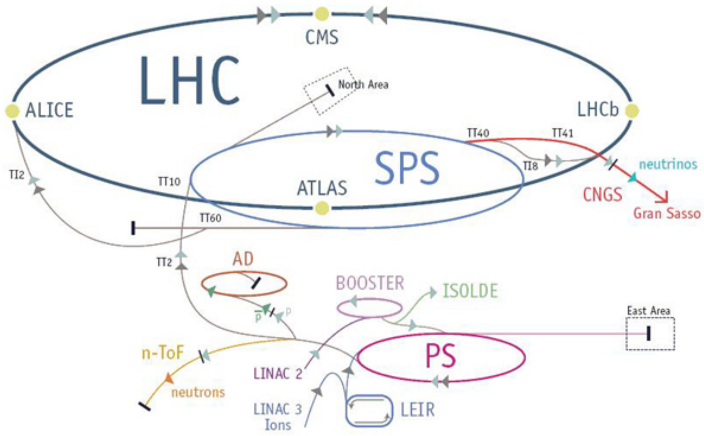

Figure 11: The accelerator complex that builds up to the full design energies at the LHC. The protons are passed in order to Linac 2, the PSB, the PS, the SPS and then the LHC.

requirements for cooling. Because of these constraints, the LHC uses superconducting magnets which can maintain that field strength with significantly less power consumption.

4.2.2 MAGNETS

The magnets chosen were Niobium and Titanium (NbTi) which allow for field strengths as high as 10 Tesla when cooled down to 1.9 K. Reaching the target temperature of 1.9 K for all of the magnets requires superfluid helium and a large cryogenic system along the entire length of the tunnel. During normal operation, the LHC uses 120 tonnes of helium within the magnets, and the entire system is cooled by eight cryogenic helium refrigerators. The temperature increase that occurs during transit from the refrigerator along the beam necessitates that the refrigerators cool the helium down to 1.8 K. Any significant increase above this temperature range can remove the superconductive properties of the magnets, which in turn generates drastically larger heat losses from the current within the magnets and causes a rapid rise in temperature called a quench.

There are approximately 8000 superconducting magnets distributed around the LHC. The 1232 bending magnets, which keep the protons curving along the length of the beam, are twin bore cryodipoles, which allow both proton beams to be accommodated by one magnet and all of the associated cooling structure. Figure 13 shows the cross section of the design for these dipoles. The magnets are very large, 16.5 m long with a diameter of 0.57 meters and a total weight of 28 tonnes. They are slightly curved, with an angle of 5.1 mrad, in order to carefully match the beam path. The twin bore accommodates both magnets inside the two 5 cm diameter holes which are surrounded by the superconducting coils. The coils require 12 kA of current in order to produce the required magnetic field. These coils are comprised of NbTi cable wound in two layers; the wire in

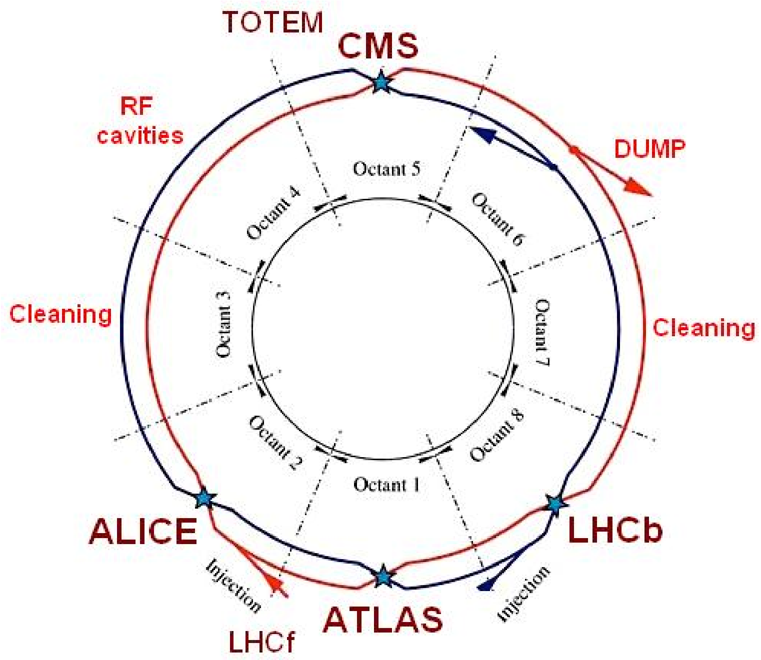

Figure 12: A schematic of the layout of the LHC, not to scale. The arched and straight sections are illustrated at the bottom of the schematic, and all four crossing sites are indicated with their respective experiments.

the inner layer has a diameter of 1.065 mm while the wire in the outer layer has a diameter of 0.825 mm.

The large currents in the wires, along with the magnetic field produced, result in forces on the magnets which would tend to push them apart with over 10,000 Newtons per meter. Constraining the magnets requires a significant amount of structure including non-magnetic stainless steel collars. Both the presence of these electromagnetic forces and the varying thermal contraction coefficient of the pieces of the magnet produce significant forces on the cold mass structure. The cold mass is carefully engineered to so that these stresses do not significantly alter the magnetic field shape, which must be maintained between magnets to a precision of approximately 10^{-4} for successful operation.

The remaining 6800 magnets are a variety of quadrupole, sextapole, octopole, and single bore dipole magnets. These are used to damp oscillations, correct beam trajectories, focus the beams during circulation, and to squeeze the beams before collisions.

4.2.3 RF CAVITIES

Sixteen RF cavities produce the actual acceleration of the proton beam up to the design energy. These RF cavities are tuned to operate at 400 MHz, and are powered by high-powered electron beams modulated at the same frequency, called klystrons. The resonance within the cavity with the oscillating electric field establishes a voltage differential of 2 MV per cavity. The sixteen cavities are split between the two beams, so combined the cavities provide 16 MV per beam,

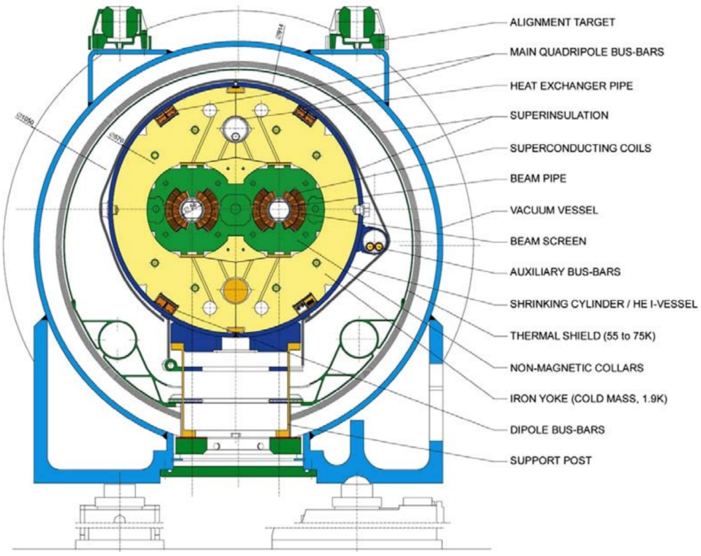

Figure 13: A cross section of the the cryodipole magnets which bend the flight path of protons around the circumference of the LHC. The diagram includes both the superconducting coils which produce the magnetic field and the structural elements which keep the magnets precisely aligned.

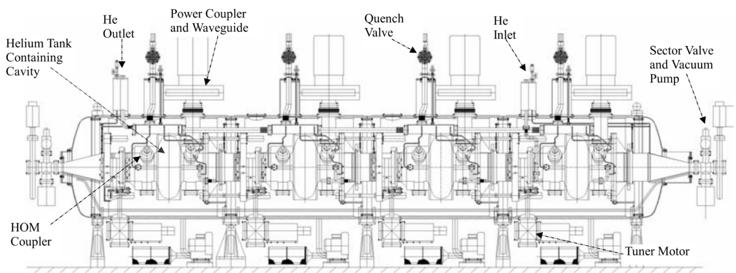

Figure 14: The arrangement of four RF cavities within a cryomodule.

which accelerate the protons on each consecutive pass through the cavity. This acceleration is also necessary during circulation even after the target energy has been reach in order to compensate for losses from synchrotron radiation.

The cavities are arranged in cryomodules which contain four cavities, with two cryomodules per beam; this arrangement is illustrated in Figure 14. These cryomodules are necessary to maintain the superconducting state of the cavities, which are also constructed from niobium. The RF cavities use niobium along with copper to allow for low power losses in the superconductors. The copper provides a reduced susceptibility to quenching, as it rapidly conducts away heat generated by imperfections in the niobium, as well as natural shielding from the earth's magnetic field which can interfere with the RF system.

The nature of the radio frequency oscillations tends to group protons together into buckets. A proton traveling exactly in phase with the RF oscillations will not be displaced at all during a single circulation, and those slightly ahead or behind of that phase will slightly decelerate or accelerate, respectively. This produces separate clusters of protons which arrive in phase to the cavities every 2.5 ns, corresponding to the 400 MHz frequency.

4.2.4 BEAM

The beams of protons circulate within 54 km of 5 cm diameter beam pipe. This entire structure is kept under vacuum at 1.9 K to prevent interactions between the beam pipe and the magnets as well as to prevent any interactions between the circulating protons and gas in the pipe. The vacuum within the pipe establishes a pressure as low as 10^{-9} mbar before the protons are introduced.

Because of the very high energies of the circulating protons, synchrotron radiation is not negligible in the bending regions. The protons are expected to radiate 3.9 kW per beam at 14 TeV, with 0.22 W/m, which is enough power to heat the liquid helium and cause a quench were it absorbed by the magnets. To prevent this, a copper screen is placed within the vacuum tube that absorb the emitted photons. This screen is kept between 5 and 20 K by the liquid helium cooling system.

4.3 LUMINOSITY PARAMETERS

In addition to the high energy of the collisions, the rate of collisions is extremely important to enabling the discovery of new physics. Many measurements and searches require a large number of events in order to be able to make statistically significant conclusions. The rate of collisions is measured using luminosity, the number of collisions per unit time and unit cross section for the proton-proton collisions. From the beam parameters, luminosity is given by

$$\mathcal{L} = \frac{N_b^2 n_b f_{rev} \gamma}{4\pi\epsilon_n\beta^*}F \tag{14}$$

where N_b is the number of protons per bunch, n_b is the number of bunches per beam, f_{rev} is the frequency of revolution, γ is the Lorentz factor for the protons at the circulating energy, ϵ_n is the emittance, β^* is the amplitude function at the collision point, and F is a geometric factor that accounts for the crossing angle of the beams at the collision point. The emittance measures the average spread of particles in both position and momentum space, while the amplitude function is a beam parameter which measures how much the beam has been squeezed. Together ϵ_n and β^* give the size of the beam in the transverse direction, $\sigma = \sqrt{\epsilon\beta^*}$. β changes over the length of the beam as the accessory magnets shape the distribution of protons, but only the value at the point of collisions, β^*, affects the luminosity.

The luminosity is maximized to the extent possible by tuning the parameters in Equation 14. A number of these are constrained by the design decisions. The revolution frequency is determined entirely by the length of the tunnel, as the protons travel at very close to the speed of light. The geometric factor F is determined by the crossing angle of the beams at the collision points, again a com-

Parameter	Unit	Injection	Nominal
Beam Energy	TeV	0.450	7
Peak Instantaneous Luminosity	$cm^{-2}s^{-1}$	-	10^{34}
Bunch Spacing	ns	25	25
Number of Filled Bunches	-	2808	2808
Normalized Transverse Emittance	μm	3.75	3.75
Frequency	MHz	400.789	400.790
RF Voltage/Beam	MV	8	16
Stored Energy	MJ	-	362
Magnetic Field	T	0.54	8.33
Operating Temperature	K	1.9	1.9

Table 2: The design parameters of the LHC beam that determines the energy of collisions and the luminosity, for both the injection of protons and at the nominal circulation.

ponent of the tunnel design; this angle is already very small at 285 μrad, which helps to maximize the geometric factor.

The major pieces that can be adjusted are the number of protons per bunch, N_b, the number of bunches in the beam, n_b, and the amplitude function β. Increasing either N_b or n_b increases the amount of energy stored in the beam, which presents a danger if control of the beam is lost. At design specifications, the beam stores 362 MJ, which is enough energy to damage the detectors or accelerator if the beam were to wander out of the beam pipe. So, the luminosity is primarily controlled at the LHC by adjusting β^*, where lowering β^* increases the luminosity. β^* is tuned to provide the various values of luminosity used at the LHC which can be raised to as much as 10^{34}.

The nominal bunch structure consists of 3654 bunches, each holding 10^{11} protons, which cross a collision point in 25 ns. These are further subdivided into the buckets mentioned in Section 4.2.3 by the clustering properties of the RF cavities. The bunches are further grouped into trains of 72 bunches which are separated by a gap which would otherwise hold 12 bunches. At nominal operation 2808 of the bunches will actually be filled with protons, while the remainder are left empty to form an abort gap that can be used in case the beam needs to be dumped.

The various beam parameters are summarized in Table 2 for the designed operation. In practice, the beam has operated at lower energies and lower luminosities than the design values for the majority of its lifetime, but the LHC has begun to operate at full design values during Run 2.

4.4 DELIVERED LUMINOSITY

During the data collection of 2015, the LHC operated at luminosities as larges as 5×10^{33} $cm^{-2}s^{-1}$. It is convenient to refer to the integrated luminosity, the inte-

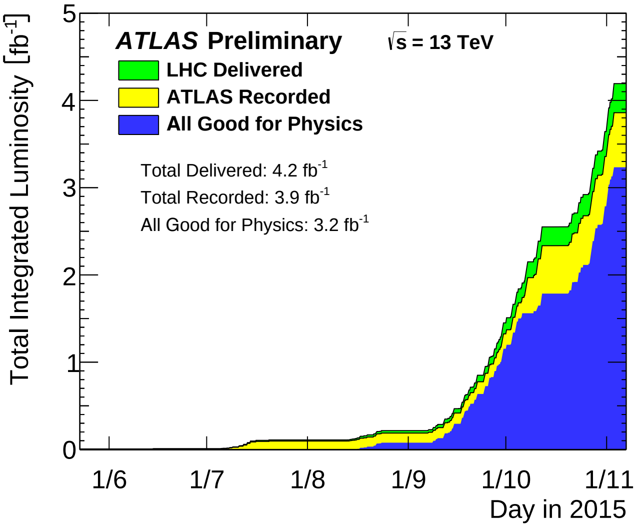

Figure 15: The cumulative luminosity versus time delivered to ATLAS (green), recorded by ATLAS (yellow), and certified to be good quality data (blue) during stable beams for pp collisions at 13 TeV in 2015.

gral of the instantaneous luminosity, which corresponds directly to the number of delivered events for a given process.

$$N = \sigma \times \int \mathcal{L}(t)dt$$

where σ is the cross section for the process of interest. The integrated luminosity over time is shown in Figure 15. This includes the luminosity delivered by the LHC as well as the luminosity that was recorded by ATLAS. ATLAS only records collisions when the LHC reports that the beam conditions are stable, so some of the delivered luminosity is not recorded. The figure also includes the amount of luminosity marked as good for physics, which includes additional requirements on the operation of the detector during data collection that are necessary for precise measurements.

Because the beam circulates and collides bunches of protons, it is possible for a single crossing to produce multiple proton-proton collisions. As the instantaneous luminosity is increased, the average number of collisions generated per bunch crossing increases. An event refers to the entire collection of interactions during a single bunch crossing, while interactions refer to the individual proton-proton collisions. The additional interactions produced during each bunch crossing are referred to as pileup, which can be more precisely defined quantified using the average number of additional proton-proton interactions per crossing, often denoted μ. Figure 16 shows the luminosity-weighted distribution of the mean number of interactions for events collected in 2015. The presence of as many as twenty interactions in a single collision provides a significant challenge in reconstructing events and isolating the targeted physical processes.

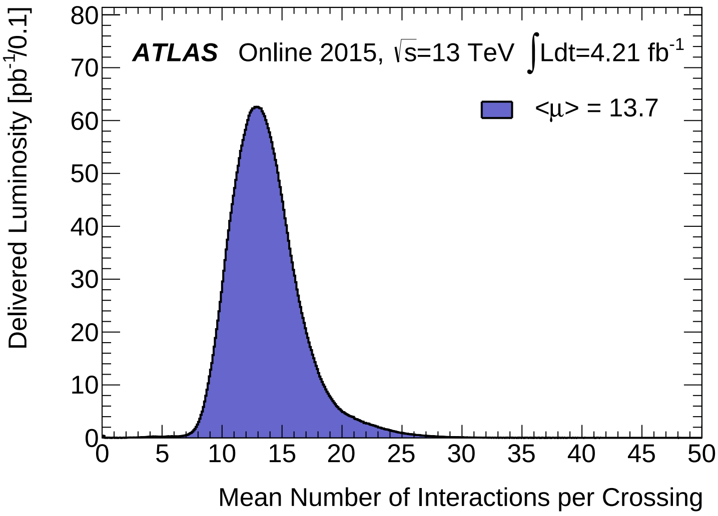

Figure 16: The luminosity-weighted distribution of the mean number of interactions per crossing for the 2015 pp collision data at 13 TeV.

5

THE ATLAS DETECTOR

The four major LHC experiments at CERN seek to use the never before matched energies and luminosities of the new collider to explore the boundaries of particle physics and to gain insight into the fundamental forces of nature. Two of these experiments, ATLAS and CMS, are general purpose detectors that seek to measure a variety of processes in the up to 13 TeV proton-proton collisions that occur as much as 800 million times per second at the LHC at the design luminosity of 10^{34} cm$^{-2}s^{-1}$. ATLAS employs a hermetic detector design, one which encloses the particle collisions as completely as possible with detecting elements, that allows it to study a wide range of physics from SM and Higgs measurements to searches for new physics in models like SUSY [13].

Accommodating this wide variety of goals is a challenge for the design of the detector. The wide range of energies involved requires high measurement precision over several orders of magnitude, and the numerous physics processes require an ability to measure a variety of particle types. At the time of the construction of ATLAS, the Higgs boson had yet to be discovered, but the diphoton decay mode was (correctly) expected to be important and necessitated a high resolution photon measurement. The potential for decays of new heavy gauge bosons, W' and Z', required a similarly high momentum resolution for leptons with momentum up to several TeV. Hadronic decay modes of several possible new high energy particles could result in very energetic jets, again up to several TeV, and reconstructing the decay resonances would again require good energy resolution. Several models, such as SUSY or Extra Dimensions, predict the existence of particles which would not interact with traditional detecting elements. However these particles can still be observed in a hermetic detector by accurately measuring the remaining event constituents to observe an imbalance in energy called missing energy or E_T^{miss}. Measuring E_T^{miss} implicitly requires a good resolution on all SM particles that can be produced. And at the lower end of the energy spectrum, precision SM measurements would require good resolution of a variety of particle types at energies as low as a few GeV, so the design needs to accommodate roughly three orders of magnitude.

This broad spectrum of measurements requires a variety of detector systems working together to form a cohesive picture of each collision. Two large magnet systems produce magnetic fields that provide a curvature to the propagation of charged particles and allows for precision momentum measurements by other systems. The inner detector uses a combination of tracking technologies to reconstruct particle trajectories and vertices for charged particles. A variety of calorimeters measure the energies of hadrons, electrons, and photons over a large solid angle. A large muon spectrometer identifies muons and uses the second magnet system to provide an independent measurement of their momentum from the inner detector and improve the resolution. The layout of all of these systems is shown in Figure 17.

The performance goals needed to achieve the various targeted measurements and searches discussed above can be summarized as resolution and coverage requirements on each of these systems. Those requirements are listed in Table 3.

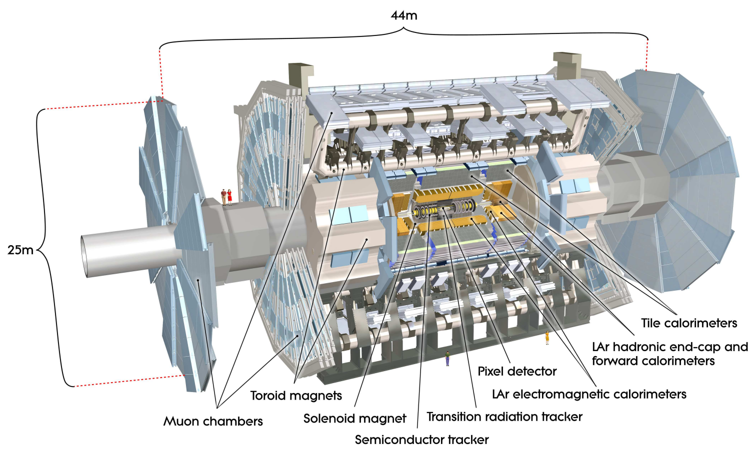

Figure 17: A cut-away schematic of the layout of the ATLAS detector. Each of the major subsystems is indicated.

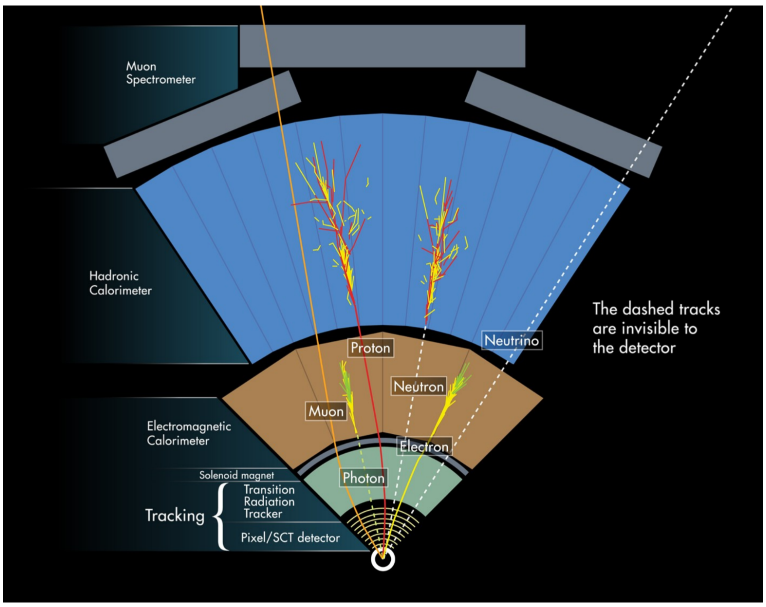

Figure 18: A cross-sectional slice of the ATLAS experiment which illustrates how the various SM particles interact with the detector systems.

Incorporating these various pieces into a single detector is a significant technical challenge. The resulting detector has a diameter of 22 m, is 46 m long, and weighs 7,000 tons; it is the largest volume particle detector ever constructed. The various detector elements need to be constructed and assembled with precision as low as micrometers. These systems all need to function well even after exposure to the significant radiation dose from the collisions. Designing, con-

Detector Component	Required Resolution	$\|\eta\|$ Coverage	
		Measurement	Trigger
Tracking	$\sigma_{p_T}/p_T = 0.05\% p_T + 1\%$	2.5	-
EM Calorimetry	$\sigma_E/E = 10\%/\sqrt{E} + 0.7\%$	3.2	2.5
Hadronic Calorimetry			
Barrel and Endcap	$\sigma_E/E = 50\%/\sqrt{E} + 3\%$	3.2	3.2
Forward	$\sigma_E/E = 100\%/\sqrt{E} + 10\%$	3.1 – 4.9	3.1 – 4.9
Muon Spectrometer	$\sigma_{p_T}/p_T = 10\%$ at $p_T = 1$ TeV	2.7	2.4

Table 3: The performance goals for each of the subsystems of the ATLAS detector. The $|\eta|$ coverage specifies the range where the subsystem needs to be able to provide measurements with the specified resolution. The resolutions include a p_T or E dependence that is added in quadrature with a p_T/E independent piece.

structing, and installing the detector took the combined effort of more than 3000 scientists from 38 countries over almost two decades.

5.1 COORDINATE SYSTEM

The coordinate system defined for the ATLAS detector is used throughout all of the sections of this thesis. The system begins with the choice of a z axis along the the beamline. The positive z side of the detector is commonly referred to as the A-side, and the negative z side is referred to as the C-side. The $x - y$ plane is then the plane transverse to the beam direction, with the x direction defined as pointing from the interaction point to the center of the LHC ring and the y direction defined as pointing upwards. The nominal interaction point is the origin of this system.

It is more convenient in practice to use a cylindrical coordinate system; this choice of coordinate system reflects the cylindrical symmetry of the ATLAS detector. The distance from the beamline is the radius, r', and the angle from the z-axis is θ. The azimuthal angle uses the usual definition, with ϕ running around the z-axis and $\phi = 0$ corresponding to the x-axis. Many aspects of the detector are independent of the this coordinate to first order. The θ direction is typically specified using rapidity or pseudorapidity, where rapidity is defined as

$$y = \frac{1}{2} \ln \frac{E + p_z}{E - p_z} \tag{15}$$

Rapidity is particularly useful to indicate the component along the z direction because differences in rapidity are invariant to boosts along the z-direction. A similar quantity which depends only the θ is pseudorapidity,

$$\eta = -\ln \tan \frac{\theta}{2} \tag{16}$$

which is the same as rapidity when the particle is massless and in the limit where the energy is much larger than the particle's mass. It is often useful to refer to differences in solid angle using the pseudorapidity and the azimuthal angle:

$$\Delta R = \sqrt{\Delta\phi^2 + \Delta\eta^2} \tag{17}$$

The pseudorapidity is also invariant to boosts along the z-axis for high momentum particles, and is preferable to rapidity because it does not depend on the specific choice of particle. Pseudorapidity is also preferable to θ because particle production is roughly uniform in equal-width intervals of η up to about $\eta = 5.0$. A particle traveling along the beampipe has $\eta = \inf$ and a particle traveling perpendicular to the beampipe has $\eta = 0$. The extent of the tracker, $|\eta| < 2.5$, corresponds to approximately $0.05\pi < \theta[\text{rad}] < 0.95\pi$ and the extent of the calorimeters, $|\eta| < 4.9$ corresponds to approximately $0.005\pi < \theta[\text{rad}] < 0.995\pi$. Many detector components are broken into multiple subsystems to provide coverage at greater $|\eta|$. The lower $|\eta|$ region is referred to as the barrel, typically with $|\eta| \lesssim 2$, and the greater $|\eta|$ region is often referred to as the endcap.

The initial energy and momentum of a proton-proton collision along the z direction is unknown in hadron colliders because different energies and momenta can be carried by the partons. Along the transverse plane, however, the vector sum of momentum will be zero. For this reason, many physical quantities are quantified in terms of their projection onto the transverse plan, such as p_{T} or E_T. In addition, p_{T} alone determines the amount of curvature in the magnetic field, and can be measured independently by measuring the curvature of a particle's propagation.

5.2 MAGNETIC FIELD

The magnet system used in ATLAS is designed to provide a substantial magnetic field in the two regions where the trajectory of particles is measured, the inner detector and the muon spectrometer. The magnetic field provides a curvature to the trajectory of charged particles and allows the precision tracking elements to make high resolutions measurements of p_{T}. To provide a magnetic field in these regions, ATLAS uses a hybrid system with four separate, superconducting magnets. A single solenoid provides a 2 T axial, uniform magnetic field for the inner detector, while a barrel toroid and two endcap toroids produce a non-uniform magnetic field of 0.5 and 1 T, respectively, for the muon detectors. This geometry is illustrated in Figure 19, and the parameters of the three magnet systems are summarized in Table 4.

The central solenoid uses a single-layer coil with a current of 7.730 kA to generate the 2 T axial field at the center of the magnet. The single-layer coil design enables a minimal amount of material to be used in the solenoid's construction, which is important because the solenoid is placed between the inner detector and the calorimeters. At normal incidence the magnet has only 0.66 radiation lengths worth of material, where one radiation length is the mean distance over

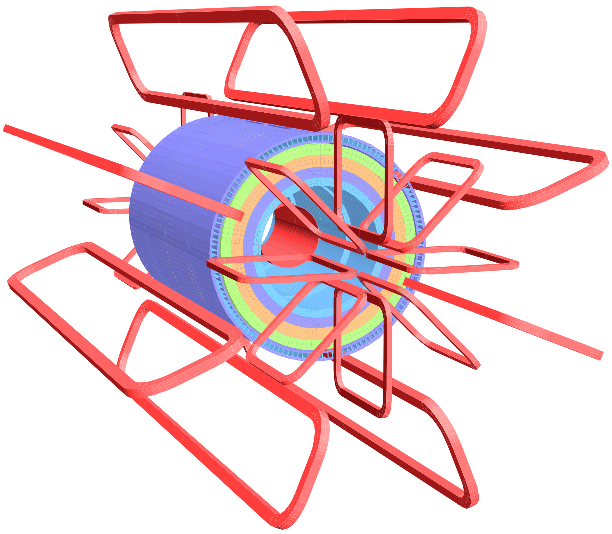

Figure 19: The layout of the four superconducting magnets in the ATLAS detector.

Parameter	Unit	Solenoid	Barrel Toroid	Endcap Toroids
Inner Diameter	m	2.4	9.4	1.7
Outer Diameter	m	2.6	20.1	10.7
Axial Length	m	5.3	25.3	5.0
Weight	tons	5.7	830	239
Conductor Size	mm^2	30×4.25	57×12	41×4.25
Peak Field	T	2.6	3.9	4.1
Heat Load	W	130	990	330
Current	kA	7.7	20.5	20.0
Stored Energy	MJ	38	1080	206

Table 4: A summary of the parameters of each of the three magnet systems on ATLAS.

which a high-energy electron loses all but $1/e$ of its energy through material interactions [6]. The coil is made of a high-strength aluminum stabilized NbTi superconductor which was optimized to achieve a high field with minimal thickness. The axial magnetic field produced by the solenoid bends charged particles in the ϕ direction, following a circular path with a radius specified by Maxwell's equations (see Equation 13).

The barrel toroid consists of eight coils which generate a 0.5 T magnetic field, on average, in the cylindrical region around the calorimeters with an approximately 20 kA current. The coils are separated only by air to reduce the scattering of muons as they propagate through the region. The coils are made of an aluminum stabilized NbTiCu superconductor and each is separately housed in a vacuum and cold chamber. This magnetic configuration produces a field in the ϕ and so curves muons traversing the volume primarily in the η direction.

The endcap toroids follow a similar design to the barrel toroid and produce a 1.0 T magnetic field, on average. Each has eight separate NbTiCu coils, and in this case all eight are housed within a single cold mass. This extra structure is necessary to withstand the Lorentz forces exerted by the magnets. These magnets are rotated 22.5% relative to the barrel toroid to provide a uniform field in the transition between the two systems. The endcap toroids also produce a field in the ϕ direction and curve muons primarily in the η direction.

5.3 INNER DETECTOR

The ATLAS inner detector provides excellent momentum resolution as well as accurate primary and secondary vertex measurements through robust pattern recognition that identifies tracks left by charged particles. These tracks fulfill a number of important roles in the ATLAS measurement system: they measure the momentum of charged particles including electrons and muons, they can identify electrons or photon conversions, they assign various particles and jets to different vertices, and they provide a correction to E_T^{miss} measurements from low energy particles. The system has to be accurate enough to separate tracks from dozens of vertices, to resolve each vertex individually, and to measure the p_{T} of very high momentum tracks which curve very little even in the large magnetic field. This is accomplished by several independent layers of tracking systems. Closest to the interaction point is the very high granularity Pixel detector, including the newly added Insertible B-Layer, which is followed by the SCT layers. These silicon subdetectors both use discrete space-points to reconstruct track patterns. The final layer, the Transition Radiation Tracker (TRT), uses many layers of straw tube elements interleaved with transition radiation material to provide continuous tracking. The arrangement of these subdetectors is shown in Figure 20. To provide the desired hermetic coverage, the subdetectors are divided into barrel and endcap geometries. Figure 21 shows the layout of the subdetectors in more detail, and illustrates how tracks at various pseudorapidities can traverse the subdetectors; tracks with $\eta > 1.1$ begin to traverse the endcap subdetectors rather than those in the barrel, and tracks with $\eta > 1.7$ use primarily endcap elements. The IBL was not present during the original commissioning of the inner detector and is not shown in this figure.

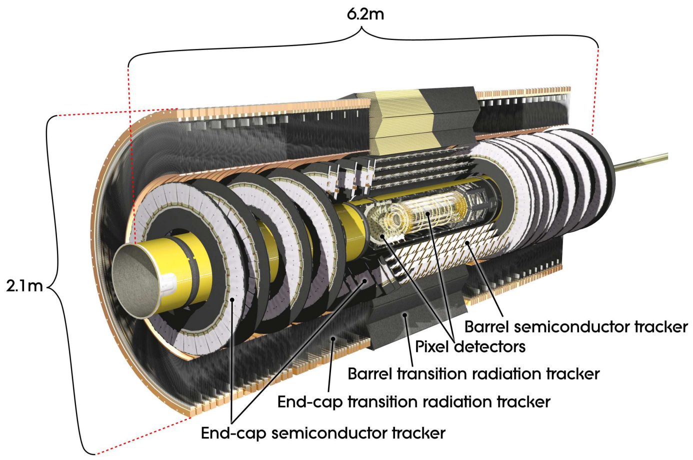

Figure 20: The arrangement of the subdetectors of the ATLAS inner detector. Each of the subdetectors is labeled in the cut-away view of the system.

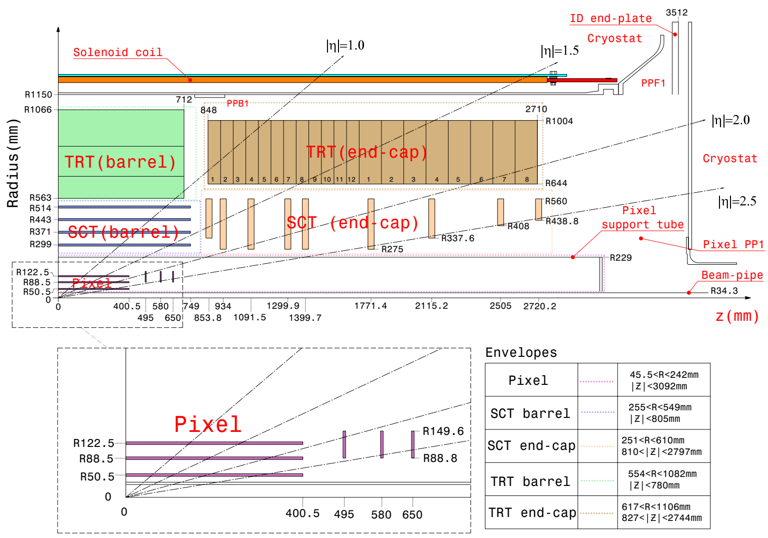

Figure 21: A quarter section of the ATLAS inner detector which shows the layout of each of the subdetectors in detail. The lower panel shows an enlarged view of the pixel detector. Example trajectories for a particle with $\eta = 1.0, 1.5, 2.0, 2.5$ are shown. The IBL, which was added after the original detector commissioning, is not shown.

Figure 22 shows a computer generated three-dimensional view of the inner detector along the beam axis, which emphasizes the straw tube structure of the TRT as well as the overlapping geometry of the SCT. This figure also includes the IBL, which was added during the long shutdown and provides an additional measurement layer in the Pixel detector as of the beginning of Run 2. Figure 23 shows an alternative computer generated three-dimensional view transverse to the beam axis which emphasizes the endcap structures of the SCT and TRT.

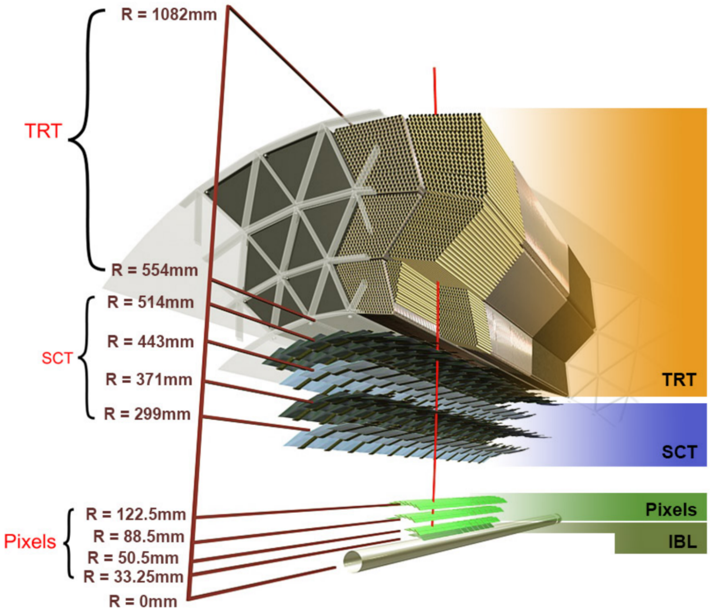

Figure 22: A computer generated three-dimensional view of the inner detector along the line of the beam axis. The subdetectors and their positions are labeled.

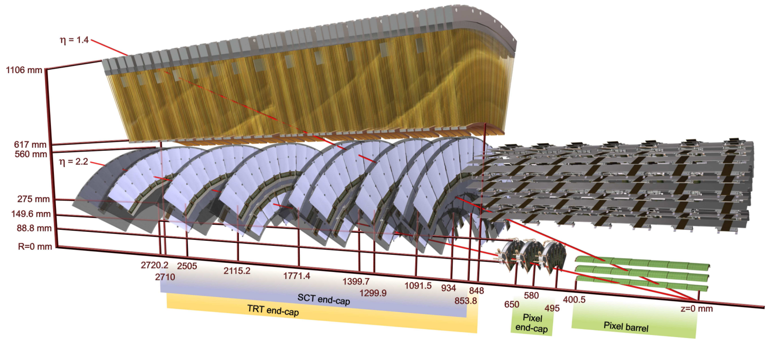

Figure 23: An alternative computer generated three-dimensional view of the inner detector transverse to the beam axis. The subdetectors and their positions are labeled.

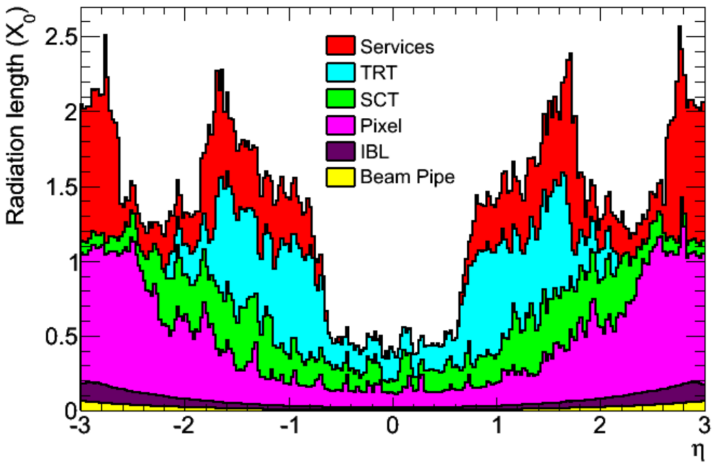

Figure 24: The integrated radiation lengths traversed by a straight track at the exit of the ID envelope, including the services and thermal enclosures. The distribution is shown as a function of $|\eta|$ and averaged over ϕ. The breakdown indicates the contributions of individual sub-detectors, including services in their active volume.

As the closest system to the interaction point, it is crucial for the inner detector to use as little material as possible to avoid scattering of charged particles or photon conversions before they reach the remaining subdetectors. The various components, including the readout electronics, cooling infrastructure, gas volumes, and support structures, were designed to accommodate this need for minimal components. Even with these optimizations, the combination of stringent performance requirements and the harsh radiation environment in the inner detector requires a significant amount of material. This material causes many electrons to lose most of their energy before reaching the electromagnetic calorimeter and approximately 40% of photons convert into an electron-positron pair while traversing the inner detector. Figure 24 shows the integrated radiation lengths traversed by a straight track in the inner detector as a function of η, grouped by subdetector. There is a large increase in the amount of material for support structures around $|\eta| = 1.7$, where the inner detector transitions from barrel to endcap.

The inner detector is designed to work as a cohesive unit to provide complete tracking information for charged particulars, and the subdetectors are complementary. Table 5 summarizes the parameters of each of the subdetectors as well as the parameters of the combined inner detector. Table 6 summarizes the expected performance that can be achieved by the inner detector as a whole.

5.3.1 PIXEL DETECTOR

The Pixel detector is the closest detector to the interaction point and therefore is designed to provide extremely high granularity while simultaneously handling a very large dose of radiation from collisions. It consists of four layers of silicon pixel modules, each of which provides a precision measurement on the trajectory

Parameter	Inner Detector	Pixel	SCT	TRT
Inner Radius	3.1 cm	3.1 cm	30 cm	56 cm
$\|\eta\|$ Coverage	-	2.5	2.5	2.0
Cell Width	-	50 μm	80 μm	4 mm
Cell Length	-	400 μm	12 cm	70 cm
Material at $\|\eta\|$ = 0.0	0.3 X/X_0			
Material at $\|\eta\|$ = 1.7	1.2 X/X_0			
Material at $\|\eta\|$ = 2.5	0.5 X/X_0			
Number of Hits	48	4	8	36
Channels	99 M	92 M	6.3 M	350 k

Table 5: A summary of the parameters of the inner detector and each of the subdetectors [13].

of any charged particle. In the barrel region, the four layers are located at radial distances of 31 mm, 51 mm, 89 mm, and 123 mm. The three outer layers also include endcap elements, illustrated in Figure 21, which are located at 495 mm, 580 mm, and 650 mm away from the interaction point.

The pixel sensor technology uses a p-n junction of n-type bulk that contains both p^+ and n^+ impurities. This combination is crucial in maintaining performance after a significant radiation dose, as the n^+ implants allow the sensor to continue function after the n-type bulk has been converted to a p-type bulk by the accumulation of radiation. In either configuration, when a charged particle passes through the bulk, it ionizes thousands of electron-hole pairs. The electrons and holes are pulled in opposite directions by the electric field established between the anode and cathode of the junction, which then produces a current that can be measured and recorded by readout electronics.

The size of the pixels in the original three layers are 50 μm x 400 μm in the $r - \phi$ and z directions, respectively. Those pixels are bump-bonded to front-end readout chips, the FE-I3, which contains a total of 2880 pixels per chip. In the three original pixel layers, the chips are grouped into modules composed of 16 chips each with 46,080 pixels per module and a total size of 20 mm x 60 mm x 250 μm. The modules are further arranged into long rectangular structures that run parallel to the beamline called staves. By tiling several staves with an offset of 20°, the stave geometry provides full azimuthal coverage in the barrel region while accommodating the readout and cable systems. The endcap regions are instead arranged into petals and then into wheels. This arrangement can be seen in Figure 25 which shows a computer-generated, cut-away image of the outer three layers of the pixel detector. Together these three layers contain 1744 modules between the barrel and two endcap sections.

The innermost layer, the IBL, was added during the long shutdown before Run 2, and provides the fourth track measurement. It was inserted directly into the existing pixel detector by removing the existing beam pipe and replacing it with a significantly smaller version. This insertion can be seen in action in Figure 26,

Parameter	Particle	Value
Reconstruction Efficiency	Muon, $p_T = 1$ GeV	96.8%
	Pion, $p_T = 1$ GeV	84.0%
	Electron, $p_T = 5$ GeV	90.0%
Momentum Resolution	$p_T = 1$ GeV, $\lvert\eta\rvert \approx 0$	1.3%
	$p_T = 1$ GeV, $\lvert\eta\rvert \approx 2.5$	2.0%
	$p_T = 100$ GeV, $\lvert\eta\rvert \approx 0$	3.8%
	$p_T = 100$ GeV, $\lvert\eta\rvert \approx 2.5$	11%
Transverse IP Resolution	$p_T = 1$ GeV, $\lvert\eta\rvert \approx 0$	75 μm
	$p_T = 1$ GeV, $\lvert\eta\rvert \approx 2.5$	200 μm
	$p_T = 1000$ GeV, $\lvert\eta\rvert \approx 0$	11 μm
	$p_T = 1000$ GeV, $\lvert\eta\rvert \approx 2.5$	11 μm
Longitudinal IP Resolution	$p_T = 1$ GeV, $\lvert\eta\rvert \approx 0$	150 μm
	$p_T = 1$ GeV, $\lvert\eta\rvert \approx 2.5$	900 μm
	$p_T = 1000$ GeV, $\lvert\eta\rvert \approx 0$	90 μm
	$p_T = 1000$ GeV, $\lvert\eta\rvert \approx 2.5$	190 μm

Table 6: A summary of the expected performance of the combined inner detector [17]. Included are the reconstruction effiencies for multiple particle types as well as the momentum and IP resolution for various momenta.

which emphasizes the extreme precision required to place the the 70 cm long layer with only 2 mm of clearance. The IBL was commissioned to provide continued tracking robustness and high precision in the higher luminosity environment of Run 2 [18]. The proximity of this layer to the collisions necessitated an even higher granularity and better radiation hardness than the other pixel layers. And the strict space requirements to add an active sensing layer so close to the interaction point required a sensor chip with a much higher active area and a larger overall area per chip. These requirements led to the development of a new chip type, the FE-I4 (compared to the FE-I3 chips used in the original pixel detector) with improved radiation hardness and a larger active footprint of 90%. The IBL is comprised of 448 of these individual chips arranged in 14 staves, with 26,880 pixels per chip and a chip size of 18.5 mm x 41.3 mm x 200 μm. The staves, like in the other layers of the pixel detector, are offset by 14°to provide full azimuthal coverage. This arrangement can be seen in Figure 27, which shows two computer-generated images of the IBL geometry and includes the some of the remaining pixel layers.

5.3.2 SEMICONDUCTOR TRACKER

The SCT, the subdetector which immediately surrounds the Pixel detector, provides additional discrete measurements of the trajectory of a charged particle. Because the SCT is further away from the interaction point, the spatial resolution

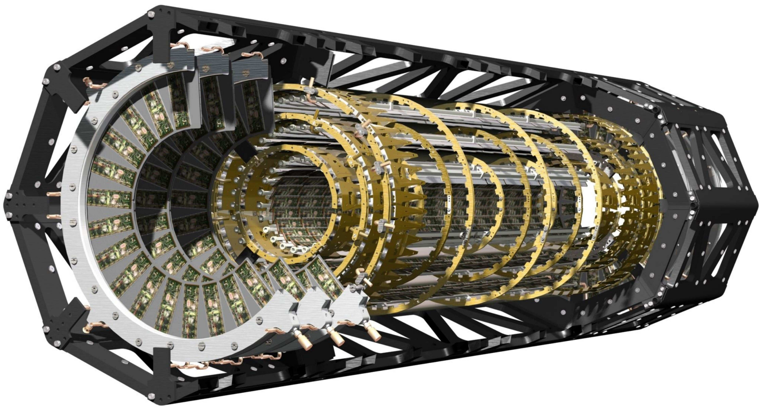

Figure 25: A cut away image of the outer three layers of the pixel detector.

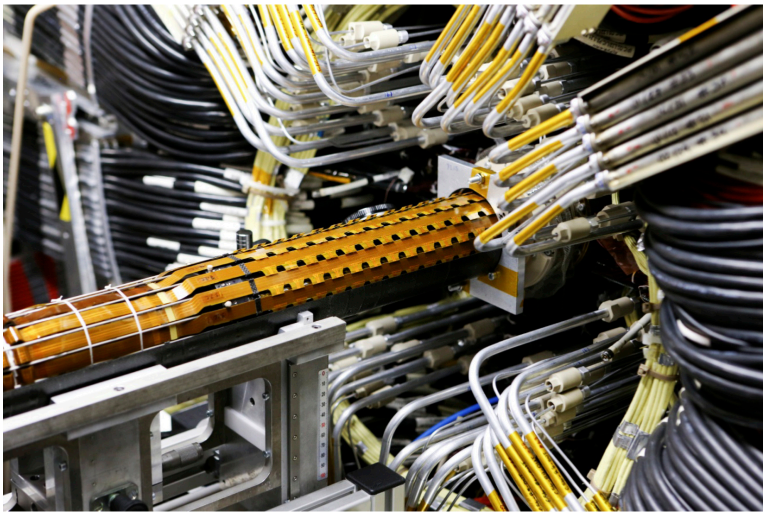

Figure 26: An image of the insertion of the IBL into the current pixel detector.

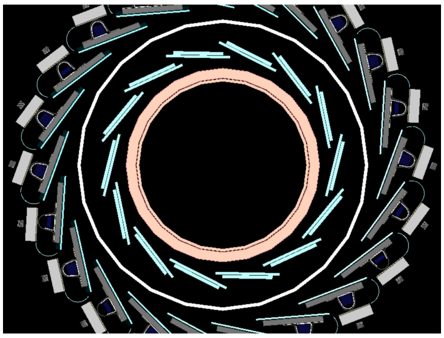

(a)

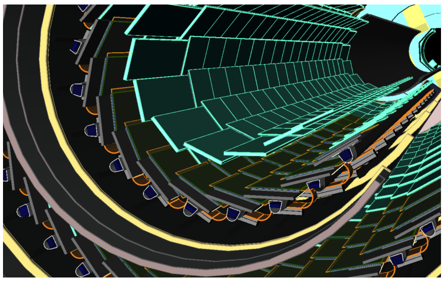

(b)

Figure 27: A three-dimensional computer-generated image of the geometry of the IBL with a view (a) mostly transverse to the beam pipe (b) mostly parallel to the beam pipe.

does not need to be as high as in the pixel detector, and so the SCT uses microstrips instead of pixels. Although pixels provide a more accurate measurement, the number of pixels and readout channels required to cover the cylindrical area at the radius of the SCT layers would be prohibitively complicated and expensive.

Each individual silicon strip sensor contains 768 individual readout strips with a total area of 6.36 cm x 6.40 cm and a pitch of 80 μm. Pairs of these sensors are then bonded together to form a combined strip with a length of 12.8 cm. Two of these combined strips are then placed back to back with a relative tilt of 40 mrad. This geometry is illustrated in an expanded view in Figure 28. The purpose of angular offset of the consecutive layers is to allow the strip sensor areas to more accurately measure the position of a particle by comparing the overlap of the two strips which were traversed by a track.

Four of these double layers are placed in the barrel region, with radii of 284 mm, 355 mm, 427 mm, and 498 mm. Together these layers provide eight additional measurements for each track that traverses the central $|\eta|$ region. In the endcap region, the layers are arranged in wheels, with the double layers similarly offset to provide improved resolution. With these configurations, the SCT achieves a spatial resolution of 17 μm in the $r - \phi$ direction and 580 μm in the z direction.

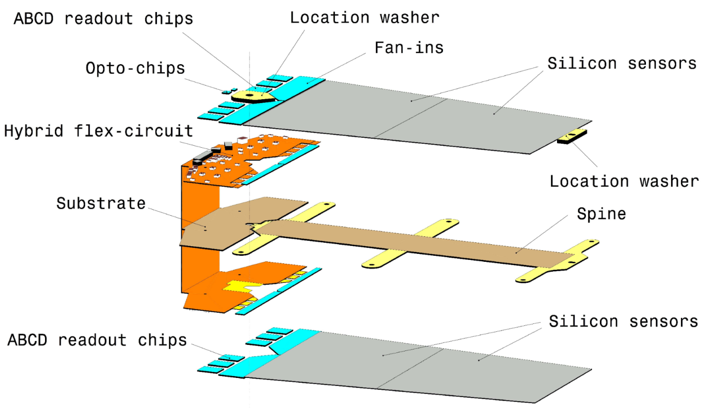

Figure 28: An expanded view of the geometry of the SCT double layers in the barrel region.

5.3.3 TRANSITION RADIATION TRACKER

The final component of the inner detector, the TRT, provides continuous tracking using straw drift tubes. The tubes are made of Kapton and aluminum with a diameter of 4 mm and are filled with a gas mixture of 70% Xe, 27% CO_2, and 3% 0_2. At the center of each tube is a gold-plated anode tungsten wire 30 μm in diameter. When a charged particle passes through these tubes, it ionizes the gas within. The ions produced drift in the electric field established between the wire and the tube wall, and the large electric field near the wire produces avalanche multiplication and results in an electric current on the wire that is read out by the electronics and provides a track measurement. The time it takes the ionization to drift to the wire can be used to estimate the distance from the wire that the particle passed through the tube; this gives a resolution on the distance of approximately 130μm. Combining several such measurements between consecutive hits in the TRT tubes allows the trajectory of the particle to be reconstructed with much better resolution than is available in each individual tube.

In addition to the continuous tracking, the detector can use transition radiation produced when a particle passes between the layers to distinguish between electrons and heavier charged particles. The space between the tubes is filled with CO_2, and so has a different dielectric constant than the gas within the tubes which contains Xe. At the transition between those media, a relativistic particle emits radiation proportional to γ, so inversely proportional to mass at a fixed momentum. The photons produced in this transition then produces an ionization cascade which is significantly larger than the signal for the minimally-ionizing charged particles. To distinguish between these two cases, the TRT defines two signal thresholds, a low threshold for the typical signal produced by a minimally ionizing particle (MIP) and a high threshold for the the signal produced by transition radiation. A high momentum electron is expected to produce approximately 7 to 10 high threshold hits as it traverses the TRT, and thus these hits provide a way to distinguish electrons from other charged particles.

The TRT contains 351,000 tubes in total, divided between the barrel and endcap regions. In the barrel region, the tubes are 144 cm long and arranged in 73 layers parallel to the beampipe. In the endcap region, the tubes are 37 cm long and arranged in 160 layers transverse to the beampipe. These configurations can be seen in Figure 22 and Figure 23. With this geometry the TRT achieves a resolution of 130 μm in the $r - \phi$ direction.

5.4 CALORIMETRY

The combination of calorimeter systems used in ATLAS can measure the energy of electrons, photons, hadrons, and hadronic jets with complete coverage up to $|\eta| < 4.9$ and across ϕ. Unlike the inner detector, the calorimeters are capable of measuring neutral particles. To accomplish precision measurements of these particle types, the ATLAS calorimeter system uses four individual calorimeters, a LAr electromagnetic calorimeter in the barrel region, a tile hadronic calorimeter in the barrel region, a LAr hadronic endcap calorimeter, and a LAr forward calorimeter. Together these provide hermetic coverage for the ATLAS detector. The configuration of these calorimeters is illustrated in Figure 29. **Note: I could make this section much longer. It might be nice to include a more complete description of showers for example. I will extend this section if there is space at the end.**

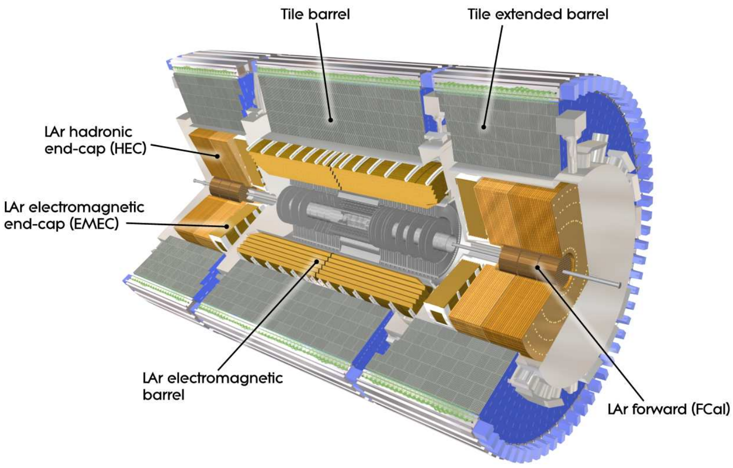

Figure 29

The calorimeters are designed to absorb and measure the energy carried by a particle, and completely stop the particle's propagation in the process. This requires a significant amount of material to provide interactions. These interactions then produce secondary particles, which can produces secondary particles in turn, and thus form a cascade of particles called an electromagnetic (EM) or hadronic shower, depending on the governing mechanism. Electromagnetic and hadronic showers have very different properties and require different technologies to measure them accurately. All of the calorimeters in the ATLAS calorimeter system are sampling calorimeters: they use alternating layers of absorbing and active material. The dense absorbing layers initiate the showers while the active layers measure the energy of the produced particles. A fraction of the energy is lost in the inactive layers, so the energy measurement from the active layers has to be corrected to estimate the actual energy of the particle.

The EM calorimeter provides around 20 radiation lengths (X_0) while the hadronic calorimeter provides around 10 interaction lengths (λ_0. As mentioned previously, radiation lengths measure the distance over which an electromagnetically interacting particle loses a characteristic fraction of its energy. Interaction lengths, on the other hand, measure the mean distance traveled by a hadronic particle before undergoing a nuclear interaction [6]. Figure 30 show the radiation lengths in the layers of the EM calorimeter in the barrel region as well as the interaction lengths for all calorimeters.

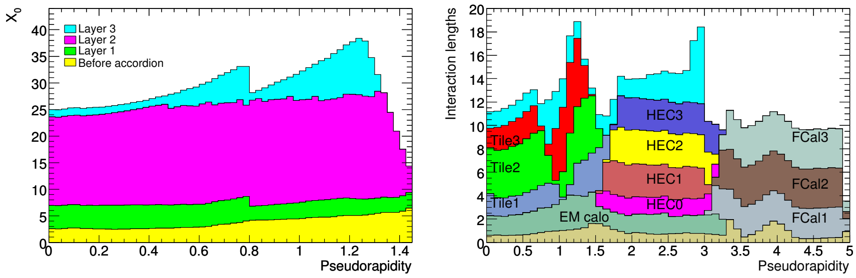

(a) (b)

Figure 30: The depth of (a) the electromagnetic barrel calorimeter in radiation lengths and (b) all calorimeters in interaction lengths as a function of pseudorapidity.

5.4.1 ELECTROMAGNETIC CALORIMETER

The electromagnetic calorimeters use alternating layers of liquid argon and lead in an accordion shape. The accordion shape provides complete coverage in the ϕ direction while also providing many alternating layers for the a particle to pass through. The configuration is detailed in Figure 31. When an electron or photon passes through the lead, it produces an electromagnetic shower. The particles produced in those showers then pass into and ionize the liquid argon; the ions produced can then be collected by an electrode in the liquid argon layer to provide the actual energy measurement.

The barrel region is covered by a presampler and three separate sampling layers with decreasing segmentation. The presampler is a thin layer of liquid argon which measures the energy of any electromagnetic showers which are initiated before the particle reaches the calorimeter due to interactions with the detector material. The first layer is the strip layer, which has fine segmentation in η to enhance the identification of shower shapes and to provide a precise η measurement for reconstructing photons and electrons. The strip layer has only 4 radiation lengths worth of material, and has a segmentation of $\Delta\eta = 0.003$ and $\Delta\phi = 0.1$. The second layer is also finely segmented, with a segmentation of $\Delta\eta = 0.025$ and $\Delta\phi = 0.025$, and a thickness of 16 X_0. This layer is designed

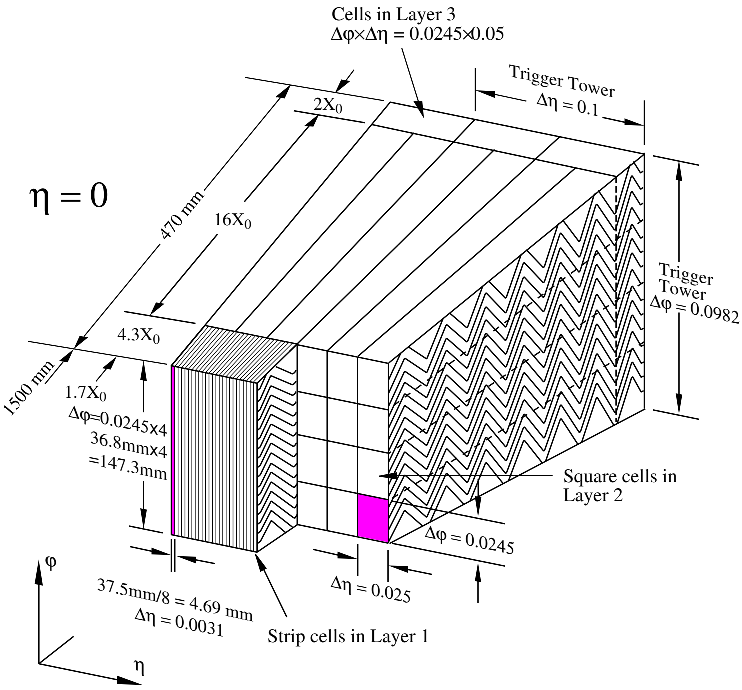

Figure 31: A schematic of the LAr calorimeter in the barrel region, highlighting the accordion structure.

to contain an electromagnetic shower and to measure the majority of the energy for photons and electrons. The third layer is only 2 X_0 thick and measures the energy of electromagnetic showers which leak out of the second layer, and helps to separate electromagnetic showers from hadronic showers. The structure of the LAr endcap calorimeter is similar except that the layers are arranged parallel to the beampipe to measure energy deposits from high η particles.

5.4.2 HADRONIC CALORIMETERS

The hadronic calorimeters use a few different technologies to satisfy the resolution demands in the different areas of the detector, and together they cover the region $|\eta| < 2.7$. In the barrel region, for $|\eta| < 1.7$, the hadronic calorimeters are constructed of alternating tiles of steel and plastic scintillator. Like in the electromagnetic calorimeter, the dense layer initiates a shower (in this case the dense layer is the steel and the shower is hadronic) of particles which pass into and ionize the following layer. The ionization in the plastic scintillator instead produces a light signal proportional to the amount of ionization produced by the shower, and this signal is measured using photomultipliers and provides the actual energy measurement. The construction of a tile in the calorimeter is shown Figure 32, which highlights the alternating layers of steel and scintillator.

This tile calorimeter, as well as the remaining hadronic calorimeters, have a much coarser granularity than the electromagnetic calorimeters. The high granularity is not needed for an accurate energy measurement, and the hadronic calorimeters are not designed to distinguish particle types like the electromag-

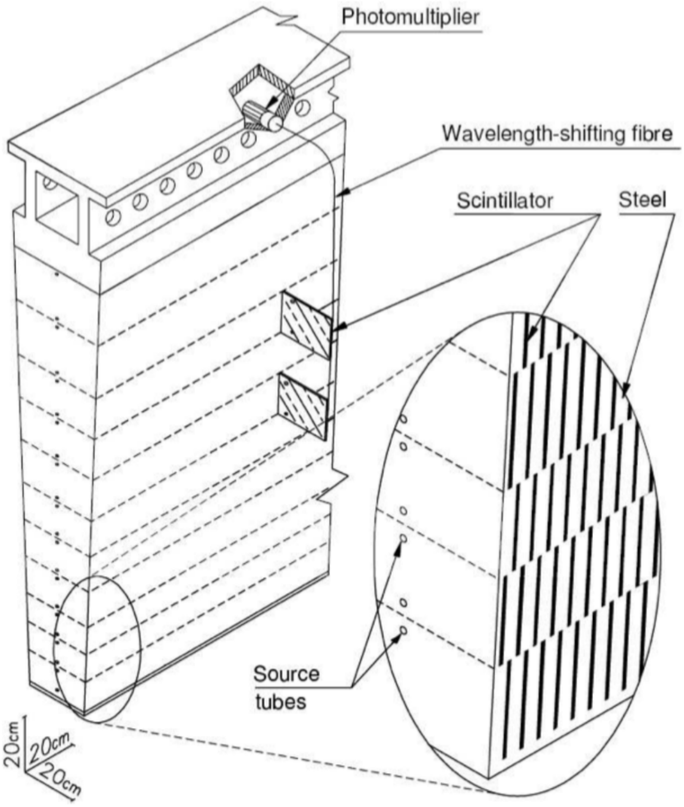

Figure 32: A schematic of a hadronic tile module which shows the alternating layers of steel and plastic scintillator.

netic calorimeters. The tile granularity is approximately $\Delta\eta = 0.1$ and $\Delta\phi = 0.1$, and the segmentation in depth and η is shown in Figure 33.

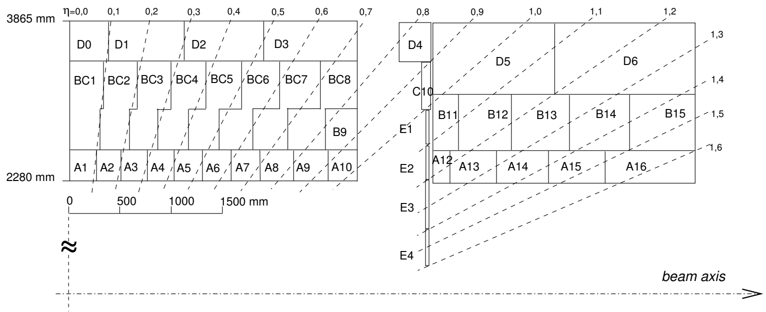

Figure 33: The segmentation in depth and η of the tile-calorimeter modules in the central (left) and extended (right) barrels.

The remaining hadronic calorimeters all use the same alternating, sampling structure but with different active and inactive materials. The hadronic endcap calorimeter covers the range of $1.5 < |\eta| < 3.2$ and uses an inactive layer of copper and an active layer of liquid argon. The forward calorimeter covers the range of $3.1 < |\eta| < 4.9$ and uses a dense matrix of copper and tungsten filled with liquid argon.

5.5 MUON SPECTROMETER

Among SM particles, only muons and neutrinos consistently pass through the calorimeters. Because the neutrinos are also electrically neutral, there is no feasible option to measure them directly in ATLAS. The muons, on the other hand, are charged and are thus already measured as a track in the inner detector. The muon spectrometer provides a way to consistently identify muon tracks and also a way to provide an additional measurement of their momentum.

The muon spectrometer contains four subdetectors that cover the barrel and endcap regions. In the barrel region, the muon spectrometer uses a combination of Resistive Plate Chambers (RPCs) and MDTs to provide both a coarse, fast measurement for triggering and a precise momentum measurement for offline event reconstruction. Similarly, in the endcap region, the TGCs, MDTs, and CSCs allow for both triggering and precise measurements. The CSCs are used only in the innermost layer of the endcap region between $2.0 < |\eta| < 2.7$ where the particle flux is too large for the MDTs to provide accurate measurements. The overall layout of the muon systems are shown in the cut-away diagram in Figure 34, and Figure 35 shows a precise schematic of the layout of each of the detecting elements. The geometric arrangement shown provides consistent coverage for muons produced up to $|\eta| < 2.7$, and takes full advantage of the bending of the muons in the toroidal magnetic field, described in Section 5.2, to measure their momentum. Figure 36 shows a cross-section of the arrangement of the muon spectrometer in the barrel; the layers are divided into eight small and eight large chambers that are overlapped to provide complete coverage in ϕ.

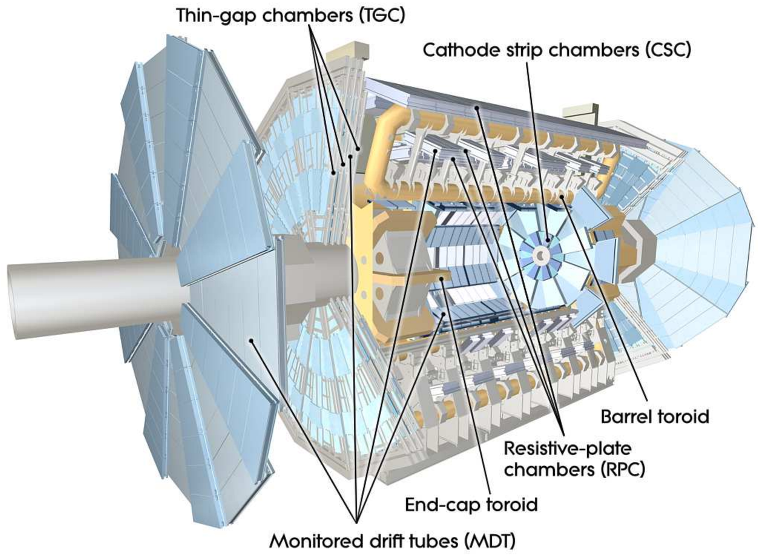

Figure 34: A cut-away diagram of the muon systems on ATLAS.

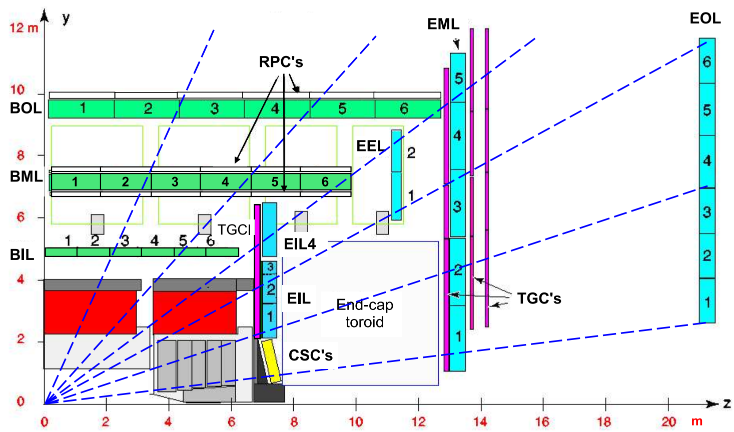

Figure 35: A quarter view of the muon spectrometer which highlights the layout of each of the detecting elements. The BOL, BML, BIL, EOL, EML, and EIL are all MDT elements, where the acronyms encode their positions.

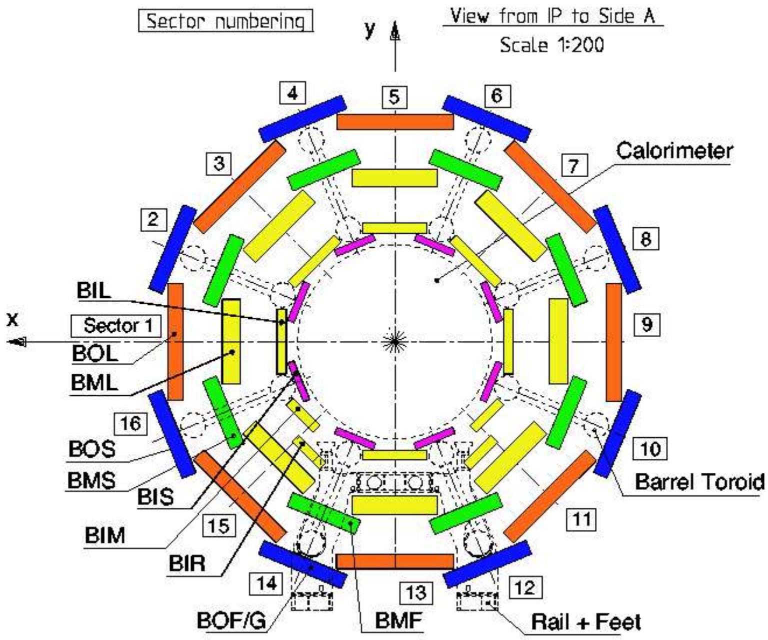

Figure 36: A schematic of the cross-section of the muon spectrometer in the barrel region.

5.5.1 Monitored Drift Tube

The momentum measurements in the barrel region are provided by three consecutive layers of MDT elements, located at approximately 5 m, 7 m, and 9 m from the interaction point. Each of these layers is a composite of two multilayers of drift tubes: two layers of three to four layers of tubes, as shown in Figure 37. These aluminum tubes are 3 cm in diameter, with lengths between 0.9 and 6.2 m, and are filled with a mixture of $ArCO_2$ kept at 3 bar absolute pressure. A central tungsten-rhenium wire with a diameter of 50 μm runs along the length of the tube, and is kept at a potential of 3080 V.

A muon traversing these tubes ionizes the gas, and the ionization electrons then drift in the electric field toward the central wire. Close to the wire, the electric field is strong enough to cause the original ionization electrons to ionize additional electrons, producing an avalanche that can be measured as a current along the wire. The time of arrival of that current depends on how far the muon entered from the wire, and can be used to achieve a position resolution of 80μm in an individual tube. The combination of the measurements in the consecutive layers of tubes improves this position resolution to 35 μm transverse to the tubes, with a resolution of 1 m along the tube direction.

To achieve a good resolution over the entire length of a muon track, the relative positions of the tubes of the muon spectrometer must be known to an accuracy of 30μm. This is achieved by an optical laser alignment system placed in each of the individual chambers and throughout the cavern. These monitor any changes in position or alignment due to effects like gravitational sag, temperature shifts, and the magnetic field. The configuration of the alignment system within an individual chamber is also shown in Figure 36.

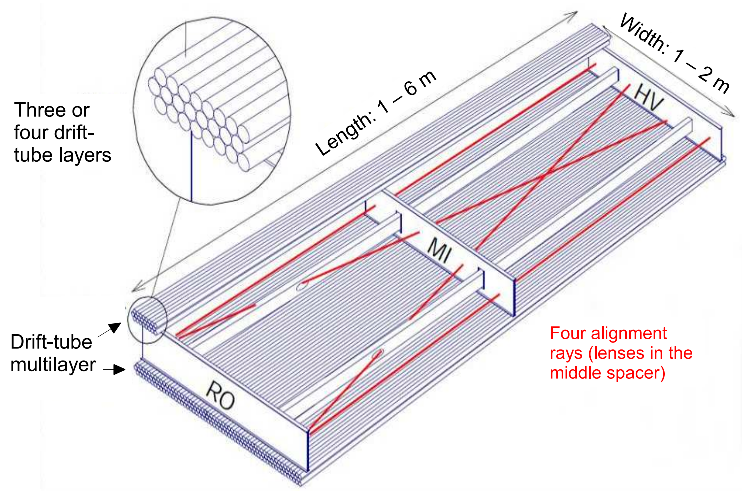

Figure 37: A schematic of a single MDT chamber, which shows the multilayers of drift tubes as well as the alignment system.

5.5.2 Resistive Plate Chamber

The RPC is the outermost detecting layer in the muon spectrometer in the barrel region, and provides a fast measurement of the ϕ position of muons for triggering. The speed of the measurement, with a time resolution of just a few tens of nanoseconds, requires a poor spatial resolution of approximately 1 cm. There are three RPCs layers in the muon spectrometer, two located on either side of the central MDT layer and one located outside the final MDT layer, as shown in Figure 35. The RPCs consist of two layers of parallel plates filled with a gas mixture of $C_2H_2F_4$. A muon passing through these systems ionizes the gas, like in the MDT, which causes an avalanche of ionization electrons in the electric field maintained between the plates. Metal strips on the outside of the chamber capacitively couple to the accumulated charge, and are read out to measure the η and ϕ positions of the muon track.

5.5.3 Cathode Strip Chamber

The majority of the momentum measurements in the endcap region are provided by the MDTs. In the most forward region of the muon spectrometer, between $2.0 < \eta < 2.7$, the particle flux is very high due to contributions from low energy photons and neutrons. The MDT can only sustain a hit rate of approximately 150 Hz/cm^2 because of limitations in the drift times of the gas and the capacity of the readout electronics. The CSCs were designed to handle higher hit rates, up to 1000 Hz/cm^2, and provide the necessary coverage in that high flux region.

The CSC consists of several multiwire proportional chambers, where the wires are oriented in the radial direction out from the beampipe. There are eight large and eight small chambers, arranged to partially overlap in the ϕ direction, as shown in Figure 38. Like in the MDT, a muon traversing the system produces ionization in the gas; here, however, the ionization is collected on a number of wires. These wires couple to cathodes on the chambers which are segmented into strips in two directions. The relative amount of charge on each of the neighboring strips can be used to interpolate to the position of the muon in both η and ϕ.

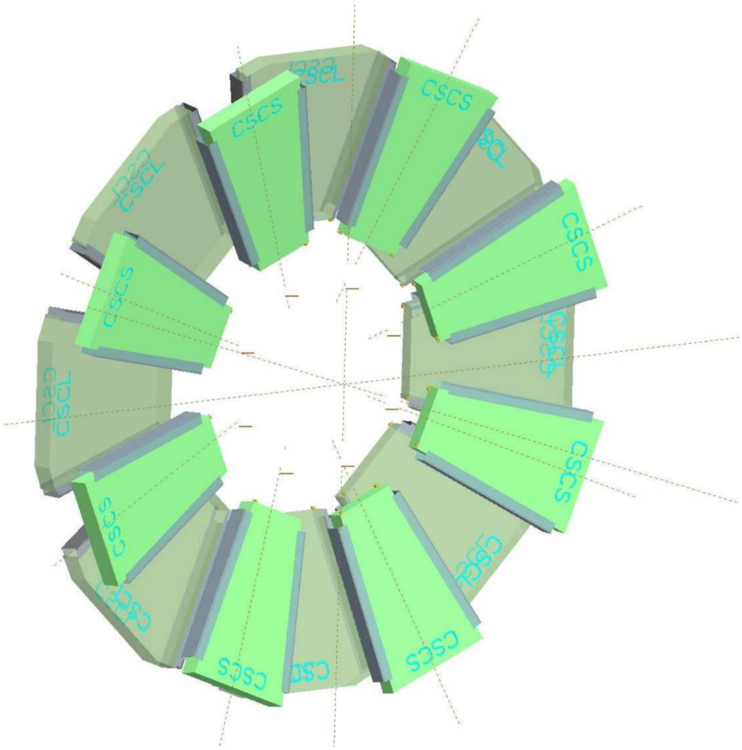

Figure 38: A schematic of the CSC endcap, showing the overlapping arrangement of the eight large and eight small chambers.

5.5.4 Thin Gap Chamber

Like in the barrel region, a separate, fast detector is required to provide position measurements of muons for trigger in the endcap region. This is provided by the TGC which consists of seven layers in the middle station of the endcap, two doublet layers and one triplet layer, and a single doublet layer in the inner endcap station. Figure 39 shows the arrangement of the triple and doublet layers of the TGCs.

Like the CSCss, the TGCs are multiwire proportional chambers with a wire-to-cathode distance of 1.4 mm and a wire-to-wire distance of 1.8 mm. Readout strips on the outside of the chambers run perpendicular to the wires, and couple to the charge collected on the wires to provide a position measurement in the η direction. The current induced on the wires is also readout to provide a position measurement in the ϕ direction. The high electric field and small wire-to-wire distance give it the required good time resolution to be used for triggering events.

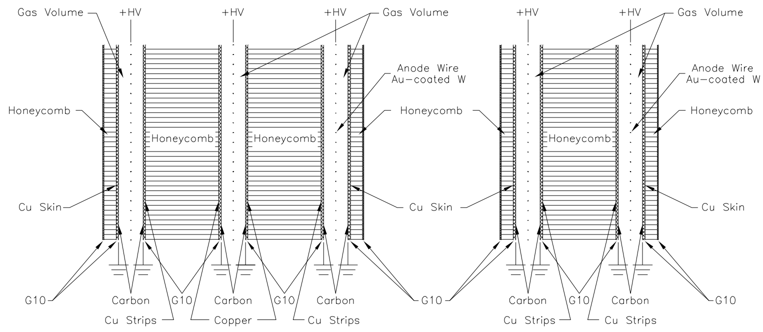

Figure 39: A schematic of the TGC doublet and triplet layers.

5.6 TRIGGER

It is not possible for the detector and the associated computing systems to record the terabytes of data that the 40 MHz event rate produces every second. Instead, a small fraction of these events are selected by the trigger system to be recorded and later analyzed. Selecting interesting events at such a high rate poses a significant challenge for the both the detector design and the implementation of a trigger decision and data acquisition system. The trigger must balance the time needed to decide to keep an event, to avoid losing information, with the filtering accuracy to consistently select a full menu of physics events that can be used for the wide array of searches and measurements targeted by ATLAS.

The ATLAS trigger system, as of Run 2, consists of two levels of decision making. The first level, referred to as L1, is hardware based and uses inputs from a subset of the detector elements to narrow the considered event rate from the original 40 MHz down to 100 kHz. The 100 kHz rate is the maximal rate that the event information can be transferred from the detector. The second, software-based level, referred to as the HLT, makes the final decisions on which events to keep for analysis and selects a rate of around 1 kHz. The collection of selection criteria used to make the L1 decisions feed into subsequent selection criteria in the HLT, and the set of these combinations of L1 and HLT criteria from the trigger menu which defines exactly what events are recorded on ATLAS. The trigger menu used for 2015 data collection is shown in Table 7, which summarizes the selection requirements at both levels and additionally shows the peak measured rates contributed by each.

At L1, the trigger system uses information primarily from the calorimeters and muon spectrometer to select high p_{T} jets, electrons, photons, and muons. The electromagnetic calorimeter uses reduced granularity energy measurements as well as isolation requirements to select electrons and photons. The hadronic calorimeter also uses a combination of reduced granularity energy measurements and isolation to select high momentum jets and hadronically decaying tau leptons.

The calorimeters are also used to provide triggers based on missing energy: the coarse granularity energy measurements are used to calculate a directional sum of energies and to trigger on a significant imbalance. Only the RPCs and

Trigger	Typical offline selection	Trigger Selection		Level-1 Peak Rate (kHz)	HLT Peak Rate (Hz)
		Level-1 (GeV)	HLT (GeV)	$L = 5 \times 10^{33}$ $\mathrm{cm}^{-2}\mathrm{s}^{-1}$	
Single leptons	Single iso μ, $p_{\mathrm{T}} > 21$ GeV	15	20	7	130
	Single e, $p_{\mathrm{T}} > 25$ GeV	20	24	18	139
	Single μ, $p_{\mathrm{T}} > 42$ GeV	20	40	5	33
	Single τ, $p_{\mathrm{T}} > 90$ GeV	60	80	2	41
Two leptons	Two μ's, each $p_{\mathrm{T}} > 11$ GeV	2×10	2×10	0.8	19
	Two μ's, $p_{\mathrm{T}} > 19, 10$ GeV	15	18, 8	7	18
	Two loose e's, each $p_{\mathrm{T}} > 15$ GeV	2×10	2×12	10	5
	One e & one μ, $p_{\mathrm{T}} > 10, 26$ GeV	20 (μ)	7, 24	5	1
	One loose e & one μ, $p_{\mathrm{T}} > 19, 15$ GeV	15, 10	17, 14	0.4	2
	Two τ's, $p_{\mathrm{T}} > 40, 30$ GeV	20, 12	35, 25	2	22
	One τ, one μ, $p_{\mathrm{T}} > 30, 15$ GeV	12, 10 (+jets)	25, 14	0.5	10
	One τ, one e, $p_{\mathrm{T}} > 30, 19$ GeV	12, 15 (+jets)	25, 17	1	3.9
Three leptons	Three loose e's, $p_{\mathrm{T}} > 19, 11, 11$ GeV	15, 2×7	17, 2×9	3	< 0.1
	Three μ's, each $p_{\mathrm{T}} > 8$ GeV	3×6	3×6	< 0.1	4
	Three μ's, $p_{\mathrm{T}} > 19, 2 \times 6$ GeV	15	18, 2×4	7	2
	Two μ's & one e, $p_{\mathrm{T}} > 2 \times 11, 14$ GeV	2×10 (μ's)	2×10, 12	0.8	0.2
	Two loose e's & one μ, $p_{\mathrm{T}} > 2 \times 11, 11$ GeV	2×8, 10	2×12, 10	0.3	< 0.1
One photon	one γ, $p_{\mathrm{T}} > 125$ GeV	22	120	8	20
Two photons	Two loose γ's, $p_{\mathrm{T}} > 40, 30$ GeV	2×15	35, 25	1.5	12
	Two tight γ's, $p_{\mathrm{T}} > 25, 25$ GeV	2×15	2×20	1.5	7
Single jet	Jet ($R = 0.4$), $p_{\mathrm{T}} > 400$ GeV	100	360	0.9	18
	Jet ($R = 1.0$), $p_{\mathrm{T}} > 400$ GeV	100	360	0.9	23
$E_{\mathrm{T}}^{\mathrm{miss}}$	$E_{\mathrm{T}}^{\mathrm{miss}} > 180$ GeV	50	70	0.7	55
Multi-jets	Four jets, each $p_{\mathrm{T}} > 95$ GeV	3×40	4×85	0.3	20
	Five jets, each $p_{\mathrm{T}} > 70$ GeV	4×20	5×60	0.4	15
	Six jets, each $p_{\mathrm{T}} > 55$ GeV	4×15	6×45	1.0	12
$b-$jets	One loose b, $p_{\mathrm{T}} > 235$ GeV	100	225	0.9	35
	Two medium b's, $p_{\mathrm{T}} > 160, 60$ GeV	100	150, 50	0.9	9
	One b & three jets, each $p_{\mathrm{T}} > 75$ GeV	3×25	4×65	0.9	11
	Two b & two jets, each $p_{\mathrm{T}} > 45$ GeV	3×25	4×35	0.9	9
$b-$physics	Two μ's, $p_{\mathrm{T}} > 6, 4$ GeV plus dedicated b-physics selections	6, 4	6, 4	8	52
Total				70	1400

Table 7: The trigger menu for the 2015 data collection with $L = 5x10^{33}\mathrm{cm}^{-2}\mathrm{s}^{-1}$. Both the L1 and HLT selection requirements and their trigger rates are shown measured at the specified luminosity are shown. The typical offline selections represent a typical set of offline requirements imposed after the trigger in an analysis.

TGCs muon subdetectors contribute to the decision at L1, and are used to identify high momentum muons. The contributions to the triggering rate of the various types of L1 triggers are shown in Figure 40. The total rate is indicated in black and is lower than the sum of individual rates because their is significant overlap between different trigger channels. The majority of the rate comes from lepton and photon triggers.

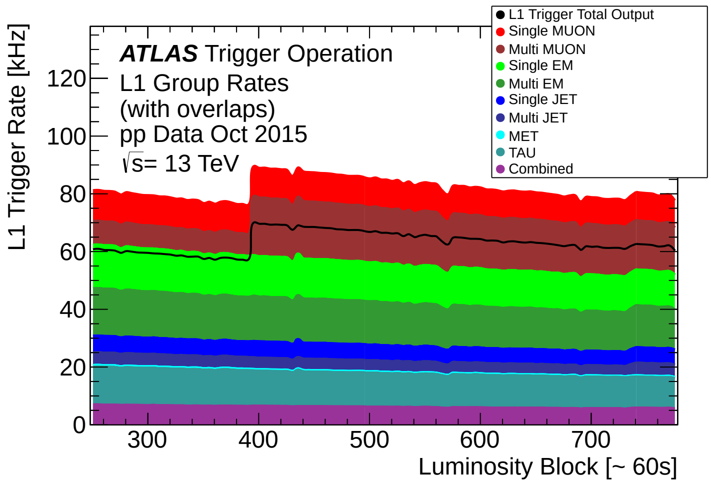

Figure 40: The L1 Trigger rate broken down into the types of triggers as a function of the luminosity block for the 2015 data collection period.

After an event is chosen by the L1 trigger, the detector measurements from the bunch crossing which fired the trigger is read out from the front-end electronics and stored on read-out boards. This inclusive information is necessary to make more the more precise event selections than is possible with the reduced information at L1. The HLT then uses this information with software algorithms to decide whether or not to permanently record the event. The L1 trigger also forwards which decision was made and Region of Interests (RoIs) to the HLT, which allows the HLT to focus on particular algorithms and particular sections of the detector to greatly improve the algorithmic selection speed. The additional information available to the HLT allows it to implement additional trigger targets, such as identified jets from the decays of b-hadrons. The contributions to the triggering rate of the various types of HLT triggers are shown in Figure 41.

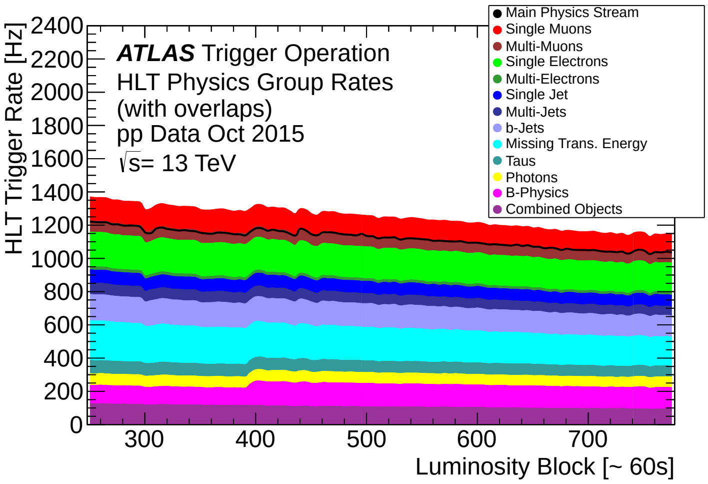

Figure 41: The HLT Trigger rate broken down into the types of triggers as a function of the luminosity block for the 2015 data collection period.

6 EVENT RECONSTRUCTION

The ATLAS experiment combines measurements in the subdetectors to form a cohesive picture of each physics event. The majority of particles that traverse the detector leave behind some combination of ionization hits in the tracking detectors or energy deposits in the calorimeters, and these measurements can be used to reconstruct physical quantities like the particle's energy, momentum, or trajectory. Even the type of the particle can be distinguished by comparing the various ways that different species of stable particles interact with the subdetectors. Reconstruction is the series of algorithms which take the electronic outputs of the detector and assigns them into individual physics objects. The physics objects summarize the properties of particles produced by the collision or subsequent decays, either for individual isolated particles like leptons, or for a collection of the cascade of products produced in the decay of an energetic hadron, called a jet. These are the objects and quantities most often used in analysis to make measurements of SM processes or to search for new physics.

6.1 CHARGED PARTICLES

As described in Section 5.3, charged particles that traverse the inner detector leave behind hits in the subdetectors. Each of these hits translates into a position measurement along the trajectory of that particle, with position resolutions depending on the subdetector that provided the measurement. Track reconstruction uses these position measurements to collect hits in consecutive layers of the detector into a trajectory consistent with a particle curving in a magnetic field [19, 20]. This reconstructed trajectory is called a track. The number of hits in the inner detector for each event makes a combinatorial method completely infeasible: the algorithms that form tracks must be significantly more intelligent so that event reconstruction does not exhaust computing resources.

The first and primary algorithm employed in track reconstruction is called the inside-out method, which begins with the assumption that the track originated from the interaction point. Its purpose is to identify primary particles, those which originate in the proton-proton collisions and with a lifetime long enough to reach the inner detector. Combinations of three hits are considered from measurements in the Pixel detector and the SCT, and form the seed for a track. Specifically, the seeding algorithm looks for a seed using three pixel hits, two pixel hits and one SCT hit, or three SCT hits. The seed is then extrapolated forwards and backwards into the Pixel and SCT detectors depending on the seed location, and hits in each layer are considered to be added to the track using a combinatorial Kalman filter [20]. After all of the silicon layers have been considered, tracks are filtered to reduce ambiguities from other nearby tracks or from combinatorial coincidences. Then the tracks are extended outwards into the TRT

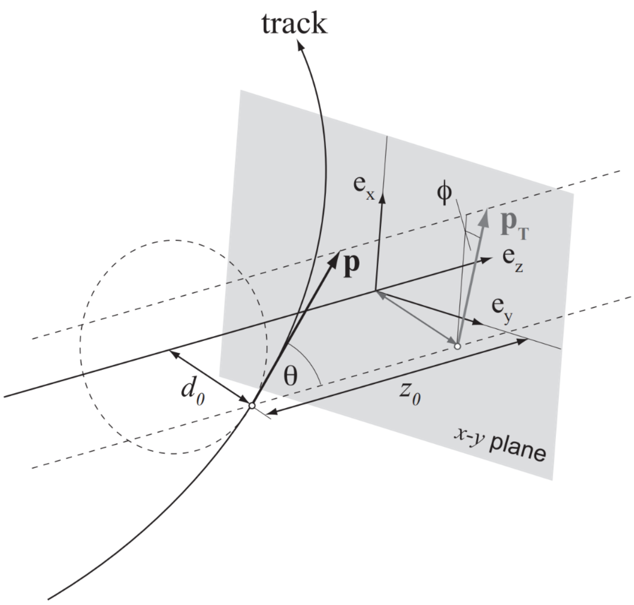

Figure 42: An illustration of the perigee representation of track parameters for an example track. The charge is not directly shown, but is indicated by the direction of curvature of the track [21].

in the same way. This algorithm is how the hits are chosen to be incorporated into a single track. Once the hits are collected, a fitting algorithm calculates the track parameters which best model the locations of the hits and their resolutions. The fitting uses five parameters, $(d_0, z_0, \phi, \theta, q/p)$, to specify a track in a perigee representation: d_0 and z_0 are the transverse and longitudinal impact parameters at the closest approach to the nominal beam axis, ϕ and θ are the usual angular coordinates, and q/p is the charge divided by the momentum. These parameters are illustrated in Figure 42. Those parameters directly determine the direction and momentum of the particle which produced the track.

This inside-out algorithm is complemented by an outside-in algorithm, which is used to find tracks from secondary particles, those produced in the decays or interactions of the primary particles inside the detector. As the name indicates, the outside-in algorithm begins by seeding tracks in the outermost layers of the inner detector, in the TRT. The seed in this case is formed by a segment in the TRT, and the track is propagated backwards into the SCT before being refitted to use all the included points. Some tracks are found with TRT segments only, which can result from interactions with the detector following the SCT. Figure 43 shows an example of the geometry of tracks formed by both algorithms, where the hits belonging to tracks found using the inside-out algorithm are highlighted in red, and the hits belonging to the tracks found using the outside-in algorithm are circled in black. The figure highlights the presence of a large number of both primary and secondary tracks in a single event, as well as the overall large number of hits present in the inner detector.

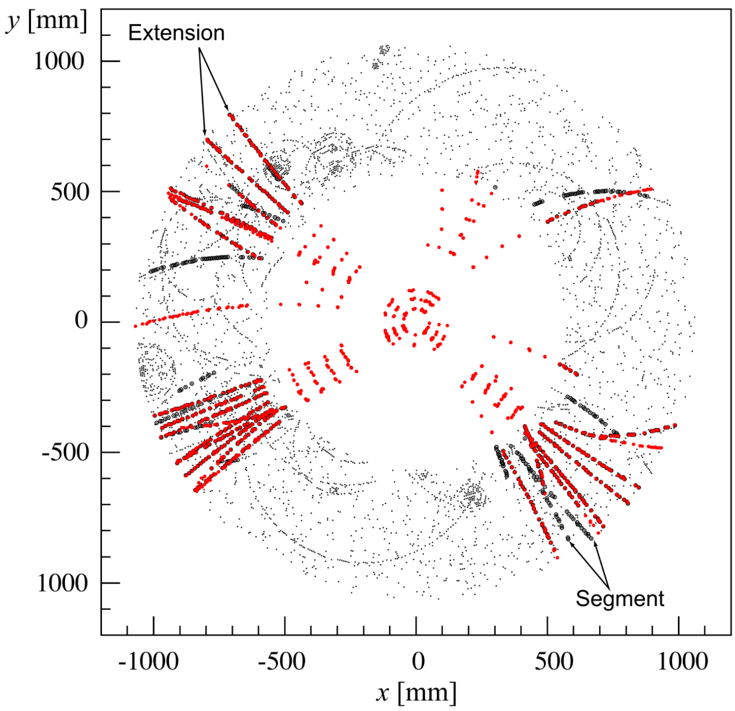

Figure 43: The x and y locations of the hits generated in a simulated $t\bar{t}$ event in the inner detector. The hits which belong to tracks formed using the inside-out algorithm are highlighted in red, while the hits which belong to tracks formed using the outside-in algorithm are circled in black.

The tracks resulting from these algorithms can be contaminated by nearby particles confusing the tracking algorithm in a high luminosity environment. For example, enough hits present in the inner detector can lead to fake tracks from combinations of hits from multiple individual tracks. Therefore, after the tracks are formed and fitted, additional quality requirements are imposed in order to reduce such backgrounds. Most tracking applications require at least seven silicon hits, that is, seven hits between the Pixel detector and SCT. Then the tracks are required to have at most two holes in the Pixel detector, where holes are non-existing but expected measurements in a layer of the subdetector. If the missing hit corresponds to an inactive module, however, it is not counted as a hole but instead as a hit for tracking as the lack of a measurement is expected in that case.

6.1.1 PIXEL NEURAL NETWORK

The hits in the Pixel detector are not typically confined to a single pixel, but rather the charge is spread over several pixels per layer which are grouped together into clusters. The clustering of these pixels for isolated tracks is relatively straightforward, but complications can arise in the high occupancy environment where hits from multiple particles can overlap in a single cluster. Figure 44 shows examples of clusters generated by a single isolated particle, two nearly overlapping particles, and a particle which emits a δ-ray. A δ-ray is a secondary

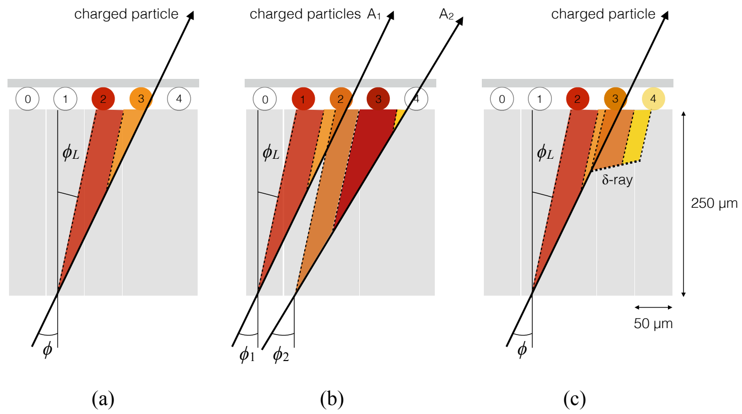

Figure 44: Examples of the clusters formed in a single layer of the pixel detector for (a) a single isolated particle, (b) two nearly-overlapping particles, and (c) a particle which emits a δ-ray [22].

electron which is generated with enough energy to escape a significant distance away from the original particle and to generate additional ionization.

A series of neural-networks analyzes the shape of the clusters to determine how many particles produced the cluster and to estimate the positions of each of the particles within the cluster. These allow for an identification of clusters caused by more than one particle or by a particle that emits a δ-ray. In a high-density tracking environment, the multiple position outputs can be used as the locations of individual hits to allow reconstruction of tracks which almost overlap and with a much better separation than is possible without the splitting of individual clusters.

6.1.2 PIXEL DE/DX

A hit in the Pixel detector corresponds to the voltage generated from ionization current rising above a threshold value that is tuned to consistently record the passing of MIPs. A larger amount of charge deposited results in a larger voltage, and a larger signal remains above the threshold for a longer period of time. The time over threshold (ToT) is read out of the Pixel detector, and can be used to provide a measurement of the charge deposited in each pixel. The charge measurements from each of the pixels included in a pixel cluster are summed to form one charge measurement per layer of the pixel detector. That charge measurement, combined with the angle of incidence of the track and the known sizes of each detector element, can be converted into a measurement of dE/dx, the ionization energy deposited per unit distance, measured in $\mathrm{MeVg^{-1}cm^2}$. The IBL only has sixteen available values (4 bits) of ToT to readout, compared to the 256 available values (8 bits) in the remaining pixel layers. To help alleviate this lack of range, the IBL also records if is in overflow: when the ionization is sufficient to generate a ToT above the largest value that can be recorded in the 4 bits.

The measurements across multiple layers are combined to form an average value of dE/dx for the track as a whole. Depending on where a charge particle is produced, it will traverse four Pixel layers and create four clusters on average. It can produce as few as two clusters in the Pixel detector if it passes through inactive modules, and as many as five if is in a region of the detector where multiple modules overlap. To reduce the influence of the typical long Landau tails of the distribution of dE/dx deposits [6], the average is calculated as a truncated mean of these clusters. The value measured in the IBL is removed if it is in overflow, as the measured value is not reliable in that case. If a track has five measurements in the pixel detector, the two highest cluster values are removed. If a track has two, three, or four measurements in the pixel detector, only the single highest cluster value is removed. The remaining values are averaged to form the pixel dE/dx.

6.1.3 VERTEX RECONSTRUCTION

A vertex represents the intersection of multiple tracks and corresponds to the location of an interaction. If at least two charged particles result from the interaction, the intersection of their resulting tracks reveals its position with high precision. Vertices are divided into two groups, primary vertices which correspond to the actual proton-proton collisions, and secondary vertices which correspond to decays of short-lived particles or interactions with the detector. Primary vertices are particularly important, as they can provide a precise location for the interaction which generated the observed particles. Understanding that location is crucial in understanding the geometry of the event.

Primary vertices are reconstructed by iteratively identifying seeds from reconstructed tracks [23]. Each track's extrapolated z position at the beamline forms a seed, and nearby tracks are fitted using that position as a point along their trajectory. The goodness of fit with that vertex is considered for each track, measured in χ^2. The final position of the vertex is determined by a fit to all of the considered tracks, where the contribution from each track is weighted according to the χ^2 compatibility with that vertex. Any tracks from this procedure that are displaced by more than 7σ from that vertex are removed from the fit and used to seed a new vertex. This procedure is iterated until no additional vertices can be found.

This procedure is typically performed twice. The first set of vertices is used to fit a profile for the beamspot, which indicates the position of the intersection of beams in that particular bunch crossing. The fitted beamspot then provides a constraint for the second attempt to locate primary vertices, where both the track fitting and seeding of vertices are required to be consistent with interactions occurring within the beamspot.

6.2 ELECTRONS AND PHOTONS

Electrons are measured as both a charged particle track and energy deposits in the electromagnetic calorimeter. Photons, on the other hand, leave energy deposits in the electromagnetic calorimeter but do not produce a corresponding track. Because the electromagnetic interactions with the calorimeter of both photons and electrons produces more photons and electrons, the behavior in the calorimeter is very similar and their is significant overlap in the reconstruction techniques for each.

The reconstruction of a photon or an electron in the calorimeter is based on clustering algorithms which identify groups of energy deposits [24–26]. For this purpose, the entire electromagnetic calorimeter is subdivided into a grid of 200 by 256 towers in the η and ϕ directions, respectively, where the individual grid units have a size of $\Delta\eta = 0.025$ and $\Delta\phi = 0.025$. These towers correspond to individual cells in the middle, coarsest layer of the EM calorimeter, and in the remaining layers the cells are grouped together cover the same area in $\eta - \phi$ space. The clustering begins by finding seeds with a sliding-window algorithm based on the towers: a window of 3 by 5 towers is formed and translated until the sum of the energy within the window is maximized. If that energy is above 2.5 GeV, then that region becomes a seed. The choice of 2.5 GeV was chosen to compromise between maximizing reconstruction efficiency while minimizing fake electron seeds from electronic noise or soft hadrons from additional interactions. The seeds are rejected if the energy measured in the hadronic calorimeter behind the seed is large, as this typically indicates a hadron rather than an electron or photon.

Next, the inner detector tracks within a cone of $\Delta R = 0.3$ are compared to the location and energy of the seed. Tracks are matched to the cluster if the extrapolation of the track to the energy-weighted center in the middle layer of the EM calorimeter falls within $\Delta\phi < 0.2$ in the direction of the curvature of the track or $\Delta\phi < 0.05$ in the direction opposite of the curvature of the track. If the seed matches with a track that originated from a primary vertex, the combination of track and electromagnetic cluster is reconstructed as an electron. If the seed matches with a track that did not originate from a primary vertex, then the electromagnetic cluster is reconstructed as a converted photon. And if there is no corresponding track in the inner detector, than the cluster is reconstructed as a photon.

After classification, the final clustering of the energy in the EM calorimeter calorimeter is performed. The classification must be done first, as the expected size of the energy deposits in the calorimeter are different for electrons and photons. In the barrel region, the final clusters for electrons are formed in rectangles of 3 towers in the η-direction and 7 towers in the ϕ-direction. This asymmetric window accounts for the curving of the produced charged particles only in the ϕ direction. For photons, the size of the rectangle is 3 towers by 5 towers. In the endcap region, all object types are clustered in rectangles of 5 towers by 5 towers, as the effect of the magnetic field curvature is less pronounced in this region. The sum of the energies in these clusters provide the final energy measurement for the electron or photon.

6.2.1 PHOTON IDENTIFICATION

The original requirement for constructing a photon cluster, a significant energy deposit in the electromagnetic calorimeter without a corresponding track or energy deposits in the hadronic calorimeter, is already effective in identifying photons. However, there is a significant background for prompt photon production from the decays of pions, $\pi^0 \to \gamma\gamma$. These can be identified using the shape of the cluster in the narrow η granularity in the first layer of the EM calorimeter.

6.2.2 ELECTRON IDENTIFICATION

Prompt electrons have a number of backgrounds, such as secondary electrons from hadron decays or misidentified hadronic jets, that can be rejected using additional information from the EM calorimeter and the inner detector. The most basic level of electron identification, referred to as Loose, makes requirements on the shower shapes in the high granularity first layer of the EM calorimeter as well as the quality of the inner detector track. It also requires a good match between the track and the calorimeter energy deposits and a small fraction of energy in the hadronic calorimeter behind the electromagnetic cluster. ATLAS defines several additional working points, including Medium and Tight, which provide progressively lower background rates for electrons by imposing additionally strict requirements on the above variables as well as new requirements like the impact parameter of the inner detector track or the comparison of the cluster energy to the momentum in the inner detector.

6.3 MUONS

Muons produced in ATLAS first traverse the inner detector and leave behind a track as described in Section 6.1. The muon then passes through the calorimeter, leaving behind a small, characteristic amount of energy, and then passes through the muon spectrometer where it produces hits in the MDTs or CSCs. Muon tracks are formed from local segments of hits in each layer of the MDTs or CSCs, and then the final muon spectrometer track is formed by combining the two local segments [27]. When a track is reconstructed in both the inner detector and the muon spectrometer, the track is refitted to include the hits in both the inner detector and the muon spectrometer, and forms a combined muon.

In a few regions of the detector, a muon may fail to leave behind both a complete inner detector and muon system track. For a very small fraction of the acceptance of the muon system, there is only one layer of muon chambers and a global muon system track is not formed. In this case, as long as the track in the inner detector exists and geometrically matches to a segment, a segment-tagged muon is formed using momentum measurements from the inner detector. In the region where the muon system has coverage but the inner detector does not, $2.5 < |\eta| < 2.7$, a stand-alone muon is formed which uses only information from the muon system. And for muons produced within one of the few holes in the muon system, including $|\eta| < 0.1$, the characteristic energy deposits in the calorimeter can be used to tag an inner detector track as a calo-tag muon. These additional categories are used to achieve high efficiency over a larger range of acceptance, but the combined muons are the most reliable.

6.3.1 MUON IDENTIFICATION

The various types of muons are incorporated into three working points: Loose, Medium, and Tight, which reflect the increasing muon purity for each of the selections definitions. Tight muons include only combined muons with a good track fit quality and momentum resolution and at least two hits in a precision muon system layer. Medium muons include those in tight as well as combined muons with one precision hit and one precision hole, where hole is defined in the same way as in Section 6.1. The medium working point also includes standalone muons with $|\eta| > 2.5$ and at least two hits in precision layers. And finally the loose working point includes both medium and tight muons, but additional includes segment-tagged and calo-tagged muons in the region $|\eta| < 0.1$.

6.4 JETS

A jet does not directly correspond to a physical particle, unlike all of the reconstructed objects described above, but instead tries to capture the conical cascade of particles produced in the hadronization of a quark or gluon from the proton-proton collision. The hadronization process creates a very large number of collimated particles, with a high enough density that individually reconstructing all of the produced particles in the calorimeter is not possible within ATLAS. However most analyses are interested only in the kinematics of the particle which produced the cascade, rather than the individual products. Therefore, jets are a useful tool to measure the combined energy and direction of the ensemble of products and thus represents the kinematics of the original. Jet algorithms are very generic and can be used to group together a number of types of objects to form aggregate representations. For example, truth particles in simulation can be grouped in truth jets, or tracks from the inner detector can be grouped together to form track jets. This section, however, will focus on calorimeter jets which take topoclusters of energy deposits in the calorimeter as inputs and produce a combined object which represents the energy measured by the calorimeter and the location where it was deposited.

6.4.1 TOPOLOGICAL CLUSTERING

Hadrons often deposit their energy into multiple individual cells in both the electromagnetic and hadronic calorimeters. The purpose of topological clustering is to group cells in all three dimensions into clusters that represent a single energy deposit. The procedure must be robust enough to reject noise fluctuations in the cell energy measurements that can come from both electronic noise and additional low energy particles produced in pileup activity. The background level of calorimeter noise is called σ_{noise}, and is an important component of the topological clustering.

The topological clusters are formed in a three step process called the 4-2-0 threshold scheme, which uses three energy thresholds to build up a cluster from cells [28]. First, any cells with a measured energy above $4\sigma_{\text{noise}}$are identified as seed cells. The cells adjacent to the seed cells with a measured energy above $2\sigma_{\text{noise}}$are called secondary cells. All of the cells which are adjacent to a secondary cell with $E_{\text{cell}} > 2\sigma_{\text{noise}}$ are also labeled secondary cells. Tertiary cells are those immediately adjacent to a seed or secondary cell with a measured energy above zero. Adjacency in this sense is defined in three dimensions, cells are adjacent if they are neighbors within a layer but also if they have the same $\eta - \phi$ coordinates but are in adjacent layers or even in an adjacent layer in another calorimeter.

From these definitions, clusters are built by resolving the seeds in order of significance, the ratio $E_{\text{cell}}/\sigma_{\text{noise}}$. All adjacent secondary cells to the highest significance seed are added to that seed's topocluster, and any of those cells which would also have qualified as seeds are removed from the list of seeds. Once all of the secondary cells have been added, the tertiary cells are then added to that cluster as well. This procedure is then iterated until no seeds remain, forming the first round of topoclusters.

It is also useful to split topoclusters into multiples if local maxima are present within the topocluster, as clusters produced by multiple nearby particles can merge. The splitting process begins by finding local maxima cells in the middle layer of the calorimeters with a minimum energy of 500 MeV and at least four neighboring secondary cells. These requirements reduce the likelihood to split a cluster due to random fluctuations, as the middle layers provide the most reliable energy measurements. Cells between two local maxima can then be shared between two clusters to account for overlapping contributions from two particles. The energy sharing is weighted by the energy of each cluster as well as the distance of the cell to the centroid of that cluster.

The energies of all the cells in the cluster are then summed together to form the energy of that cluster. The energy needs to be corrected for the various losses expected in the calorimeter, as described in Section 5.4. The simplest correction, scaling the measured energy by the sampling fraction, brings the cluster energies to the EM scale. It is called the EM scale because it accurately describes the energy of electromagnetic showers.

Another scale is defined to improve accuracy for hadronic processes, the local cluster weighted (LCW) scale, that helps to correct for the expected variations in hadronic energy deposits. The LCW correction first determines if the shower is hadronic or electromagnetic, based on the depth of the shower and the cluster energy density. For hadronic showers, the energy is corrected for calorimeter non-compensation, an effect which reduces the measured energy of hadronic showers because some of the energy goes into invisible processes like the break up of nuclei. All clusters are then corrected for energy that may be deposited in uninstrumented regions in that cluster's location in the calorimeter, and they are also corrected with an estimate of how much energy falls outside the extent of the cluster based on its shape and the deposit type.

6.4.2 JET ALGORITHMS

Using the topological clusters as inputs, a jet algorithm groups them together into a collection of adjacent energy deposits that is intended to correspond to a single process [29]. Jet algorithms need a few key characteristics to be usable for physics analysis. First, the jets produced by the algorithm should have little dependence on the addition of soft particles to the event (infrared safety), as a negligible addition of energy should not significantly modify the event topology. Similarly, the jets produced by the algorithm should also not significantly depend on mostly collinear splitting of an input particle (collinear safety); that is, a single quark replaced by two, parallel quarks with half the original's momentum should not change the resulting jets, which are intended to capture only the properties of the aggregate and not those of individual particles. And finally the algorithm needs to be sufficiently simple and fast to be used for the large rate of collected proton-proton collisions on ATLAS.

The most commonly used algorithm on ATLAS that satisfies these requirements is called the anti-k_t algorithm, and is discussed in further detail in Reference [30]. The anti-k_t, in brief, relies on iteratively combining the input objects that are closest together, where closest is defined by a particular distance metric, $d_{i,j}$, where the index i represents the combination constructed so far and j is an additional object being considered. The combinations stop when the closest remaining object is the beam itself, where the distance to the beam is called $d_{i,B}$. An entire class of algorithms follows this procedure with the following distance metrics

$$d_{i,j} = \min(k_{ti}^{2p}, k_{tj}^{2p}) \frac{\Delta_{ij}^2}{R^2} \tag{18}$$

$$d_{i,B} = k_{ti}^{2p} \tag{19}$$

where $\Delta_{i,j} = (y_i - y_j)^2 + (\phi_i - \phi_j)^2$, k_{ti} is the transverse momentum of the object, y is the rapidity, and p is a parameter of the algorithm. Anti-k_t is the particular case where $p = -1$, and is a choice that results in an algorithm that is both infrared and collinear safe.

The algorithm is repeated until there are no input objects remaining, which results in a series of jets. Each jet has a complete four momentum from the combination of its input clusters, where the combinations assume a mass of zero. The jet energies then need to be calibrated to attempt to match the energy of the object which produced the jet.

6.4.3 JET ENERGY SCALE

Though the LCW scheme attempts to correct the topoclusters to reflect the true deposited energy, the correction does not fully account for energy lost within the calorimeters. Because of these effects, the original reconstructed jet energy does not reflect the true energy of the particle which initiated the jet. Therefore it is necessary to additionally correct the reconstructed jet itself, in addition to the corrections on the inputs. This correction is referred to as the JES, which combines several individual steps of calibration [31].

The first calibration step corrections the direction of the jet to ensure that it points back to the primary vertex. Next, the energy of the jet is corrected for pileup by subtracting the expected contribution from pileup based on the momentum, η, and area of the jet as well as the number of reconstructed vertices and expected number of interactions per crossing. The largest single correction is the absolute η and scale correction, where the jet energy and pseudorapidity is corrected to attempt to match the energy and pseudorapidity of the parton which produced it. This correction is measured in simulation by comparing the reconstructed jet energies to the energy of the truth particle which produced it. However the simulation is not relied on alone to estimate this correction, and an additional step applies an additional energy correction based on in-situ measurements in data. These corrections come from various techniques which measure jet energies indirectly by balancing them with other, well-measured objects. In the central region ($|\eta| < 1.2$), jets are balanced against photons and the leptonic decays of Z bosons and high momentum jets ($p_T > 210$ GeV) are also balanced against multiple smaller jets in multijet events. Jets at larger pseudorapidities, above $|\eta| = 1.2$, are calibrated by balancing with lower pseudorapidity jets.

These steps introduce a number of systematic uncertainties, referred to as the JES uncertainty. The largest of these comes from the in-situ measurements, which are statistically limited in measuring high momentum and high pseudorapidity jets. The total, fractional JES uncertainty is shown as a function of p_T in Figure 45. The uncertainty falls to a minimum value of just over 1.0% around a few hundred GeV, and rises again at high momentum because of the difficulty of measuring jet balance in data above 2-3 TeV. The uncertainty is also minimized at low $|\eta|$, and grows at large $|\eta|$ again where making in-situ measurements is difficult. This technique does not actually provide a measurement of the uncertainty for the highest energy jets, above 3 TeV, because there are not enough measured data events to provide them. An alternative method for deriving the JES and JES uncertainty that can be used even for very high p_T jets will be discussed in Chapter 8.

6.5 MISSING TRANSVERSE ENERGY

Among stable SM particles, only the neutrino cannot be directly measured in the ATLAS detector. Because the neutrino carries neither electric nor color charge, it is very unlikely to interact with the tracking detectors or the calorimeters, and instead passes through the detector completely unobserved. Some particles which have been conjectured to exist, like the LSP in many SUSY models, would also have the same behavior. Therefore, it is important for ATLAS to provide some way to assess the momentum carried away by a neutral, colorless particle. This can be accomplished through a measurement of missing energy in the

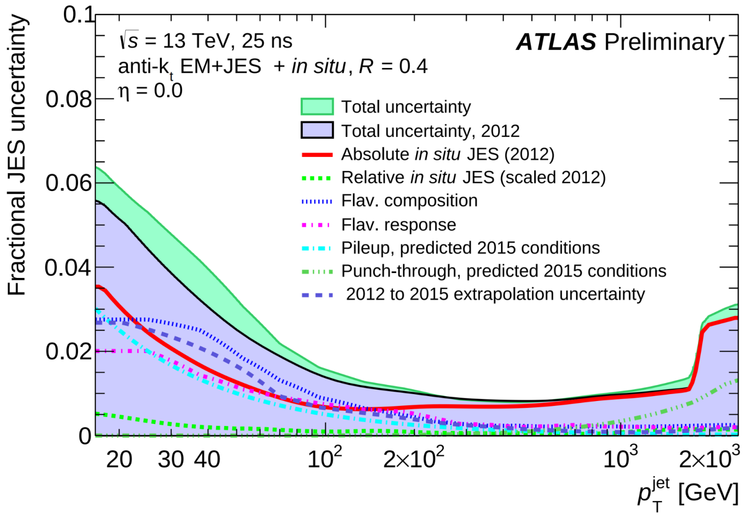

Figure 45: The total, fractional JES uncertainties estimated for 2015 data as a function of jet p_T.

transverse direction, or E_T^{miss}, which quantifies the momentum imbalance of the observed particles. From the conservation of momentum and the lack of the initial momentum in the transverse plane in the proton-proton collisions, any imbalance of momentum can be inferred to be carried away by an unmeasured particle.

E_T^{miss} is more precisely defined as the magnitude of the vector sum of the (p_x, p_y) components of each observed object's momentum. The definition is simple, but there can be significant complexity in defining the inputs. As of Run 2, ATLAS uses a common algorithmic approach to carefully calculate missing energy, but each analysis is free to define it's own inputs. For the analysis discussed throughout this thesis, the missing energy inputs consist of the electrons, photons, muons, and jets discussed in the previous sections, in addition to a track-based soft term.

To produce the most precise measurement of E_T^{miss}, it is important to use the best representation of the momentum of each of the input objects, which can often be reconstructed as multiple different types in a single event. For example, an electron can be reconstructed separately as an electron (Section 6.2) and a jet (Section 6.4), but the electron representation has the highest precision for reconstructing the true electron momentum. To ensure no duplications in the E_T^{miss} definition, the inputs are collectively considered for overlap removal. Only the most precise object type is kept for objects that fall within a cone of $\Delta R < 0.2$ for pairs of electrons and jets and a cone of $\Delta R < 0.4$ for other pair types.

The fully reconstructed objects do not include all of the energy within the events, as some clusters do not enter into a jet and some tracks are not classified as electrons or muons. These momentum carried by these objects is accounted for in a soft-term, which tallies all of the energy carried by the particles too soft to form separate objects. The track soft term uses only tracking information to estimate the contribution of soft objects, and does so by vectorially summing the momentum of all well-reconstructed tracks with momentum above 400 MeV.

All of these contributions together give a single E_T^{miss} value for a given event. The direction of that missing energy is taken as opposite the vector sum of all the constituents, to correspond to the momentum an invisible particle would have to have to make the event balanced. Depending on the context, this missing energy can be considered the energy of a neutrino or an LSP, with a large missing energy being a common signal criteria for searches for new physics.

PART III

CALORIMETER RESPONSE

You can put some informational part preamble text here.

7 RESPONSE MEASUREMENT WITH SINGLE HADRONS

As discussed in Section 6.4, colored particles produced in collisions hadronize into jets of multiple hadrons. One approach to understanding jet energy measurements in the ATLAS calorimeters is to evaluate the calorimeter response to those individual hadrons; measurements of individual hadrons can be used to build up an understanding of the jets that they form. The redundancy of the momentum provided by the tracking system and the energy provided by the calorimeter provides an opportunity to study calorimeter response using real collisions, as described further in Section 7.2.

Calorimeter response includes a number of physical effects that can be extracted to provide insight into many aspects of jet modeling. First, many charged hadrons interact with the material of the detector prior to reaching the calorimeters and thus do not deposit any energy. Comparing this effect in data and simulation is a powerful tool in validating the interactions of particles with the material of the detector and the model of the detector geometry in simulation, see Section 7.2.2. The particles which do reach the calorimeter deposit their energy into several adjacent cells, which are then clustered together. The energy of the cluster is then the total energy deposited by that particle. Comparing the response of hadrons in data to that of simulated hadrons provides a direct evaluation of the showering of hadronic particles and the energy deposited by particles in matter (Section 7.2.4).

The above studies all use an inclusive selection of charged particles, which are comprised predominantly of pions, kaons, and (anti)protons. It is also possible to measure the response to various identified particle types separately to evaluate the simulated interactions of each particle, particularly at low energies where differences between species are very relevant. Pions and (anti)protons can be identified through decays of long-lived particles, in particular Λ, $\overline{\Lambda}$, and K_S^0, and then used to measure response as described above. This is discussed in detail in Section 7.3.

The results in this chapter use data collected at 7 and 8 TeV collected in 2010 and 2012, respectively. Both are included as the calorimeter was repaired and recalibrated between those two data-taking periods. Both sets of data are compared to an updated simulation that includes new physics models provided by `Geant4` [32] and improvements in the detector description [33, 34]. The present results are published in European Physical Journal C (EPJC) [35] and can be compared to a similar measurement performed in 2009 and 2010 [36], which used the previous version of the simulation framework [37].

7.1 DATASET AND SIMULATION

7.1.1 DATA SAMPLES

The two datasets used in this chapter are taken from dedicated low-pileup runs where the fraction of events with multiple interactions was negligible. These datasets are used rather than those containing full-pileup events to facilitate measurement of isolated hadrons. The 2012 dataset at $\sqrt{s}$ = 8 TeV contains 8 million events and corresponds to an integrated luminosity of 0.1 nb^{-1}. The 2010 dataset at $\sqrt{s}$ = 7 TeV contains 3 million events and corresponds to an integrated luminosity of 3.2 nb^{-1}. The latter dataset was also used for the 2010 results [36], but it has since been reanalyzed with an updated reconstruction including the final, best understanding of the detector description for the material and alignment from Run 1.

7.1.2 SIMULATED SAMPLES

The two datasets above are compared to simulated single-, double-, and non-diffractive events generated with `Pythia8` [38] using the A2 configuration of hadronization [39] and the MSTW 2008 parton-distribution function set [40, 41]. The admixture of the single-, double-, and non-diffractive events uses the default relative contributions from `Pythia8`. The conditions and energies for the two simulations are chosen so that they match those of the corresponding dataset.

To evaluate the interaction of hadrons with detector material, the simulation uses two different collections of hadronic physics models, called physics lists, in `Geant4 9.4` [42]. The first, `QGSP_BERT`, combines the Bertini intra-nuclear cascade [43–45] below 9.9 GeV, a parametrized proton inelastic model from 9.5 to 25 GeV [46], and a quark-gluon string model above 12 GeV [47–51]. The second, `FTFP_BERT`, combines the Bertini intra-nuclear cascade [43–45] below 5 GeV and the Fritiof model [52–55] above 4 GeV. In either list, `Geant4` enforces a smooth transition between models where multiple models overlap.

7.1.3 EVENT SELECTION

The event selection for this study is minimal, as the only requirement is selecting good-quality events with an isolated track. Such events are triggered by requiring at least two hits in the minimum-bias trigger scintillators. After trigger, each event is required to have exactly one reconstructed vertex, and that vertex is required to have four or more associated tracks.

The particles which are selected for the response measurements are first identified as tracks in the inner detector. The tracks are required to have at least 500 MeV of transverse momentum. To ensure a reliable momentum measurement, these tracks are required to have at least one hit in the pixel detector, six hits in the SCT, and small longitudinal and transverse impact parameters with respect to the primary vertex [36]. For the majority of the measurements in this chapter, the track is additionally required to have 20 hits in the TRT, which significantly reduces the contribution from tracks which undergo nuclear interactions. This requirement and its effect is discussed in more detail in Section 7.2.5. In addition, tracks are rejected if there is any other reconstructed track which extrapolates to the calorimeter within a cone of $\Delta R = \sqrt{(\Delta\phi)^2 + (\Delta\eta)^2} < 0.4$. This requirement guarantees that the contamination of energy from nearby charged particles is negligible [36].

7.2 INCLUSIVE HADRON RESPONSE

The calorimeter response is more precisely defined as the ratio of the measured calorimeter energy to the true energy carried by the particle, although this true energy is unknown. For charged particles, however, the inner detector provides a very precise measurement of momentum (with uncertainty less than 1%) that can be used as a proxy for true energy. The ratio of the energy deposited by the charged particle in the calorimeter, E, to its momentum measured in the inner detector p, forms the calorimeter response measure called E/p. Though the distribution of E/p contains a number of physical features, this study focuses on the trends in two aggregated quantities: $\langle E/p \rangle$, the average of E/p for the selected tracks, and the zero fraction, the fraction of tracks with no associated energy in the calorimeter for those tracks.

The calorimeter energy assigned to a track is defined using clusters. The clusters are formed using a 4–2–0 algorithm [56] that begins with seeds requiring at least 4 times the average calorimeter cell noise. The neighboring cells with at least twice that noise threshold are then added to the cluster, and all bounding cells are then added with no requirement. This algorithm minimizes noise contributions through its seeding process, and including the bounding cells improves the energy resolution [57]. The clusters are associated to a given track if they fall within a cone of $\Delta R = 0.2$ of the extrapolated position of the track, which includes about 90% of the energy on average [36].

7.2.1 E/P DISTRIBUTION

The E/p distributions measured in both data and simulation are shown in Figure 46 for two example bins of track momentum and for tracks in the central region of the detector. These distributions show several important features of the E/p observable. The large content in the bin at $E = 0$ comes from tracks that have no associated cluster, which occurs due to interactions with detector material prior to reaching the calorimeter or the energy deposit being insufficiently large to generate a seed, and are discussed in Section 7.2.2. The small negative tail also comes from tracks that do not deposit any energy in the calorimeter but are randomly associated to a cluster with an energy below the noise threshold. The long positive tail above 1.0 comes from the contribution of neutral particles. Nearby neutral particles deposit (sometimes large) additional energy in the calorimeter but do not produce tracks in the inner detector, so they cannot be rejected by the track isolation requirement. Additionally the peak and mean of the distribution falls below 1.0 because of the loss of energy not found within the cone as well as the non-compensation of the calorimeter.

The data and simulation share the same features, but the high and low tails are significantly different. The simulated events tend to overestimate the contribution of neutral particles to the long tail, an effect which can be isolated and removed as discussed in Section 7.2.3. Additionally, the simulated clusters have less noise on average, although this is a small effect on the overall response.

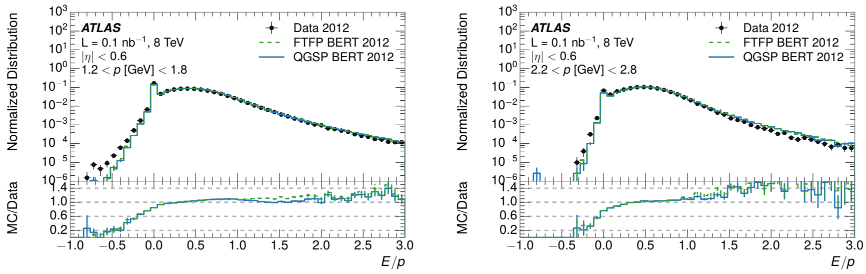

(a) (b)

Figure 46: The E/p distribution and ratio of simulation to data for isolated tracks with (a) $|\eta| < 0.6$ and $1.2 < p/\text{GeV} < 1.8$ and (b) $|\eta| < 0.6$ and $2.2 < p/\text{GeV} < 2.8$.

7.2.2 ZERO FRACTION

The fraction of particles with no associated clusters, or similarly those with $E \leq 0$, reflects the modeling of both the detector geometry and hadronic interactions. The zero fraction is expected to rise as the amount of material a particle traverses increases, while it is expected to decrease as the particle energy increases. This dependence can be seen in Figure 47, where the zero fraction in data and simulation is shown as a function of momentum and the amount of material measured in interaction lengths. The trends are similar between 2010 and 2012 and for positively and negatively charged particles. The zero fraction decreases with energy as expected. The absolute discrepancy in zero fraction between data and simulation decreases with momentum from 5% to less than 1%, but this becomes more pronounced in the ratio as the zero fraction shrinks quickly with increasing momentum. The amount of material in the detector increases with η, which is used to obtain results for interaction lengths ranging between 0.1 and 0.65 λ. As the data and simulation have significant disagreement in the zero fraction over a number of interaction lengths, the difference must be primarily from the modeling of hadronic interactions with detector material and not just the detector geometry. Although two different hadronic interaction models are shown in the figure, they have very similar discrepancies to data because both use the same description (the BERT model) at low momentum.

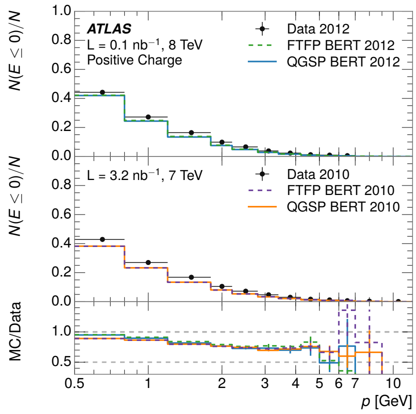

(a)

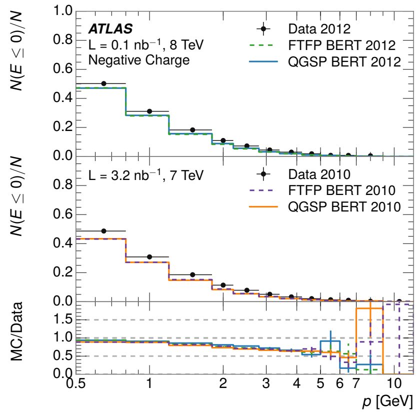

(b)

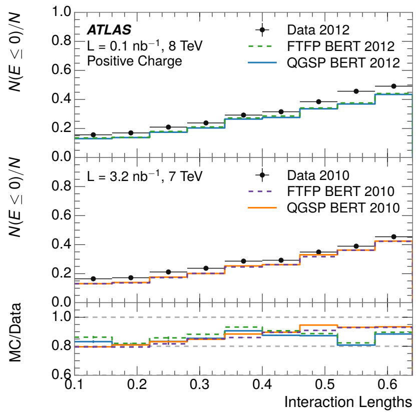

(c)

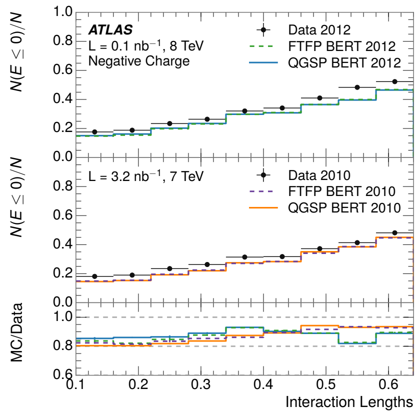

(d)

Figure 47: The fraction of tracks as a function (a, b) of momentum, (c, d) of interaction lengths with $E \leq 0$ for tracks with positive (on the left) and negative (on the right) charge.

7.2.3 NEUTRAL BACKGROUND SUBTRACTION

The isolation requirement on hadrons is only effective in removing an energy contribution from nearby charged particles. Nearby neutral particles, predominantly photons from π^0 decays, also add their energy to the calorimeter clusters, but mostly in the electromagnetic calorimeter. The arrangement of energy deposits is shown in Figure 48, which illustrates both energy deposits from the hadronic particle and additional deposits from neutral particles. It is possible to measure this contribution, on average, using late-showering hadrons that minimally ionize in the electromagnetic calorimeter. Such particles are selected by requiring that they deposit less than 1.1 GeV in the EM calorimeter within a cone of $\Delta R < 0.1$ around the track. To ensure that these particles are well measured, they are additionally required to deposit between 40% and 90% of their energy in the hadronic calorimeter within the same cone.

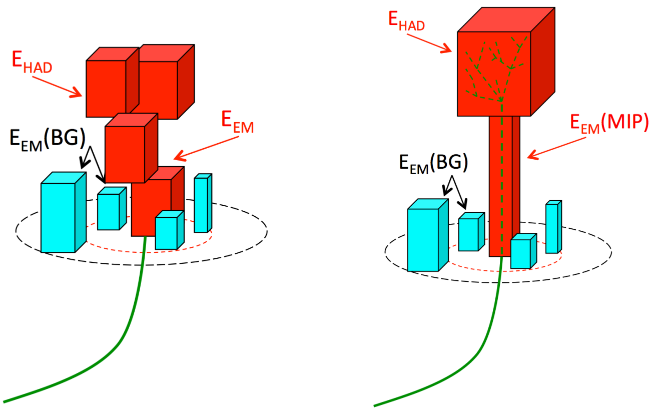

(a) (b)

Figure 48: An illustration (a) of the geometry of energy deposits in the calorimeter. The red energy deposits come from the charged particle targeted for measurement, while the blue energy deposits are from nearby neutral particles and must be subtracted. The same diagram (b) for the neutral-background selection, described in Section 7.2.3.

These particles provide a clean sample to measure the nearby neutral background because they do not deposit energy in the area immediately surrounding them in the EM calorimeter, as shown in Figure 48. So, the energy deposits in the region $0.1 < \Delta R < 0.2$ can be attributed to neutral particles alone. To estimate the contribution to the whole cone considered for the response measurement, that energy is scaled by a geometric factor of 4/3. This quantity, $\langle E/p \rangle_{\mathrm{BG}}$, measured in aggregate over a number of particles, gives the contribution to $\langle E/p \rangle$ from neutral particles in the EM calorimeter. Similar techniques were used in the individual layers of the hadronic calorimeters to show that the background from neutrals is negligible in those layers [36].

The distribution of this background estimate is shown in Figure 49 for data and simulation with the two different physics lists. The contribution from neutral particles falls from 0.1 at low momentum to around 0.03 for particles above 7 GeV. Although the simulation captures the overall trend, it significantly overestimates the neutral contribution for tracks with momentum between 2 and 8 GeV. This effect was also seen in the tails of the E/p distributions in Figure 46. This difference is likely due to modeling of coherent neutral particle radiation in `Pythia8` that overestimates the production of π^0 near the production of the charged particles. The discrepancy does not depend on η and thus is unlikely to be a mismodeling of the detector. This difference can be subtracted to form a corrected average of E/p.

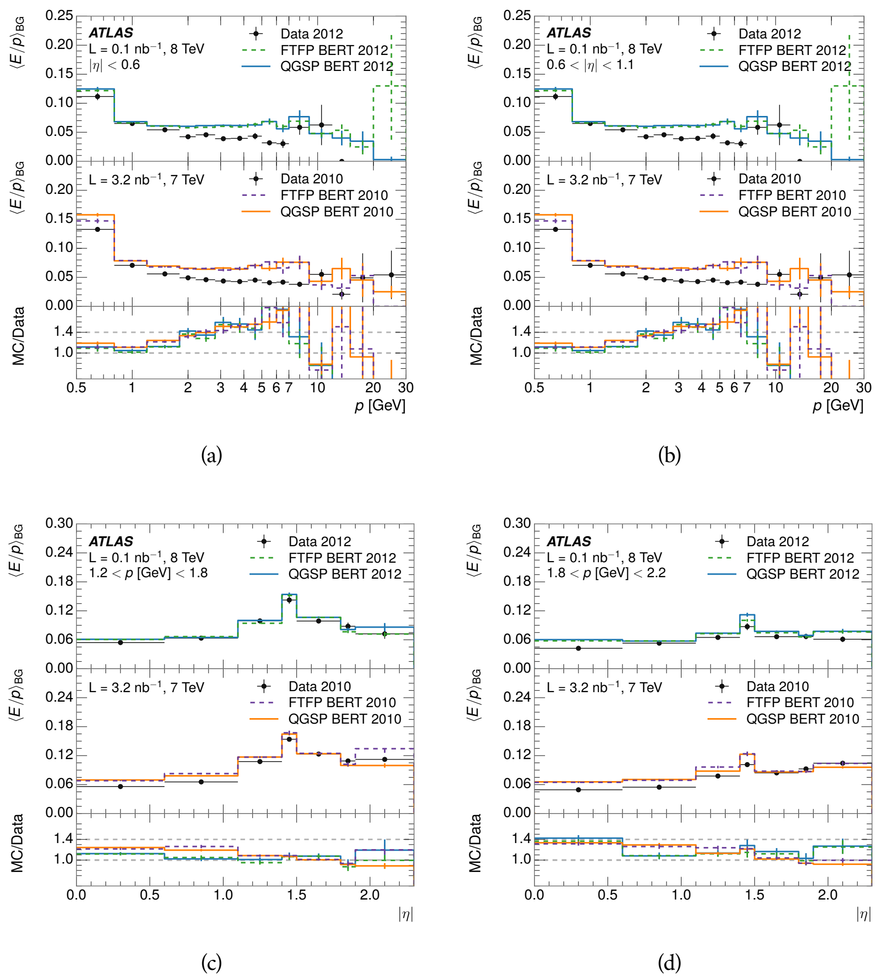

Figure 49: $\langle E/p \rangle_{BG}$ as a function of the track momentum for tracks with (a) $|\eta| < 0.6$, (b) $0.6 < |\eta| < 1.1$, and as a function of the track pseudorapidity for tracks with (c) $1.2 < p/\text{GeV} < 1.8$, (d) $1.8 < p/\text{GeV} < 2.2$.

7.2.4 CORRECTED RESPONSE

Figure 50 shows $\langle E/p \rangle_{COR}$ as a function of momentum for several bins of pseudorapidity. This corrected $\langle E/p \rangle_{COR} \equiv \langle E/p \rangle - \langle E/p \rangle_{BG}$ measures the average calorimeter response without the contamination of neutral particles. It is the most direct measurement of calorimeter response in that it is the energy measured for fully isolated hadrons. The correction is performed separately in data and simulation, so that the mismodeling of the neutral background in simulation is removed from the comparison of response. The simulation overestimates the response at low momentum by about 5%, an effect that can be mostly attributed to the underestimation of the zero fraction mentioned previously. For $|\eta| < 0.6$, the data-simulation agreement has a larger discrepancy by about 5% for 2010 than 2012, although this is not reproduced in at higher pseudorapidity.

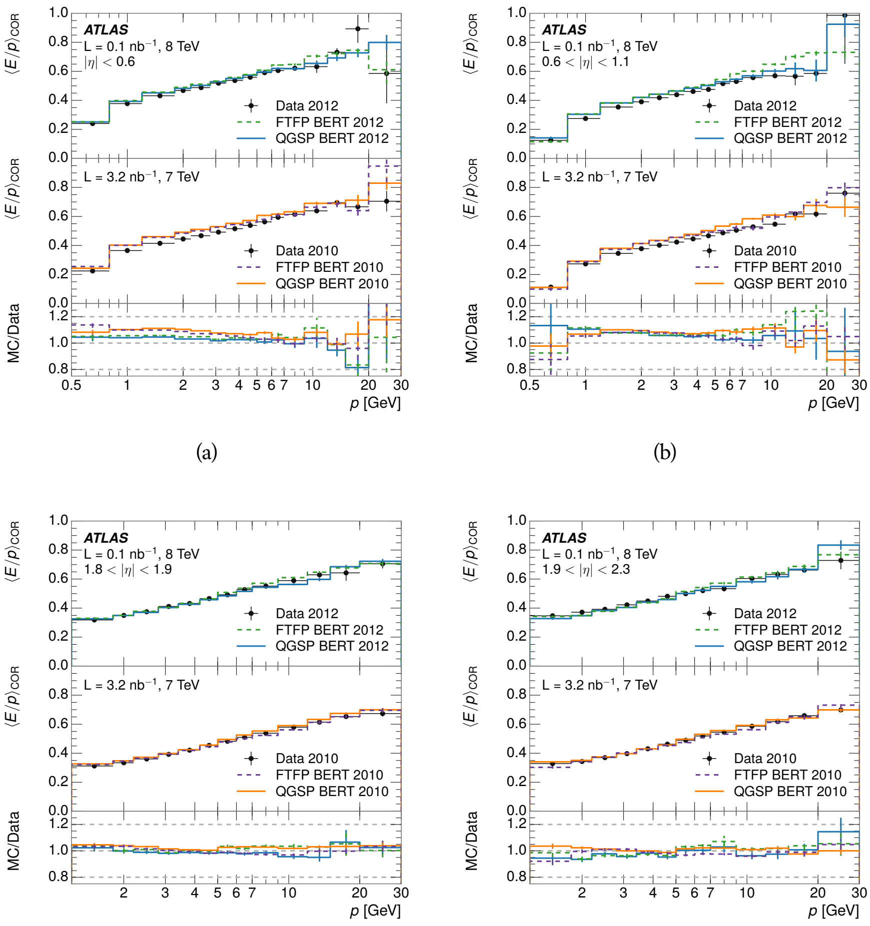

(a) (b) (c) (d)

Figure 50: $\langle E/p \rangle_{\mathrm{COR}}$ as a function of track momentum, for tracks with (a) $|\eta| < 0.6$, (b) $0.6 < |\eta| < 1.1$, (c) $1.8 < |\eta| < 1.9$, and (d) $1.9 < |\eta| < 2.3$.

The response measurement above used topological clustering at the EM scale, that is clusters were formed to measure energy but no corrections were applied to correct for expected effects like energy lost outside of the cluster or in uninstrumented material. It is also interesting to measure $\langle E/p \rangle_{\mathrm{COR}}$ using LCW energies, which accounts for those effects by calibrating the energy based on the properties of the cluster such as energy density and depth in the calorimeter. Figure 51 shows these distributions for tracks with zero or more clusters and separately for tracks with one or more clusters. The calibration moves the mean value of $\langle E/p \rangle_{\mathrm{COR}}$ significantly closer to 1.0 as desired, but the discrepancy between data and simulation remains in the comparison that includes tracks with zero associated clusters. The agreement between data and simulation improves noticeably when at least one cluster is required, as this removes the contribution from the mismodeling of the zero fraction.

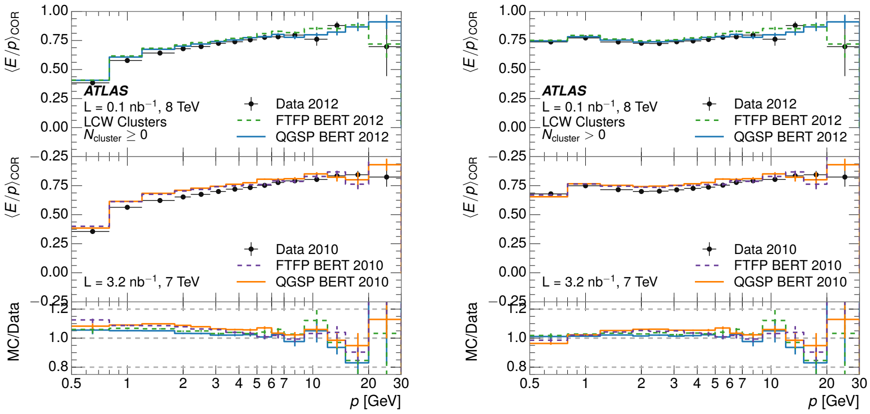

(a) (b)

Figure 51: $\langle E/p \rangle_{\mathrm{COR}}$ calculated using LCW-calibrated topological clusters as a function of track momentum for tracks with (a) zero or more associated topological clusters or (b) one or more associated topological clusters.

7.2.5 ADDITIONAL STUDIES

As has been seen in several measurements in previous sections, the simulation does not correctly model the chance of a low momentum hadron to reach the calorimeter. Because of the consistent discrepancy across pseudorapidity and interaction lengths, this can be best explained by incomplete understanding of hadronic interactions with the detector [35]. For example, a hadron that scatters off of a nucleus in the inner detector can be deflected through a significant angle and not reach the expected location in the calorimeter. In addition, these interactions can produce secondary particles that are difficult to model.

The requirement used throughout the previous sections on the number of hits in the TRT reduces these effects by preferentially selecting tracks that do not undergo nuclear interactions. It is interesting to check how well the simulation models tracks with low numbers of TRT hits, which selects tracks that are more likely to have undergone a hadronic interaction. Figure 52 compares the distributions with $N_{\mathrm{TRT}} < 20$ to $N_{\mathrm{TRT}} > 20$ for real and simulated particles[1]. As expected, the tracks with fewer hits are poorly modeled in the simulation as $\langle E/p \rangle_{\mathrm{COR}}$ differs by as much as 25% at low momentum. They also have significantly lower $\langle E/p \rangle_{\mathrm{COR}}$ on average, because they are much less likely to have an associated cluster.

1 The distribution with $N_{\mathrm{TRT}} > 20$ is the same as shown in Figure 50 (a) and is included again here for the comparison.

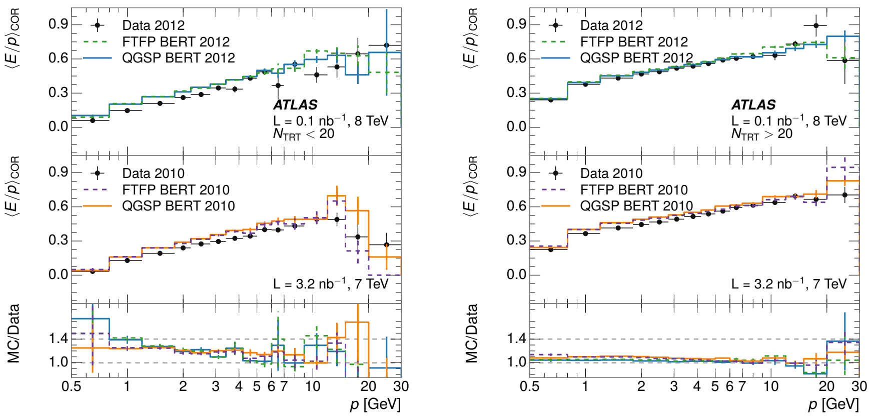

(a) (b)

Figure 52: Comparison of the $\langle E/p \rangle_{\mathrm{COR}}$ for tracks with (a) less than and (b) greater than 20 hits in the TRT.

Another interesting aspect of the simulation is the description of antiprotons at low momentum, where `QGSP_BERT` and `FTFP_BERT` have significant differences. This can be seen to have an effect in the inclusive response measurement when separated into positive and negative charge. The $\langle E/p \rangle_{\mathrm{COR}}$ distributions for positive and negative particles are shown in Figure 53, where a small difference between `QGSP_BERT` and `FTFP_BERT` can be seen in the distribution for negative tracks. The figure also includes data, and the simulation overestimates $\langle E/p \rangle_{\mathrm{COR}}$ mostly due to an underestimation in zero fraction. There is an approximately 5% difference between the 2010 and 2012 simulated events. The difference between positive and negative particles is demonstrated more clearly in Figure 54, which shows the E/p distribution in the two simulations separated by charge. There is a small difference around $E/p > 1.0$, which can be explained by the additional energy deposited by the annihilation of the antiproton in the calorimeter that is modeled well only in `FTFP_BERT`. This is also explored with data using identified antiprotons in Section 7.3.

The $\langle E/p \rangle$ results in previous sections have considered the electromagnetic and hadronic calorimeters together as a single energy measurement, to emphasize the total energy deposited for a given particle. However, the deposits in each calorimeter are measured separately and $\langle E/p \rangle$ can be constructed for each layer separately. As the layers are composed of different materials and are modeled separately in the detector geometry, confirmation that the simulation matches the data well in each layer adds confidence in both the description of hadronic interactions with the two different materials and also the geometric description of each.

The technique discussed in Section 7.2.3 for selecting MIPs in the electromagnetic calorimeter is also useful in studying deposits in the hadronic calorimeter. The tracks selected with the MIP requirements deposit almost all of their energy exclusively in the hadronic calorimeter. Figure 55 shows $\langle E/p \rangle^{\mathrm{Had}}_{\mathrm{RAW}}$, where RAW indicates that no correction has been applied for neutral backgrounds and

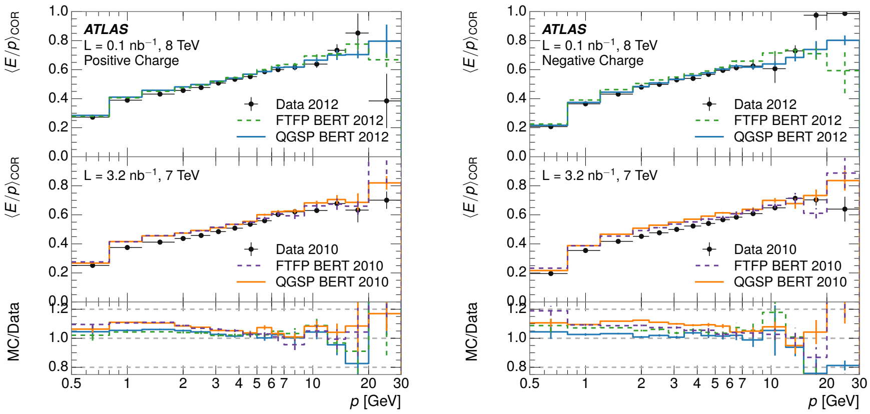

(a) (b)

Figure 53: Comparison of the $\langle E/p \rangle_{\mathrm{COR}}$ for (a) positive and (b) negative tracks as a function of track momentum for tracks with $|\eta| < 0.6$.

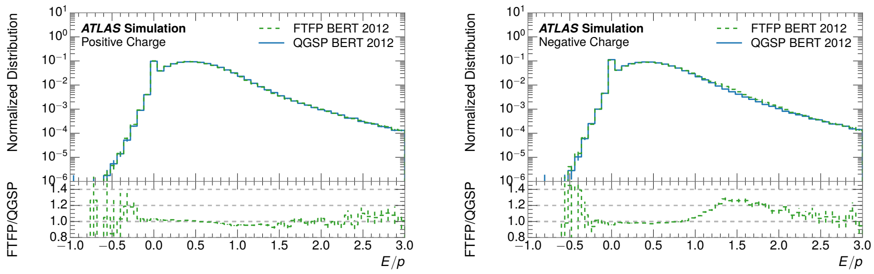

(a) (b)

Figure 54: Comparison of the E/p distributions for (a) positive and (b) negative tracks with $0.8 < p/\mathrm{GeV} < 1.2$ and $|\eta| < 0.6$, in simulation with the `FTFP_BERT` and `QGSP_BERT` physics lists.

Had indicates that only clusters for the hadronic calorimeter are included[2]. The distributions are shown both for the original EM scale calibration and after LCW calibration. The data and simulation agree very well in this comparison, except in the lowest momentum bin where there is a 5% discrepancy that has already been seen in the measurements in Section 7.2.4.

A similar comparison can be made in the electromagnetic calorimeter by selecting particles which have no associated energy in the hadronic calorimeter. These results are measured in terms of $\langle E/p \rangle^{\mathrm{EM}}_{\mathrm{COR}}$, where EM designates that only clusters in the electromagnetic calorimeter are included and COR designates that the neutral background is subtracted as the neutral background is present in this case. Figure 56 shows the analogous comparisons to Figure 55 in the electromagnetic calorimeter. The $\langle E/p \rangle_{\mathrm{COR}}$ values are lower on average in the EM calorimeter than in the hadronic calorimeter, which is an expected conse-

2 The RAW and COR versions of $\langle E/p \rangle$ in this case are the same, as the neutral background is negligible in that calorimeter layer.

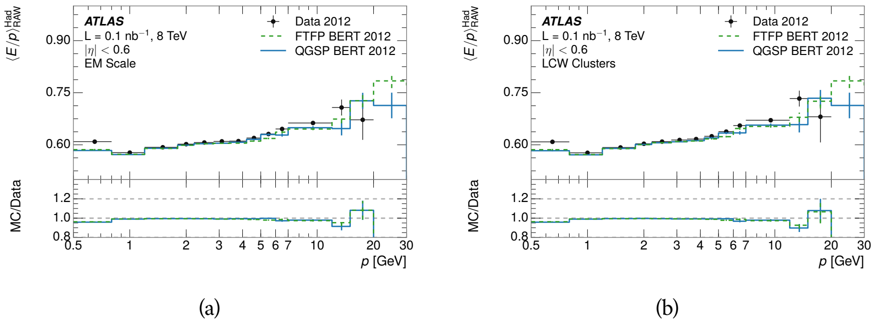

Figure 55: Comparison of the response of the hadronic calorimeter as a function of track momentum (a) at the EM-scale and (b) after the LCW calibration.

quence of their different material types (discussed in Section 5.4). In this case the disagreement between data and simulation is more pronounced, with discrepancies as high as 5% over a larger range of momenta. This level of discrepancy indicates that the description of the electromagnetic calorimeter is actually the dominant source of discrepancy in the combined distributions in Section 7.2.4.

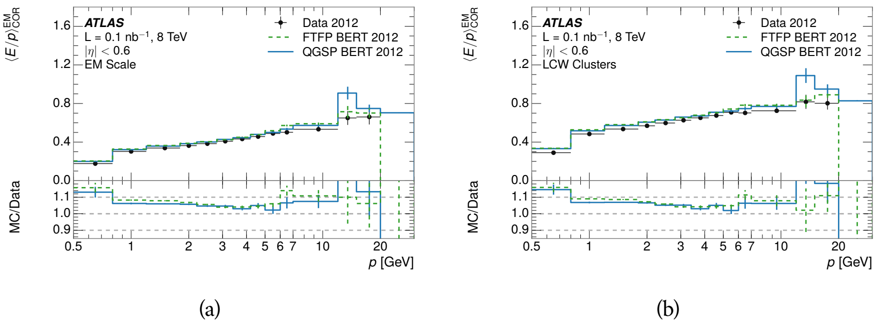

Figure 56: Comparison of the response of the EM calorimeter as a function of track momentum (a) at the EM-scale and (b) with the LCW calibration.

7.3 IDENTIFIED PARTICLE RESPONSE

The inclusive response measurement for hadrons can be augmented by measuring the response for specific particle species. The simulation models each particle type separately, and understanding the properties of each is important in constraining the uncertainty on jets. In order to select and measure specific hadrons, this section relies on the displaced decays of long-lived particles. Such decays can be identified by reconstructing secondary vertices with a requirement on mass. In particular, Λ, $\bar{\Lambda}$, and K_S^0 can be used to select a pure sample of protons, antiprotons, and pions, respectively.

7.3.1 DECAY RECONSTRUCTION

The measurement of the response for identified particles uses the same selection as for inclusive particles (Section 7.1.3) with a few additions. Each event used is required to have at least one secondary vertex, as described in Section 6.1.3, and the tracks are required to match to that vertex rather than the primary vertex. Pions are selected from decays of $K^0_S \to \pi^+\pi^-$, which is the dominant decay for K^0_S to charged particles. Protons are selected from decays of $\Lambda \to \pi^- p$ and antiprotons from $\bar{\Lambda} \to \pi^+ \bar{p}$, which are similarly the dominant decays of Λ and $\bar{\Lambda}$ to charged particles. The species of parent hadron in these decays is determined by reconstructing the mass of the tracks associated to the secondary vertex. The sign of the higher momentum decay particle can distinguish between Λ and $\bar{\Lambda}$, which of course have the same mass, as the proton or antiproton is kinematically favored to have higher momentum. The proton or antiproton will carry the higher momentum above 95% of the time. Examples of the reconstructed masses used to select these decays are shown in Figure 57. The mass peaks in data and both simulation models are very similar.

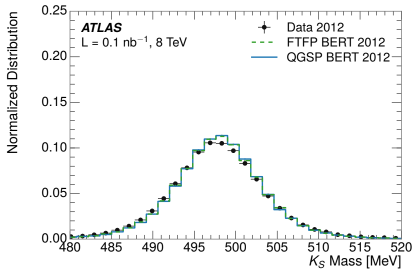

(a)

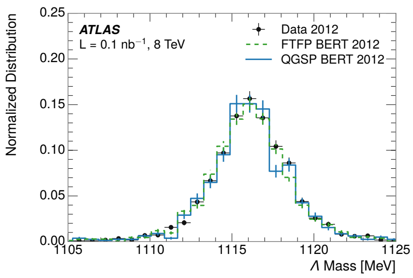

(b)

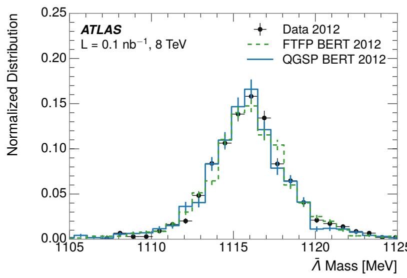

(c)

Figure 57: The reconstructed mass peaks of (a) K^0_S, (b) Λ, and (c) $\bar{\Lambda}$ candidates.

The dominant backgrounds for the identified particle decays are nuclear interactions and combinatoric sources. These are suppressed by the kinematic requirements on the tracks as well as an additional veto which removes candidates that are consistent with both a Λ or $\bar{\Lambda}$ and a K^0_S hypothesis, which is possible because of the different assumptions on particle mass in each case [36]. After these requirements, the backgrounds are found to be negligible compared to the statistical errors on these measurements.

7.3.2 IDENTIFIED RESPONSE

With these techniques the E/p distributions are extracted in data and simulation for each particle species and shown in Figure 58. These distributions are shown for a particular bin of E_a ($2.2 < E_a/\text{GeV} < 2.8$), rather than p. E_a is the energy available to be deposited in the calorimeter: for pions $E_a = \sqrt{p^2 + m_\pi^2}$, for protons $E_a = \sqrt{p^2 + m_p^2} - m_p$, and for antiprotons $E_a = \sqrt{p^2 + m_p^2} + m_p$. In the pion case, the entire energy of the pion is deposited in the calorimeter, so E_a is just the usual energy. For protons, the proton remains after depositing its energy in the calorimeter, so its mass is not available and must be subtracted from E_a. And for antiprotons, the antiproton constituents annihilate with the quarks in the protons and neutrons of the calorimeter material, so it deposits its entire energy as well as an the additional energy from the annihilation; this extra energy is equal to the mass of the antiproton and is added to the available energy. The features of the E/p distributions are similar to the inclusive case, with a peak around 0.5 at low momentum. The zero fraction is not as pronounced as in the inclusive case. There is a small negative tail from noise and a large fraction of tracks with zero energy from particles which do not reach the calorimeter. The long positive tail is noticeably more pronounced for antiprotons because of the additional energy generated by the annihilation of the antiproton with the material of the detector, and the peak of the distribution is also increased for the same reason. The simulation correctly captures these features, and the agreement between data and simulation is good to within the available statistical limitations.

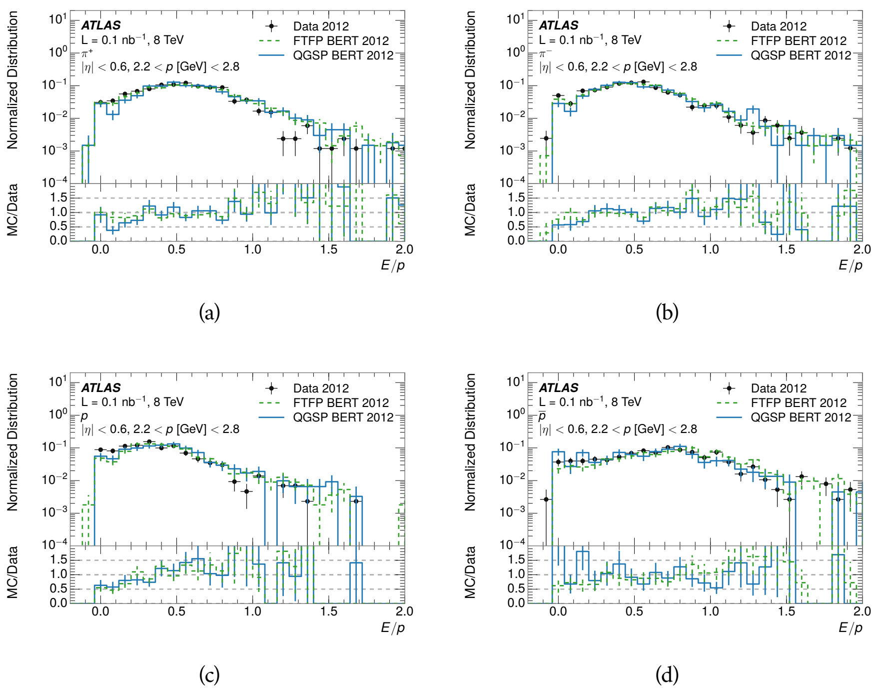

Figure 58: The E/p distribution for isolated (a) π^+, (b) π^-, (c) proton, and (d) anti-proton tracks.

The zero fraction is further explored in Figure 59 for pions and protons in data and simulation. The simulation consistently underestimates the zero fraction independent of particle species, which implies that this discrepancy is not caused by the model of a particular species but rather a feature common to all. The zero fraction is larger for π^- than π^+, which is evident in both data and simulation. However there is some suggestion that this increase in zero fraction leads to an even larger discrepancy in the modeling of π^- in simulation.

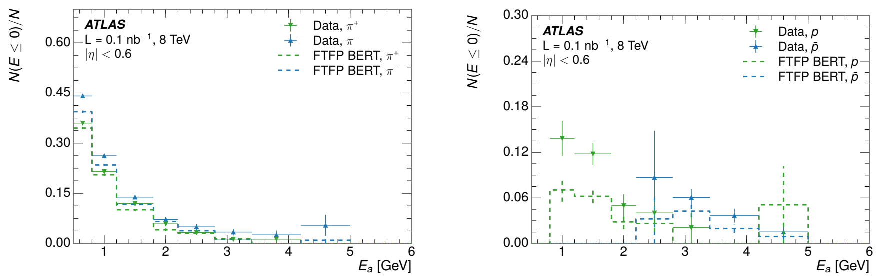

(a) (b)

Figure 59: The fraction of tracks with $E \leq 0$ for identified (a) π^+ and π^-, and (b) proton and anti-proton tracks

It is also interesting to compare the response between the different particle species. One approach to do this is to measure the difference in $\langle E/p \rangle$ between two types, which has the advantage of removing the neutral background. These differences are shown in various combinations in Figure 60. The response for π^+ is greater on average than the response to π^- because of a charge-exchange effect which causes the production of additional neutral pions in the showers of π^+ [58]. This effect becomes less significant as the $\langle E/p \rangle$ increases, and the difference approaches zero. Both version of the simulation correctly model this trend. The response for π^+ is also greater on average than the response to p, because a large fraction of the energy of π^+ hadrons is converted to an electromagnetic shower [59, 60]. This effect is again reproduced by both simulations. The $\bar{p}$ response, however, is significantly higher than the response to π^- because of the annihilation of the antiproton, but the difference decreases at higher energies where the additional energy has less relative importance. `FTFP_BERT` models this effect more accurately than `QGSP_BERT` because of their different descriptions of $\bar{p}$ interactions with material.

It is also possible to remove the neutral background from these response distributions using the same technique as in Section 7.2.3. The technique is largely independent of the particle species and so can be directly applied to $\langle E/p \rangle$ for pions. The $\langle E/p \rangle_{\mathrm{COR}}$ distributions for pions are shown in Figure 61, which are very similar to the inclusive results. The inclusive hadrons are comprised mostly of pions, so this similarity is not surprising. It is also possible to see the small differences between π^+ and π^- response here, where $\langle E/p \rangle_{\mathrm{COR}}$ is higher on average for π^+. The agreement between data and simulation is significantly worse for the π^- distributions than for the π^+, with a discrepancy greater than 10% below 2-3 GeV.

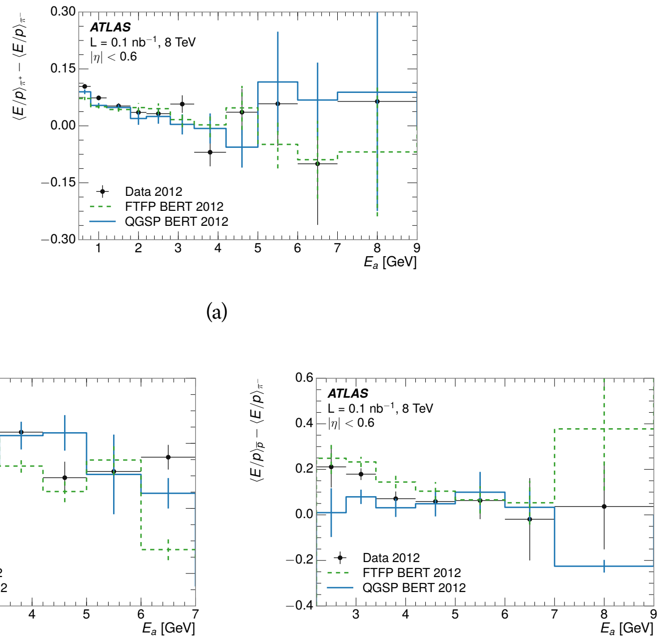

(a) (b) (c)

Figure 60: The difference in $\langle E/p\rangle$ between (a) π^+ and π^- (b) p and π^+, and (c) $\bar{p}$ and π^-.

7.3.3 ADDITIONAL SPECIES IN SIMULATION

The techniques above provide a method to measure the response separately for only pions and protons. However the hadrons which forms jets include a number of additional species such as kaons and neutrons. The charged kaons are an important component of the inclusive charged hadron distribution, which is comprised of roughly 60-70% pions, 15-20% kaons, and 5-15% protons [35]. These fractions vary depending on the production mechanism, and the ranges are indicative of the variations between different events. These are difficult to measure in data at the ATLAS detector, as the particles which decay to kaons such as ϕ and D mesons have shorter lifetimes and are comparatively rare. These properties make it impractical to identify a sufficient number of decays to make statistically meaningful measurements. The simulation of these particles includes noticeable differences in response between species at low energies, which are shown in Figure 62 for FTFP_BERT. The significant differences in response between protons and antiprotons below 1 GeV are accounted for above in the definitions of E_a.

7.4 SUMMARY

These various measurements of calorimeter response shown above for data and simulation illuminate the accuracy of the simulation of hadronic interactions at the ATLAS detector. The results were obtained using 2010 and 2012 data at 7 and 8 TeV, but reflect the most current understanding of the detector alignment

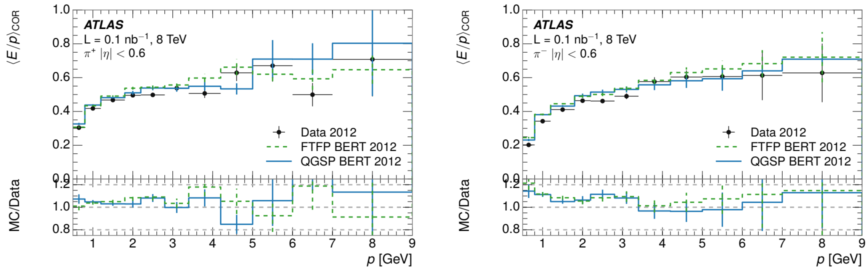

(a) (b)

Figure 61: $\langle E/p \rangle_{\text{COR}}$ as a function of track momentum for (a) π^+ tracks and (b) π^- tracks.

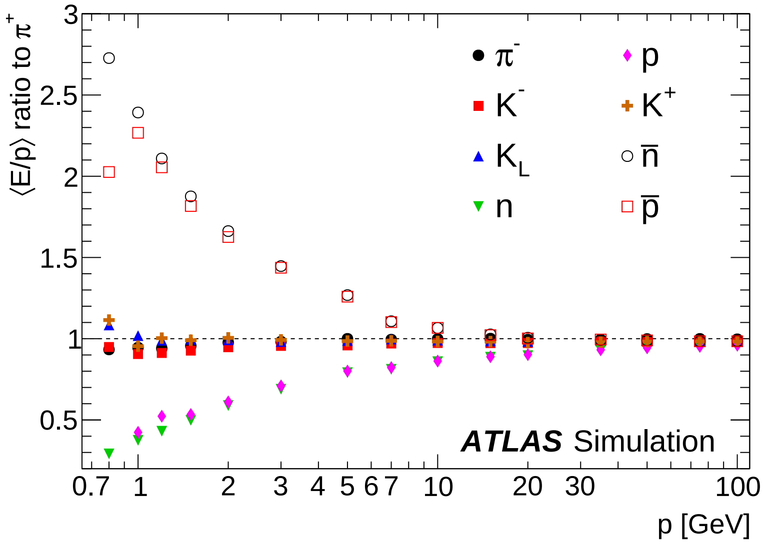

Figure 62: The ratio of the calorimeter response to single particles of various species to the calorimeter response to π^+ with the physics list FTFP_BERT.

and geometry. A number of measurements focusing on a comparison between protons and antiprotons suggest that FTFP_BERT models those interaction more accurately than QGSP_BERT. These measurements, among others, were the motivation to switch the default Geant4 simulation from QGSP_BERT to FTFP_BERT for all ATLAS samples.

Even with these updates, there are a number of approximately 5% discrepancies in response between the data and simulation. The differences result mostly from a difference in the modeling of the zero fraction, which is most significant at low energies. The difference in response without the zero fraction are primarily in the electromagnetic calorimeter, while the modeling of the hadronic calorimeter is accurate. At higher momenta the simulation of hadronic interactions is very consistent with data. Chapter 8 discusses how to use these observed differences to constrain the jet energy scale and its associated uncertainties.

8

JET ENERGY RESPONSE AND UNCERTAINTY

8.1 MOTIVATION

As jets form a major component of many physics analyses at ATLAS, it is crucial to carefully calibrate the measurement of jet energies and to derive an uncertainty on that measurement. These uncertainties are often the dominant systematic uncertainty in high-energy analyses at the LHC. Jet balance techniques, as discussed in Section 6.4.3, provide a method to constrain the JES and its uncertainty in data, and provide the default values used for ATLAS jet measurements at most energies [61]. These techniques are limited by their reliance on measuring jets in data, so they are statistically limited in estimating the jet energy scale at the highest jet energies. This chapter presents another method for estimating the jet energy scale and its uncertainty which builds up a jet from its constituents and thus can be naturally extended to high jet momentum. Throughout this chapter the jets studied are simulated using `Pythia8` with the CT10 parton distribution set [62] and the AU2 tune [39], and corrections are taken from the studies including data and simulation in Chapter 7.

As described in Section 6.4, jets are formed from topological clusters of energy in the calorimeters using the anti-k_t algorithm. These clusters originate from a diverse spectrum of particles, in terms of both species and momentum, leading to significantly varied jet properties and response between jets of similar produced momentum. Figure 63 shows the momentum and particle distributions of simulated particles within jets at a few examples energies. Each bin for each distribution shows the fraction of jet constituents of that particle type and that truth energy for a jet of the specified energy. These show that majority of particles in jets are charged pions and photons, and the charged pions constituent carry the highest energies on average. The figure also demonstrates that the majority of the particles in a jet have much lower momentum than the jet itself; for example in 90-100 GeV jets less than 1% of particles have energies above 20 GeV. The E/p measurements provide a thorough understanding of the dominant particle content of jets, the charged hadrons.

8.2 UNCERTAINTY ESTIMATE

A correct modeling of jets in the data by simulation requires that both the particle production inside jets as well as the response of the calorimeter to particles are correctly modeled. Chapter 7 showed that the simulation does not perfectly model the calorimeter response, and provided measurements that can be used to correct for discrepancies. To determine the corrections appropriate for jets, that is to evaluate a jet energy response, the simulated jet energies are compared

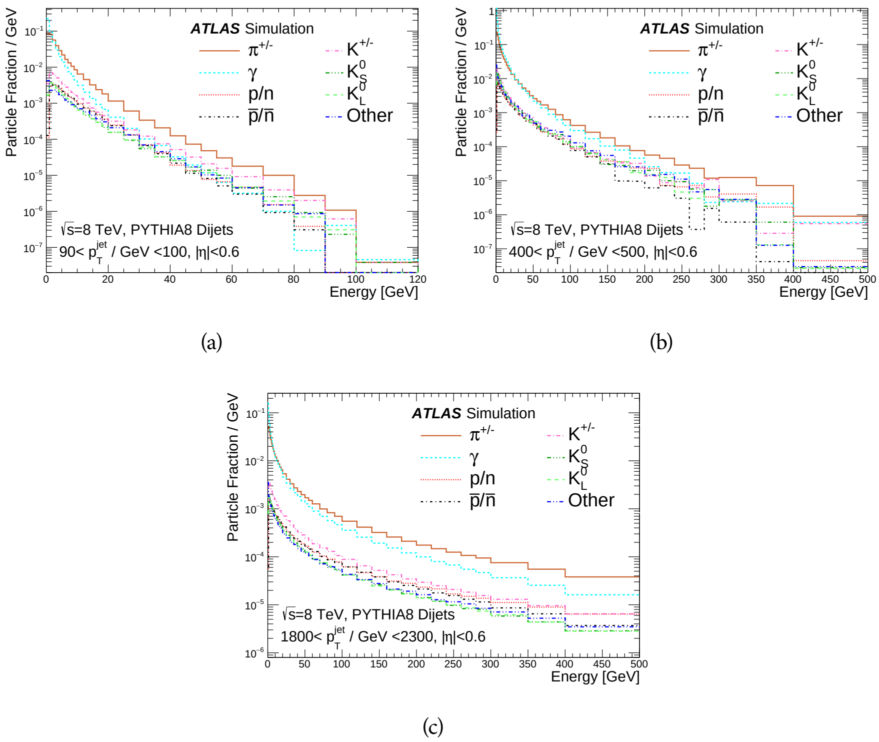

Figure 63: The spectra of true particles inside anti-k_t, $R = 0.4$ jets with (a) $90 < p_T/\text{GeV} < 100$, (b) $400 < p_T/\text{GeV} < 500$, and (c) $1800 < p_T/\text{GeV} < 2300$.

to a corrected jet built up at the particle level. Each cluster in a jet is associated to the truth particle which deposited it, and the energy in that cluster is then corrected for a number of effects based on measurements in data. The primary corrections come from the single hadron response measurements in addition to response measured using the combined test beam which covers higher momentum particles [63]. These corrections include both a shift (Δ), in order to make the simulation match the average response in data, and an uncertainty (σ) associated with the ability to constrain the difference between data and simulation. Some of the dominant sources of uncertainty are itemized in Table 8 with typical values, and the full list considered is described in detail in the associated paper [35]. These uncertainties cover differences between the data and simulation in the modeling of calorimeter response to a given particle. The typical values are listed as ranges to show the variation over momentum and pseudorapidity. For the in situ E/p term, for example, Δ corresponds to the difference between data and simulation for $\langle E/p \rangle_{\text{COR}}$ at the LCW scale (shown in Figure 51 (b)) and σ is the uncertainty on that difference including the statistical uncertainties of both the data and simulated events. No uncertainties are added for the difference between particle composition of jets in data and simulation, as this method focuses on providing a response correction for discrepancies of particle interactions rather than differences in particle composition.

From these terms, the jet energy scale and uncertainty is built up from individual energy deposits in simulation. Each uncertainty term is treated inde-

Abbrev.	Description	Δ (%)	σ (%)
In situ E/p	The comparison of $\langle E/p \rangle_{\mathrm{COR}}$, at the LCW scale, as described in Chapter 7 with statistical uncertainties from 500 MeV to 20 GeV.	0-3	1-5
CTB	The main $\langle E/p \rangle$ comparison uncertainties, binned in p and $\|\eta\|$, as derived from the combined test beam results, from 20 to 350 GeV [63].	0-3	1-5
E/p Zero Fraction	The difference in the zero-fraction between data and MC simulation from 500 MeV to 20 GeV.	5-25	1-5
E/p Threshold	The uncertainty in the EM calorimeter response from the potential mismodeling of threshold effects in topological clustering.	0	0-10
Neutral	The uncertainty in the calorimeter response to neutral hadrons based on studies of physics model variations.	0	5-10
K_{L}	An additional uncertainty in the response to neutral K_L in the calorimeter based on studies of physics model variations.	0	20
E/p Misalignment	The uncertainty in the p measurement from misalignment of the ID.	0	1
Hadrons, $p > 350$ GeV	An energy independent uncertainty for all particles above the energy range or outside the longitudinal range probed with the combined test beam.	0	10

Table 8: The dominant sources of corrections and systematic uncertainties in the JES estimation technique, including typical values for the correcting shift (Δ) and the associated uncertainty (σ).

pendently, and is taken to be gaussian distributed. The resulting scale and uncertainty is shown in Figure 64, where the mean response is measured relative to the calibrated energy reported by simulation. The mean response is slightly below one, indicating that the simulation slightly overestimates the calorimeter response on average, and this response is relatively constant as a function of the jet p_{T}. The dominant uncertainties come from the statistical uncertainties on the E/p measurements at lower energies and the additional uncertainty for out of range measurements at higher energies. Combined the resulting uncertainty ranges from between 1.5% at low momentum and pseudorapidity to as much as 4% at higher momentum and pseudorapidity. The total uncertainty from this method at intermediate jet energies is comparable to other simulation-based methods [64] and is about twice as large as in-situ methods using data [61]. This method is the only one which provides an estimation above 1.8 TeV, however, and so is still a crucial technique in analyses that search for very energetic jets.

These techniques can also be used to measure the correlation between bins of average reconstructed jet momentum across a range of p_T and $|\eta|$, where correlations are expected because of a similarity in particle composition at similar energies. Figure 65 shows these correlations, where the uncertainties on jets in neighboring bins are typically between 30% and 60% correlated. The uncertainty on all jets becomes significantly correlated at high energies and larger pseudorapidities, when the uncertainty becomes dominated by the single term reflecting out of range particles.

8.3 SUMMARY

The technique described above provides a jet energy scale and uncertainty by building up jet corrections from the energy deposits of constituent particles. The E/p measurements are crucial in providing corrections for the majority of particles in the jets. The uncertainty derived this way is between 2 and 5% and is about twice as large at corresponding momentum than jet balance methods. However this is the only uncertainty available for very energetic jets using 2012 data and simulation, and repeating this method with Run 2 data and simulation will be important in providing an uncertainty for the most energetic jets in 13 TeV collisions.

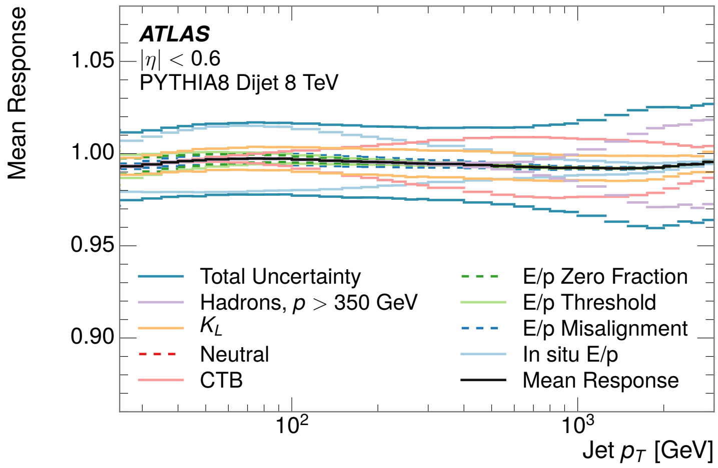

(a)

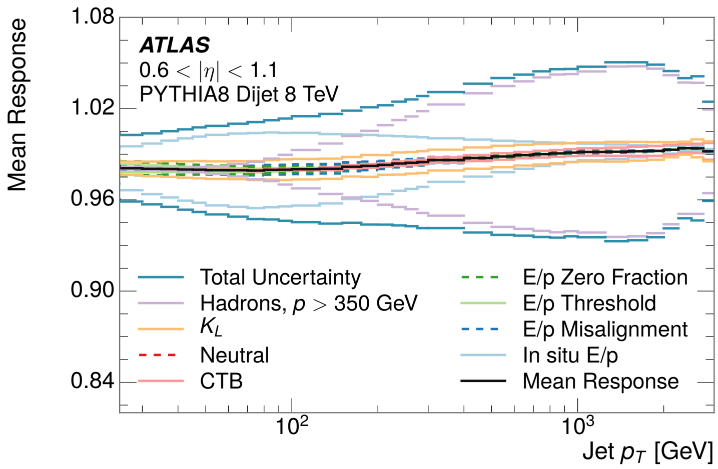

(b)

Figure 64: The JES response uncertainty contributions, as well as the total JES uncertainty, as a function of jet p_T for (a) $|\eta| < 0.6$ and (b) $0.6 < |\eta| < 1.1$.

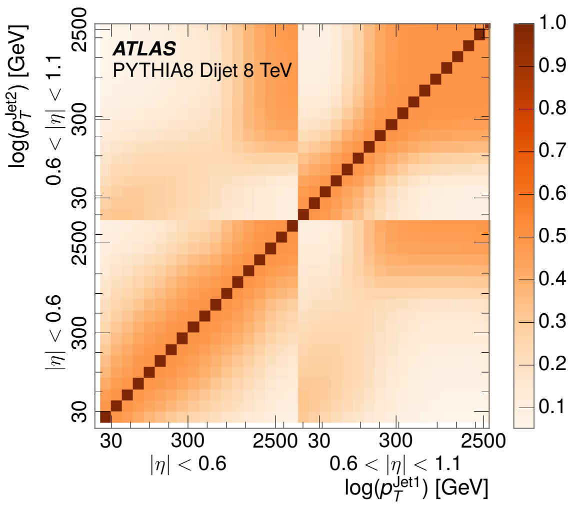

Figure 65: The correlations between bins of average reconstructed jet momentum as a function of jet p_T and $|\eta|$ for jets in the central region of the detector.

Part IV

SEARCH FOR LONG-LIVED PARTICLES

You can put some informational part preamble text here.

9

LONG-LIVED PARTICLES IN ATLAS

As discussed in Section 2.6, various limitations in the SM suggest a need for new particles at the TeV scale. A wide range of extensions to the Standard Model predict that these new particles can have lifetimes greater than approximately one-hundredth of a nanosecond. These include theories with universal extra-dimensions [65, 66], with new fermions [67], and with leptoquarks [68]. As discussed in Section 3.4, many SUSY theories also produce these LLPs, in both R-Parity violating [69–71] and R-Parity conserving [72–75] formulations. Split supersymmetry [8, 9], for example, predicts long-lived gluinos with O(TeV) masses. This search focuses specifically on the SUSY case, but many of the results are generic to any model with LLPs.

Long-lived gluinos or squarks carry color-charge and will thus hadronize into color neutral bound states called R-Hadrons. These are composit particles like the usual hadrons but with one supersymmetric constituent, for example $\tilde{g}q\bar{q}$ and $\tilde{q}\bar{q}$. Through this hadronization process, the neutral gluino can acquire a charge. Gluino pair production, $pp \to \tilde{g}\tilde{g}$ has the largest cross sectional increase with the increase in energy to 13 TeV, and so this search focuses on gluino R-Hadrons. Planned future updates will extend the case to explicitly include squark and chargino models, but the method covers any long-lived, charged, massive particle.

9.1 EVENT TOPOLOGY

The majority of SUSY models predict that gluinos will be produced in pairs at the LHC, through processes like $pp \to q\bar{q} \to \tilde{g}\tilde{g}$ and $pp \to gg \to \tilde{g}\tilde{g}$, where the gluon mode dominates for the collision energy and gluino masses considered for this search. During their production, the long-lived gluinos hadronize into color singlet bound states including $\tilde{g}q\bar{q}$, $\tilde{g}qqq$, and even $\tilde{g}g$ [76]. The probability to form the gluon-only bound states is a free parameter usually taken to be 0.1, while the meson states are favored among the R-Hadrons [77]. The charged and neutral states are approximately equally likely for mesons, so the R-Hadrons will be charged roughly 50% of the time.

These channels produce R-Hadrons with large p_{T}, comparable to their mass, so that they typically propagate with $0.2 < \beta < 0.9$ [77]. The fragmentation that produces that hadrons is very hard, so the jet structure around the R-Hadron is minimal, with less than 5 GeV of summed particle momentum expected in a cone of $\Delta R < 0.25$ around the R-Hadron [77]. After hadronization, depending on the gluino lifetime, the R-Hadrons then decay into hadrons and a LSP [76].

In summary, the expected event for pair-produced long-lived gluinos is very simple: two isolated, high-momentum R-Hadrons that propagate through the detector before decaying to jets. The observable features of such events depend strongly on the interaction of the R-Hadron with the material of the detector and also its lifetime. Section 9.1.1 describes the interactions of R-Hadrons which reach the various detector elements in ATLAS and Section 9.1.2 provides a summary of the observable event descriptions for R-Hadrons of various lifetimes.

9.1.1 DETECTOR INTERACTIONS

After approximately 0.2 ns, the R-Hadron reaches the pixel detector. If charged, it deposits energy into the material through repeated single collisions that result in ionization of the silicon substrate [6]. Because of its comparatively low β, the ionization energy can be significantly greater than expected for SM particles because the most-probable energy loss grows significantly as β decreases [6]. This large ionization can be measured through the ToT read out from the pixel detector as described in Section 6.1.2. Large ionization in the inner detector is one of the major characteristic features of LLPs.

Throughout the next few nanoseconds, the R-Hadron propagates through the remainder of the inner detector. A charged R-Hadron will provide hits in each of these systems as would any other charged particle, and can be reconstructed as a track. The track reconstruction provides a measurement of its trajectory and thus its momentum as described in Section 6.1. The large momentum is another characteristic feature of massive particles produced at the LHC. **Note: At this point I am failing to mention that the TRT provides a possible dE/dx measurement, because no one uses it as far as I know.**

As of roughly 20 ns, the R-Hadron enters the calorimeter where it interacts hadronically with the material. Because of its large mass and momentum, the R-Hadron does not typically stop in the calorimeter, but rather deposits a small fraction of its energy through repeated interactions with nucleons. The probability of interaction between the gluino itself and a nucleon is low because the cross section drops off with the inverse square of its mass, so the interactions are primarily governed by the light constituents [78]. Each of these interactions can potentially change that quark content and thus change the sign of the R-Hadron, so that the charge at exit is typically uncorrelated with the charge at entry [77]. The total energy deposited in the calorimeters during the propagation is small compared to the kinetic energy of the R-Hadron, around 20-40 GeV, so that E/p is typically less than 0.1 [77].

Then, 30 ns after the collision, it reaches the muon system, where it again ionizes in the material if charged and can be reconstructed as a muon track. Because of the charge-flipping interactions in the calorimeter, this track may have the opposite sign of the track reconstructed in the inner detector, or there may be a track present when there was none in the inner detector and vice-versa. The propagation time at the typically lower β results in a significant delay compared to muons, and that delay can be assessed in terms of a time-of-flight measurement. Because of the probability of charge-flip and late arrival, there is a significant chance that an R-Hadron which was produced with a charge will not be identified as a muon. The long time-of-flight is another characteristic feature of R-Hadrons which are reconstructed as muons.

9.1.2 LIFETIME DEPENDENCE

The above description assumed a lifetime long enough for the R-Hadron to exit the detector, which through this search is referred to as "stable", even though the particle may decay after exiting the detector. There are several unique signatures at shorter lifetimes where the R-Hadron decays in various parts of the inner detector; these lifetimes are referred to as "metastable".

The shortest case where the R-Hadron is considered metastable is for lifetimes around 0.01 ns, where the particle decays before reaching any of the detector elements. Although the R-Hadrons are produced opposite each other in the transverse plane, each R-Hadron decays to a jet and an LSP. The LSPs are not measured, so the produced jets can be significantly imbalanced in the transverse plane which results in large missing energy. That missing energy can be used to trigger candidate events, and provides the most efficient trigger option for shorter lifetimes. Additionally, the precision of the tracking system allows the displaced vertex of the R-Hadron decay to be reconstructed from the charged particles in the jet. The distance of that vertex from the interaction point can be used to distinguish R-Hadron decays from other processes. Figure 66 shows a schematic diagram of an example R-Hadron event with such a lifetime. The diagram is not to scale, but instead illustrates the detector interactions in the pixel detector, calorimeters, and muon system. It includes a representation of the charged R-Hadron and the neutral R-Hadron, as well as the LSPs and jets (shown as charged hadrons) produced in the decay. Neutral hadrons may also be produced in the decay but are not depicted. Previous searches on ATLAS have used the displaced vertex to target LLP decays [79].

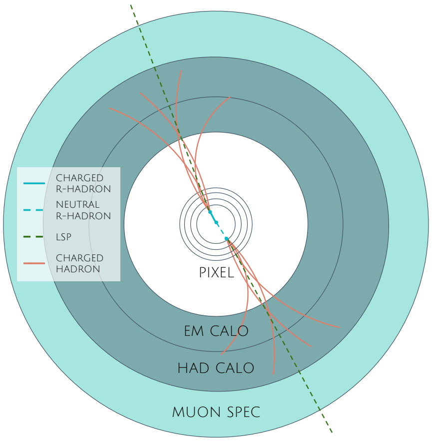

Figure 66: A schematic diagram of an R-Hadron event with a lifetime around 0.01 ns. The diagram includes one charged R-Hadron (solid blue), one neutral R-Hadron (dashed blue), LSPs (dashed green) and charged hadrons (solid orange). The pixel detector, calorimeters, and muon system are illustrated but not to scale.

The next distinguishable case occurs at lifetimes greater than 0.1 ns, where the R-Hadron forms a partial track in the inner detector. If the decay products are sufficiently soft, they may not be reconstructed, and this forms a unique signature of a disappearing track. An example of such an event is illustrated in Figure 67, which shows the short track in the inner detector and the undetected soft charged hadron and LSP that are produced. A dedicated search on ATLAS used the disappearing track signature to search for LLP in Run 1 [80]. z**Note: might not be worth mentioning the disapearing track here since it is actually a chargino search, the soft pion is pretty unique to charginos.**

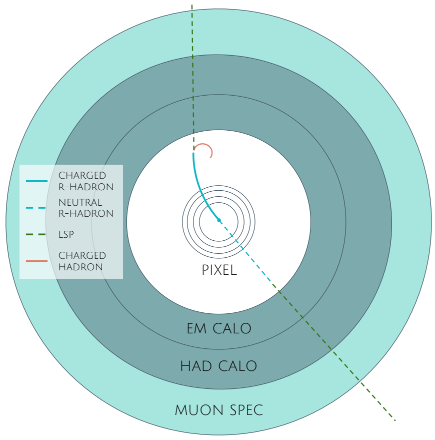

Figure 67: A schematic diagram of an R-Hadron event with a lifetime around 4 ns. The diagram includes one charged R-Hadron (solid blue), one neutral R-Hadron (dashed blue), LSPs (dashed green) and a charged hadron (solid orange). The pixel detector, calorimeters, and muon system are illustrated but not to scale.

If the decay products are not soft, the R-Hadron daughters form jets, resulting in an event-level signature of up to two high-momentum tracks, jets, and significant missing energy. The missing energy has the same origin as in the case of 0.01 ns lifetimes, from the decay to unmeasured particles, and again can be large. The high-momentum tracks will also have the characteristicly high-ioniziation of massive, long-lived paticles in the inner detector. Figure 68 illustrates an example event with one charged R-Hadron which decays after approximately 10 ns, and shows how the jets from the decay can still be reconstructed in the calorimeter. Several previous searches on ATLAS from Run 1 have used this signature to search for R-Hadrons [81, 82], including a dedicated search for metastable particles [83].

If the lifetime is longer than several nanoseconds, in the range of 15-30 ns, the R-Hadron decay can occur in or after the calorimeters, but prior to reaching the muon system. This case is similar to the above, although the jets may not be reconstructed, and is covered by many of the same search strategies. The events still often have large missing energy, although it is generated through different mechanisms. The R-Hadrons do not deposit much energy in the calorimeters, so a neutral R-Hadron will not enter into the missing energy calculation. A charged R-Hadron opposite a neutral R-Hadron will thus generate significant missing energy, and close to 50% of pair-produced R-Hadron events fall into this category. If both R-Hadrons are neutral then the missing energy will be low because neither is detected. Two charged R-Hadrons will also result in low missing energy because both are reconstructed as tracks and will balance each other in the trans-

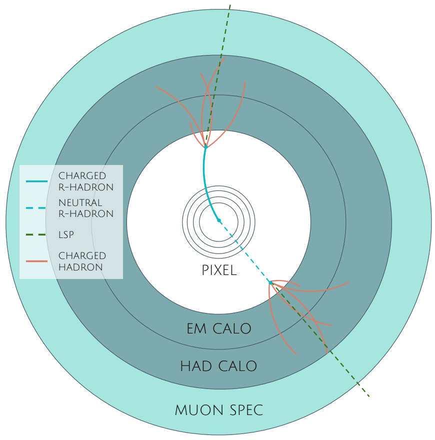

Figure 68: A schematic diagram of an R-Hadron event with a lifetime around 5 ns. The diagram includes one charged R-Hadron (solid blue), one neutral R-Hadron (dashed blue), LSPs (dashed green) and charged hadrons (solid orange). The pixel detector, calorimeters, and muon system are illustrated but not to scale.

verse plane. A small fraction of the time, one of the charged R-Hadron tracks may fail quality requirements and thus be excluded from the missing energy calculation and again result in signficant missing energy. Figure 69 illustrates another example event with one charged R-Hadron which decays after approximately 20 ns, and shows how the jets from the decay might not be reconstructed.

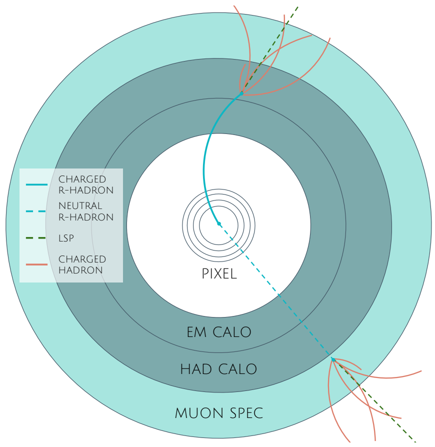

Figure 69: A schematic diagram of an R-Hadron event with a lifetime around 20 ns. The diagram includes one charged R-Hadron (solid blue), one neutral R-Hadron (dashed blue), LSPs (dashed green) and charged hadrons (solid orange). The pixel detector, calorimeters, and muon system are illustrated but not to scale.

The longest lifetimes, the stable case, has all of the features of the 30-50 ns case but with the addition of muon tracks for any R-Hadrons that exit the calorimeter with a charge. That muon track can provide additional information from time-of-flight measurements to help identify LLPs. An example of the event topology for one charged and one neutral stable R-Hadron is shown in Figure 70. Some searches on ATLAS have included this information to improve the search reach for stable particles [82, 84].

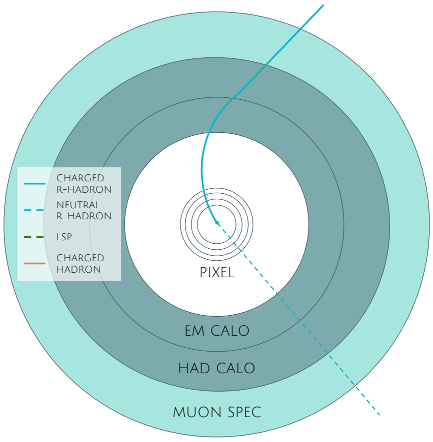

Figure 70: A schematic diagram of an R-Hadron event with a lifetime around 20 ns. The diagram includes one charged R-Hadron (solid blue) and one neutral R-Hadron (dashed blue). The pixel detector, calorimeters, and muon system are illustrated but not to scale.

9.2 SIMULATION

All of the event topologies discussed above are explored by simulations of R-Hadron events in the ATLAS detector. A large number of such samples are generated to determine signal efficiencies, to measure expected yields, and to estimate uncertainties. The primary interaction, pair production of gluinos with masses between 400 and 3000 GeV, is simulated using `Pythia 6.4.27` [85] with the AUET2B [86] set of tuned parameters for the underlying event and the CTEQ6L1 [62] PDF set. The simulated interactions include a modeling of pileup by adding secondary, minimum bias interactions from both the same (in-time pileup) and nearby (out-of-time pileup) bunch crossings. This event generation is then augmented with a dedicated hadronization routine to hadronize the long-lived gluinos into final states with R-Hadrons [87], with the probability to form a gluon-gluino bound set at 10% [88].

The cross sections used for these processes are calculated at next-to-leading order (NLO) in the strong coupling constant with a resummation of soft-gluon emmision at next-to-leading logarithmic (NLL) [89–93]. The nominal predictions and the uncertainties for each mass point are taken from an envelope of cross-section predictions using different PDF sets and factorization and renormalization scales [94].

The R-Hadrons then undergo a full detector simulation [], where the interactions of the R-Hadrons with the material of the detector are described by dedicated `Geant4` [32] routines. These routines model the interactions described in Section 9.1.1, including the ionizing interactions in the silicon modules of the inner detector and the R-Hadron-nucleon interactions in the calorimeters [95, 96]. The specific routine chosen to describe the interactions of the R-Hadrons with nucleons, the "generic model", uses a pragmatic approach where the scattering cross section is taken to be a constant 12 mb per light quark. In this model the gluino itself does not interact at all except through its role as a reservoir of kinetic energy.

The lifetimes of these R-Hadrons are then simulated at several working points, $\tau = 0.1, 1.0, 3.0, 10, 30, 50$ and detector stable, where the particle is required to decay after propagating for a time compatible with its lifetime. Only one decay mode is simulated for these samples, $\tilde{g} \rightarrow q\bar{q}\tilde{\chi}_1^0$ with the neutralino mass set to 100 GeV, which is chosen because it has the highest sensitivity among all of the modes studied in previous searches [83]. Heavier neutralinos have similar results but generate less missing energy which reduces the efficiency of triggering.

All of the simulated events are then reconstructed using the same software used for collision data. The fully reconstructed events are then reweighted to match the distribution of initial state radiation in an alternative sample of events, generated with `MG5_aMC@NLO` [97], which has a more accurate description of radiate effects than `Pythia6`. This reweighting provides a more accurate description of the momentum of the gluino-gluino system and is important in modeling the efficiency of triggering and offline event selection.

10 EVENT SELECTION

The LLPs targeted by this search differ in their interactions with the detector from SM particles primarily because of their large mass. When produced at the energies available at the LHC, that large mass results in a low β (typically $0.2 < \beta < 0.9$). Such slow-moving particles heavily ionize in detector material. Each layer of the pixel detector provides a measurement of that ionization, through ToT, as discussed in Section 6.1.2. The ionization in the pixel detector, quantified in terms of dE/dx, provides the major focus for this search technique, along with the momentum measured in the entire inner detector. It is effective both for its discriminating power and its use in reconstructing a particle's mass, and it can be used for a wide range of masses and lifetimes as discussed in Section 9.1.2. However dE/dx needs to be augmented with a few additional selection requirements to provide a mechanism for triggering and to further reduce backgrounds.

Ionization itself is not currently accessible for triggering, so this search instead relies on E_T^{miss} to trigger signal events. Although triggering on E_T^{miss} can be inefficient, E_T^{miss} is often large for many production mechanisms of LLPs, as discussed in Section 9.1.

The use of ionization to reject SM backgrounds relies on well-measured, high-momentum tracks, so some basic requirements on quality and kinematics are placed on the tracks considered in this search. These quality requirements have been significantly enhanced in Run 2 by a newly introduced tracking variable that is very effective in removing highly-ionizing backgrounds caused by overlapping tracks. A few additional requirements are placed on the tracks considered for LLP candidates that increase background rejection by targeting specific types of SM particles. These techniques provide a significant analysis improvement over previous iterations of ionization-based searches on ATLAS by providing additional background rejection with minimal loss in signal efficiency.

The ionization measurement with the Pixel detector can be calibrated to provide an estimator of $\beta\gamma$. That estimate, together with the momentum measurement provided by tracking, can be used to reconstruct a mass for each track which traverses the pixel detector. That mass variable will be peaked at the LLP mass for any signal, and provides an additional tool to search for an excess. In addition to an explicit requirement on ionization, this search constructs a mass-window for each targeted signal mass in order to evaluate any excess of events and to set limits.

The strategy discussed here is optimized for lifetimes of $O(1)$ - $O(10)$ ns. Pixel ionization is especially useful in this regime as particles only need to propagate through the first seven layers of the inner detector, about 37 cm from the beam axis. The search is still competitive with other searches for LLPs at longer lifetimes, because the primary discriminating variables are still applicable even for particles that do not decay within the detector [84]. Although the majority of the requirements will be the same for all lifetimes, two signal regions are defined to optimize separately for intermediate and long lifetime particles.

10.1 TRIGGER

Triggering remains a significant difficulty in defining an event selection with high signal efficiency in a search for LLPs. There are no triggers available in the current ATLAS system that can fire directly from a high momentum track with large ionization (Section 5.6). Although in some configurations a charged LLP can fire muon triggers, this requirement introduces significant model dependence on both the allowed lifetimes and the interactions in the calorimeter [77], as discussed in Section 9.1.1.

For a search targeting particles which may decay prior to reaching the muon system, the most efficient available trigger is based on missing energy [77]. As discussed in Section 9.1, signal events can produce significant E_T^{miss} by a few mechanisms. At the trigger level however, the missing energy is only calculated using the calorimeters (Section 5.6) where the R-Hadrons deposit little energy. So, at short lifetimes, E_T^{miss} measured in the calorimeter is generated by an imbalance between the jets and undetected LSPs produced in R-Hadron decays. At longer lifetimes, without the decay products, missing energy is only produced in the calorimeters when the R-Hadrons recoil against an ISR jet.

These features are highlighted in Figure 71, which shows the E_T^{miss} distributions for simulated short lifetime (3 ns) and stable R-Hadron events. The figure includes both the offline E_T^{miss}, the missing energy calculated with all available information, and Calorimeter E_T^{miss}, the missing energy calculated using only information available at the calorimeter which approximates the missing energy available at the trigger. The short lifetime sample has significantly greater E_T^{miss} and Calorimeter E_T^{miss} than the stable sample as expected. For the stable sample, a small fraction of events with very large E_T^{miss} (about 5%) migrate into the bin with very small Calorimeter E_T^{miss} because the E_T^{miss} produced by a charged R-Hadron track opposite a neutral R-Hadron track does not contribute any missing energy in the calorimeters.

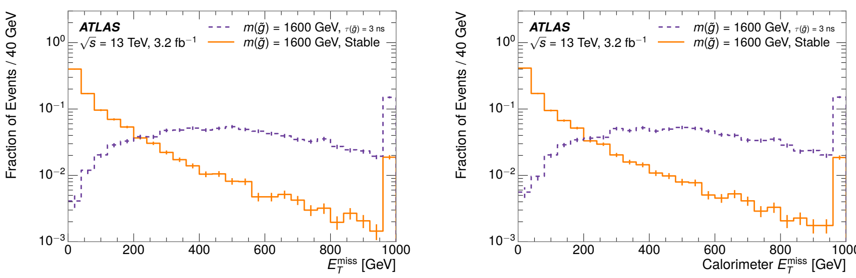

(a) (b)

Figure 71: The distribution of (a) E_T^{miss} and (b) Calorimeter E_T^{miss} for simulated signal events before the trigger requirement.

So, either case to some extent relies on kinematic degrees of freedom to produce missing energy, as the pair-produced LLPs tend to balance each other in the transverse plain. That balance results in a relatively low efficiency for long-lifetime particles, roughly 40%, and efficiencies between 65% and 95% for shorter lifetimes depending on both the mass and the lifetime. For long lifetimes in particular, the presence of ISR is important in providing an imbalance in the transverse plane, and is an important aspect of modeling the selection efficiency for R-Hadron events.

The missing energy trigger with the lowest threshold available is chosen for this selection in order to maximize the trigger efficiency. During 2015 data collection this was the `HLT_xe70` trigger, which used a 50 GeV threshold on missing energy at `LVL1` and a 70 GeV threshold on missing energy at the `HLT`. These formation of the trigger decision for missing energy was discussed in more detail in Section 5.6.

10.2 KINEMATICS AND ISOLATION

After the trigger requirement, each event is required to have a primary vertex reconstructed from at least two well-measured tracks in the inner detector, each with $p_{\mathrm{T}} > 400$ MeV. If more than one such vertex exists, the primary vertex is taken to be the one with the largest summed track momentum for all tracks associated to that vertex. The offline reconstructed E_T^{miss} is required to be above 130 GeV to additionally reject SM backgrounds. The transverse missing energy is calculated using fully reconstructed and calibrated offline objects, as described in Section 6.5. In particular the E_T^{miss} definition in this selection uses jets reconstructed with the anti-k_t algorithm with radius $R = 0.4$ from clusters of energy in the calorimeter (Section 6.4) and with $p_T > 20$ GeV, as well as reconstructed muons, electrons, and tracks not identified as another object type.

The E_T^{miss} distributions are shown for data and a few simulated signals in Figure 72, after the trigger requirement. The cut placed at 130 GeV is 95% efficient for metastable and 90% efficient for stable particles, after the trigger requirement, because of the missing energy generating mechanisms discussed previously. The distribution of data in this figure and subsequent figures in this section can be interpreted as the distribution of backgrounds, as any signal contamination would be negligible if present at these early stages of the selection (prior to the final requirement on ionization). The background falls rapidly with missing energy, motivating the direct requirement on E_T^{miss} for the signal region. Although a tighter requirement than the specified value of 130 GeV would seem to increase the search potential from these early distributions, other requirements are more optimal when taken as a whole. The specific values for each requirement in signal region were optimized considering the increase in discovery reach for tightening the requirement on each discriminating variable. **NOTE: If space and time permit, I will add a whole section about signal region optimization..**

It is typically the practice for searches for new physics on ATLAS to place an offline requirement on the triggering variable that is sufficiently tight to guar-

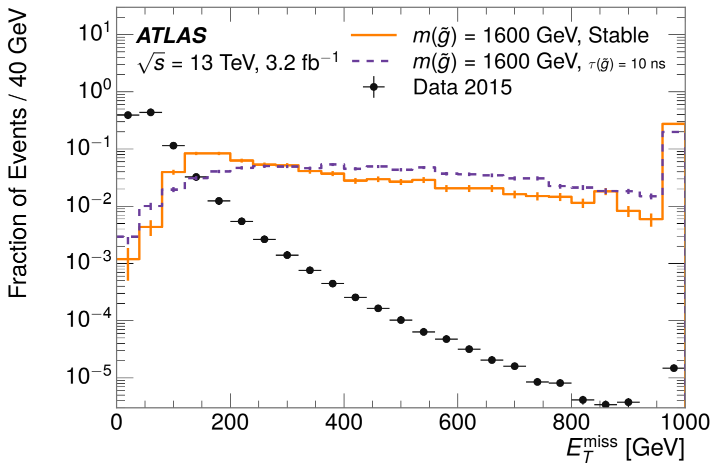

Figure 72: The distribution of E_T^{miss} for data and simulated signal events, after the trigger requirement.

antee that the event would pass the trigger. Such a tight requirement makes the uncertainty on the trigger efficiency of the simulation negligible, as modeling the regime where the trigger is only partially efficient can be difficult. In this analysis, however, because of the atypical interactions of R-Hadrons with the tracker and the calorimeter, the offline requirement on E_T^{miss} is not sufficient to guarantee a 100% trigger efficiency even at large values, as can be seen in Figure 73. This figure shows the efficiency for passing the `HLT_xe70` trigger as a function of the requirement on E_T^{miss}, which plateaus to roughly 85% even at large values. This plateau does not reach 100% because events which have large offline missing energy from a neutral R-Hadron produced opposite of a charged R-Hadron can have low missing energy in the calorimeters. The Calorimeter E_T^{miss}, on the other hand, does not have this effect and reaches 100% efficiency at large values because it is the quantity that directly corresponds to the trigger threshold. In both cases the efficiency of triggering is greater for the short lifetime sample because the late decays to hadrons and LSPs produce an imbalance in the calorimeters even though they may not be reconstructed offline as tracks or jets. For this reason, the requirement on E_T^{miss} is determined by optimizing the background rejection even though it corresponds to a value of trigger efficiency significantly below 1.0.

Potential signal events are then required to have at least one candidate LLP track. Although the LLPs are produced in pairs, many models do not consistently yield two charged particles. For example, in the R-Hadron model highlighted here, only 20% of events have two charged R-Hadrons while 47% of events have just one. A signal region requiring two charged candidates could be a powerful improvement in background rejection for a larger dataset, but it is not considered in this version of the analysis as it was found to be unnecessary to reject the majority of backgrounds.

For a track to be selected as a candidate, it must have $p_T > 50$ GeV and pass basic quality requirements. The track must be associated to the primary vertex.

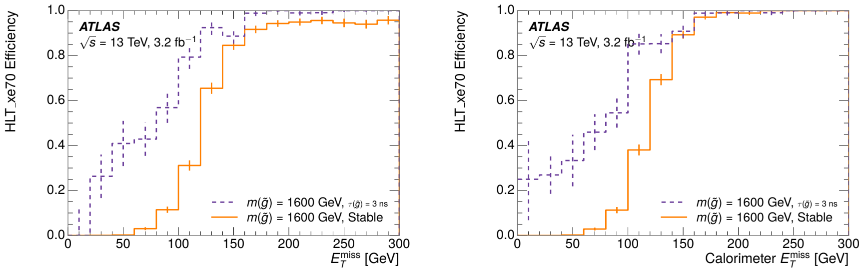

(a) (b)

Figure 73: The trigger efficiency for the `HLT_xe70` trigger requirement as a function of (a) E_T^{miss} and (b) Calorimeter E_T^{miss} for simulated signal events.

It must also have at least seven clusters in the silicon layers in the inner detector to ensure an accurate measurement of momentum. Those clusters must include one in the innermost layer if the extrapolated track is expected to pass through that layer. And to ensure a reliable measurement of ionization, the track is required to have at least two clusters in the pixel detector that provide a measurement of dE/dx.

At this point in the selection, there is a significant high-ionization background from multiple tracks that significantly overlap in the inner detector. Previous version of this analysis have rejected these overlaps by an explicit overlap rejection between pairs of fully reconstructed tracks, typically by requiring no additional tracks within a cone around the candidate. This technique, however, fails to remove the background from tracks that overlap so precisely that the tracks cannot be separately resolved, which can be produced in very collimated photon conversions or decays of pions.

A new method, added in Run 2, identifies cluster shapes that are likely formed by multiple particles based on a neural network classification algorithm. The number of clusters that are classified this way in the pixel detector for a given track is called N_{split}. As the shape of clusters requires significantly less spatial separation to identify overlaps than it does to reconstruct two fully resolved tracks, this variable is more effective at rejecting backgrounds from overlaps. Figure 74 shows the dependence of ionization on N_{split}; as N_{split} increases the most probable value of dE/dx grows significantly up to twice the expected value when $N_{\text{split}} = 4$.

This requirement is very successful in reducing the long positive tail of the dE/dx distributions, as can be seen in Figure 75. Comparing the distribution for "baseline tracks", tracks with only the above requirements on clusters applied and before the requirement on N_{split}, to the distribution with $N_{\text{split}} = 0$, it is clear that the fraction of tracks with large dE/dx is reduced be several orders of magnitude. The tracks without split hits are very close to the dE/dx distribution of identified muons, which are extremely well isolated on average. Figure 75 also includes the distribution of dE/dx in an example signal simulation to demonstrate how effective dE/dx is as a discriminating variable with this isolation applied. The background falls rapidly for $dE/dx > 1.8$ MeVg^{-1}cm^2

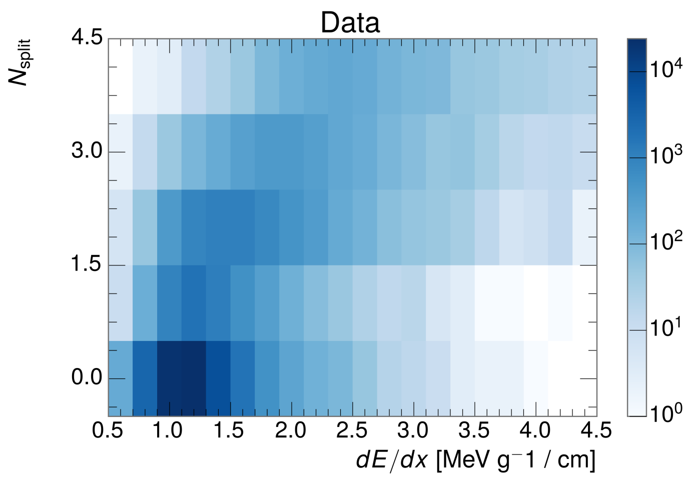

Figure 74: The dependence of dE/dx on N_{split} in data after basic track hit requirements have been applied.

while the majority of the signal, approximately 90% depending on the mass, falls above that threshold. Over 90% of LLP tracks in simulated signal events pass the N_{split}-based isolation requirement.

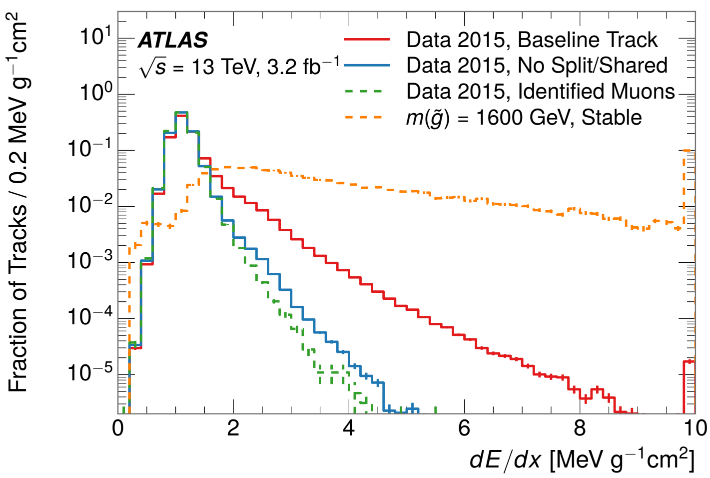

Figure 75: The distribution of dE/dx with various selections applied in data and simulated signal events.

A few additional kinematic requirements are imposed to help reduce SM backgrounds. The momentum of the candidate track must be at least 150 GeV, and the uncertainty on that measurement must be less than 50%. The distribution of momentum is shown in Figure 76 for tracks in data and simulated signal events after the previously discussed requirements on clusters, transverse momentum, and isolation have been imposed. The signal particles are much harder on average than their backgrounds because of the high energy interactions required to produce them. The transverse mass, M_{T}, defined as

$$M_{\mathrm{T}} = \sqrt{2 p_{\mathrm{T}} E_T^{\mathrm{miss}} (1 - \cos(\Delta\phi(E_T^{\mathrm{miss}}, \mathrm{track})))} \tag{20}$$

estimates the mass of a decay of to a single charged particle and an undetected particle and is required to be greater than 130 GeV to reject contributions from the decay of W bosons. Figure 77 shows the distribution of M_{T} for data and simulated signal events. The signal is distributed over a wide range of M_{T}, with about 90% above the threshold value of 130 GeV. The data shows a dual-peaked structure, where the first peak comes from W boson decays and the second peak is a kinematic shaping from the requirements on E_T^{miss} and the track p_{T} in dijet events.

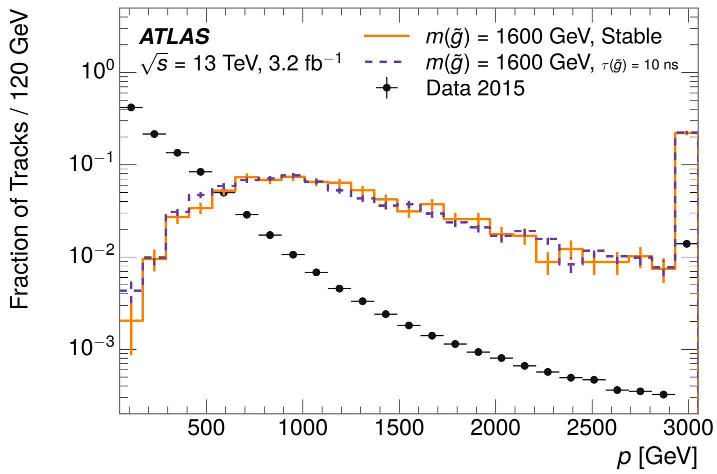

Figure 76: The distribution of track momentum for data and simulated signal events, after previous selection requirements have been applied.

10.3 PARTICLE SPECIES REJECTION

The amount of ionization deposited by particles with low mass and high momentum has a large positive tail [6], so backgrounds can be formed by a wide variety of SM processes when various charged particles have a few randomly large deposits of energy in the pixel detector. Those backgrounds can be additionally reduced by targeting other interactions with the detector where they are expected to have different behavior than R-Hadrons. The interactions with the detector depend on the types of particles produced rather than the processes which produce them, so this search forms a series of rejections to remove backgrounds from individual particle species. These rejections focus on using additional features of the event, other than the kinematics of the candidate track, as they can provide a powerful source of background rejection with very high signal efficiency. However, the lifetime of an R-Hadron can significantly change

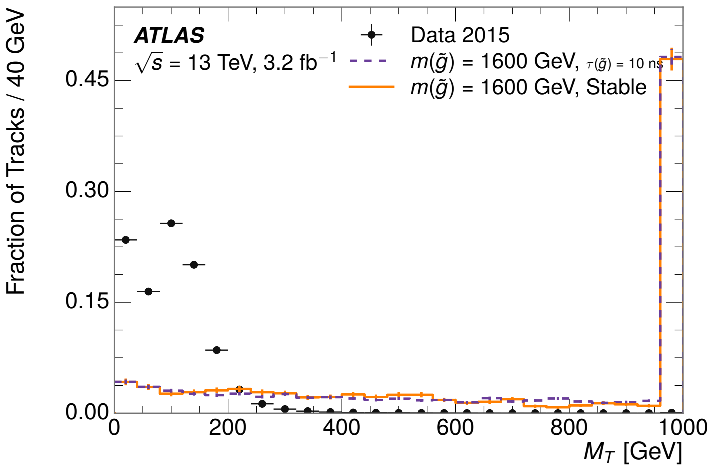

Figure 77: The distribution of M_T for data and simulated signal events, after previous selection requirements have been applied.

its detector characteristics, as discussed in Section 9.1.2. To accommodate these differences, the SM rejections defined in this section are split to form two signal regions, one for long-lifetimes particles, the stable region ($50 <= \tau[\text{ns}] < \inf$ ns), and one for intermediate lifetime particles, the metastable region ($0.4 < \tau[\text{ns}] < 50$).

Jets can be very effectively rejected by considering the larger-scale isolation of the candidate track. In this case the isolation focuses on the production of nearby particles as a jet-veto, rather than the isolation from overlapping tracks based on N_{split} that was used to reduce high-ionization backgrounds. As explained in Section 9.1, the fragmentation process which produces an R-Hadron is very hard and thus is not expected to produce additional particles with a summed momentum of more than 5 GeV. The jet-veto uses the summed momentum of tracks with a cone of $\Delta R < 0.25$, referred to as p_T^{Cone}, which is shown in Figure 78 for data and simulated signal events. In the data this value has a peak at zero from isolated tracks such as leptons, and a long tail from jets which contains as much as 80% of the background above 20 GeV at this stage of the selection. In signal events p_T^{Cone} is strongly peaked at zero and significantly less than 1% of signal events have p_T^{Cone} above 20 GeV. This makes a requirement of $p_T^{\text{Cone}} < 20$ GeV a very effective method to reject background without losing signal efficiency. For the stable signal region, this cut is further tightened to $p_T^{\text{Cone}} < 5$ GeV as it is the most effective variable remaining to extend the search reach for long lifetimes.

Even for fully isolated particles, there are additional methods to reject each type of particle using information in the muon system and calorimeters. Muons can be identified very reliably using the tracks in the muon system, as described in Section 6.3. For intermediate lifetimes the LLPs do not survive long enough to reach the muon system, and so muons are vetoed by rejecting tracks that associate to a muon with medium muon identification requirements (Section 6.3). For longer lifetimes, this rejection is not applied because LLPs which reach the

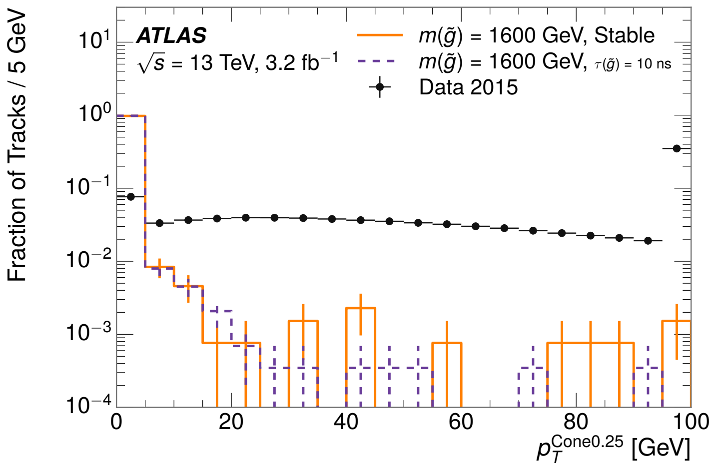

Figure 78: The distribution of summed tracked momentum within a cone of $\Delta R < 0.25$ around the candidate track for data and simulated signal events, after previous selection requirements have been applied.

muon system can be identified as muons as often as 30% of the time in simulated samples.

Calorimeter-based particle rejection relies on the expected small deposits of energy from LLPs. When the lifetime is long enough to reach the calorimeter, a LLP deposits little of its energy as it traverses the material, as discussed in Section 9.1. Even when the particle does decay before the calorimeter, the majority of its energy is carried away by the LSP and not deposited in the calorimeter. In both cases the energy is expected to be distributed across the layers of the calorimeters and not peaked in just one layer. This can be quantified in terms of E/p, the ratio of calorimeter energy of a nearby jet to the track momentum, and f_{EM}, the fraction of energy in that jet within the electromagnetic calorimeter. When no jets fall within a cone of 0.05 of the particle, E/p and f_{EM} are both defined as zero. E/p is expected to be above 1.0 for typical SM particles because of calibration and the contributions from other nearby particles, as discussed in Chapter 7. At these momenta there is no significant zero fraction due to interactions with the detector or insufficient energy deposits (see Section 7.2.2). f_{EM} is peaked close to 1.0 for electrons, and distributed between 10% and 90% for hadrons.

These trends can be seen in the two dimensional distribution for signal in Figure 79 for stable and metastable (10 ns) events. The majority of R-Hadrons in both samples fall into the bin for $E/p = 0$ and $f_{\mathrm{EM}} = 0$ because the majority of the time there is no associated jet. In the stable sample, when there often is an associated jet, E/p is typically still below 0.1, and the f_{EM} is predominantly under 0.8. In the metastable sample, on the other hand, E/p is larger but still typically below 0.1 because of actual jets produced during the decay. The f_{EM} is much lower on average in this case, below 0.1, because the 10 ns lifetime particles rarely decay before passing through the electromagnetic calorimeter. Figure 79 also includes simulated Z decays to electrons or tau leptons. From the decays to electrons it is clear that the majority of electrons have f_{EM} above 0.9. The tau decays include a variety of products. Muons can be seen in the bin where $E/p = 0$ and $f_{\mathrm{EM}} = 0$ because they do not have an associated jet. Electrons fall into the range where $E/p > 1$ and $f_{\mathrm{EM}} > 0.9$. Hadronic tau decays are the most common, and fall in the range of $0.1 < f_{\mathrm{EM}} < 0.9$ and $E/p > 1.0$.

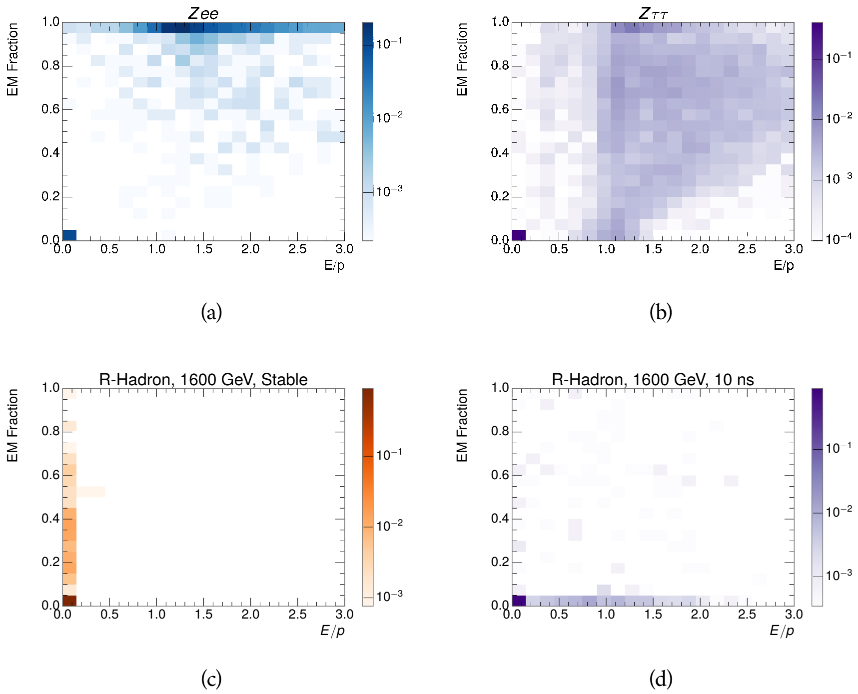

Figure 79: The normalized, two-dimensional distribution of E/p and f_{EM} for simulated (a) $Z \rightarrow ee$, (b) $Z \rightarrow \tau\tau$, (c) 1200 GeV Stable R-Hadron events, and (d) 1200 GeV, 10 ns R-Hadron events.

These differences motivate an electron rejection by requiring an f_{EM} below 0.9. Similarly, isolated hadrons are rejected by requiring $E/p < 1.0$. These requirements combine to remove the majority of isolated electrons and hadrons but retain over 95% of the simulated signal across a range of masses and lifetimes.

10.4 IONIZATION

The final requirement on the candidate track is the primary discriminating variable, the ionization in the pixel detector. That ionization is measured in terms of dE/dx, which was shown for data and simulated signal events in Figure 75. dE/dx is dramatically greater for the high mass signal particles than the backgrounds, which start to fall immediately after the minimally ionizing peak at 1.1 MeVg^{-1}cm^{2}. The dE/dx for candidate tracks must be greater than a pseudorapidity-dependent threshold, specifically $1.80 - 0.11|\eta| + 0.17\eta^2 - 0.05|\eta|^3$ MeV g^{-1} cm^{-2}, in order to correct for an approximately 5% dependence of the MIP peak on η. The requirement was chosen as part of the signal region optimization, and man-

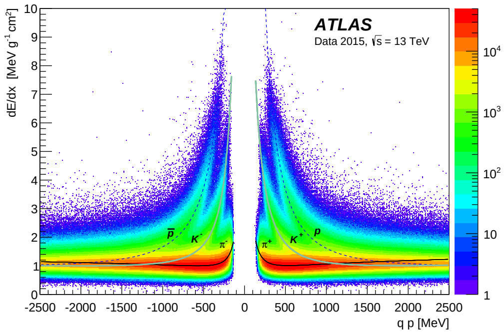

Figure 80: Two-dimensional distribution of dE/dx versus charge signed momentum (qp) for minimum-bias tracks. The fitted distributions of the most probable values for pions, kaons and protons are superimposed.

ages to reduce the backgrounds by a factor of 100 while remaining 70-90% efficient for simulated signal events depending on the mass.

10.4.1 MASS ESTIMATION

The mean value of ionization in silicon is governed by the Bethe equation and the most probable value follows a Landau-Vavilov distribution [6]. Those forms inspire a parametric description of dE/dx in terms of $\beta\gamma$,

$$(dE/dx)_{\mathrm{MPV}}(\beta\gamma) = \frac{p_1}{\beta^{p_3}} \ln(1 + [p_2\beta\gamma]^{p_5}) - p_4 \tag{21}$$

which performs well in the range $0.3 < \beta\gamma < 1.5$. This range includes the expected range of $\beta\gamma$ for the particles targeted for this search, with $\beta\gamma \approx 2.0$ for lower mass particles (O(100 GeV)) and up to $\beta\gamma \approx 0.5$ for higher mass particles (O(1000 GeV)). The parameters, p_i, are fit using a 2015 data sample of low-momentum pions, kaons, and protons as described in Ref. [98]. Figure 80 shows the two-dimensional distribution of dE/dx and momentum along with the above fitted values for $(dE/dx)_{\mathrm{MPV}}$.

The above equation (21) is then numerically inverted to estimate $\beta\gamma$ and the mass for each candidate track. In simulated signal events, the mean of this mass value reproduces the generated mass up to around 1800 GeV to within 3%, and 3% shift is applied to correct for this difference. The mass distributions prior to this correction are shown for a few stable mass points in Figure 81. The large widths of these distributions come from the high variability in energy deposits in the pixel detector as well as the uncertainty on momentum measurements at high momentum, but the means converge to the expected values.

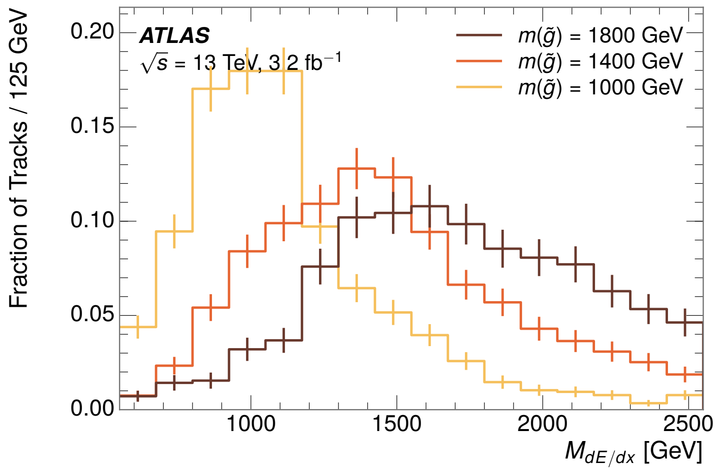

Figure 81: The distribution of mass estimated using dE/dx for simulated stable R-Hadrons with masses between 1000 and 1600 GeV.

This analysis evaluates expected yields and the resulting cross sectional limits using windows in this mass variable. The windows are formed by fitting mass distributions in simulated signal events like those in Figure 81 to Gaussian distributions and taking all events that fall within $\pm 1.4\sigma$ of the mean. As can be seen in Figure 81, typical values for this width are $\sigma \approx 300 - 500$ GeV depending on the generated mass.

10.5 EFFICIENCY

The numbers of events passing each requirement through ionization are shown in Table 9 for the full 2015 dataset and a simulated 1600 GeV, 10 ns lifetime R-Hadron sample. The table highlights the overall acceptance × efficiency for signal events, which for this example is 19%. Between SM rejection and ionization, this signal region reduces the background of tracks which pass the kinematic requirements down by an additional factor of almost 2000.

There is a strong dependence of this efficiency on lifetime and mass, with efficiencies dropping to under 1% at low lifetimes. Figure 82 shows the dependence on both mass and lifetime for all signal samples considered in this search. The dependence on mass is relatively slight and comes predominantly from the increasing fraction of R-Hadrons which pass the ionization cut with increasing mass. The trigger and E_T^{miss} requirements are most efficient for particles that decay before reaching the calorimeters. However, the chance of a particle to be reconstructed as a high-quality track decreases significantly at low lifetimes as the particle does not propagate sufficiently through the inner detector. These effects lead to a maximum in the selection efficiency for lifetimes around 10-30 ns.

The inefficiency of this signal region at short lifetimes comes almost exclusively from an acceptance effect, in that the particles do not reach the necessary

Selection	Exp. Signal Events	Observed Events in 3.2 fb^{-1}
Generated	26.0 ± 0.3	
E_T^{miss} Trigger	24.8 ± 0.3 (95%)	
$E_T^{\text{miss}} > 130$ GeV	23.9 ± 0.3 (92%)	
Track Quality and $p_{\text{T}} > 50$	10.7 ± 0.2 (41%)	368324
Isolation Requirement	9.0 ± 0.2 (35%)	108079
Track $p > 150$ GeV	6.6 ± 0.2 (25%)	47463
$M_{\text{T}} > 130$ GeV	5.8 ± 0.2 (22%)	18746
Electron and Hadron Veto	5.5 ± 0.2 (21%)	3612
Muon Veto	5.5 ± 0.2 (21%)	1668
Ionization Requirement	5.0 ± 0.1 (19%)	11

Table 9: The expected number of events at each level of the selection for metastable 1600 GeV, 10 ns R-Hadrons, along with the number of events observed in data, for 3.2 fb^{-1}. The simulated yields are shown with statistical uncertainties only. The total efficiency × acceptance is also shown for the signal.

layers of the SCT. This can be seen more clearly by defining a fiducial region which includes events with at least one R-Hadron that is produced with non-zero charge, $p_{\text{T}} > 50$ GeV, $p > 150$ GeV, $|\eta| < 2.5$, and a decay distance greater than 37 cm in the transverse plane. At short (1 ns) lifetimes, the acceptance into this region is as low as 4%. Once this acceptance is accounted for, the selection efficiency ranges from 25% at lifetimes of 1 ns up to 45% at lifetimes of 10 ns.

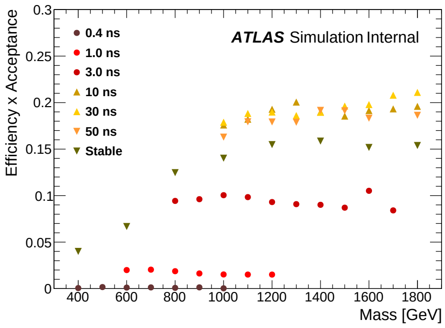

(a)

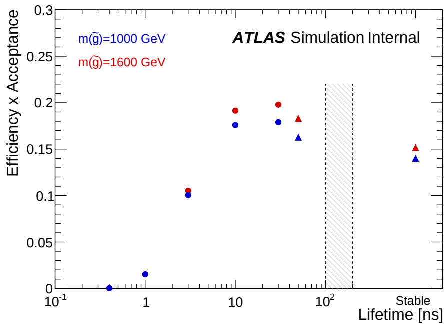

(b)

Figure 82: The acceptance × efficiency as a function of R-Hadron (a) mass and (b) lifetime. (a) shows all of the combinations of mass and lifetime considered in this search, and (b) highlights the lifetime dependence for 1000 GeV and 1600 GeV R-Hadrons.

11

BACKGROUND ESTIMATION

The event selection discussed in the previous section focuses on detector signatures, emphasizing a single high-momentum, highly-ionizing track. That track is then required to be in some way inconsistent with the expected properties of SM particles, with various requirements designed to reject jets, hadrons, electrons, and muons (Section 10.3). Therefore the background for this search comes entirely from reducible backgrounds that are outliers of various distributions including dE/dx, f_{EM}, and p_T^{Cone}. The simulation can be tuned in various ways to do an excellent job of modeling the average properties of each particle type [99], but it is not necessarily expected to accurately reproduce outliers. For this reasons, the background estimation used for this search is estimated entirely using data.

11.1 BACKGROUND SOURCES

SM charged particles with lifetimes long enough to form tracks in the inner detector can be grouped into three major categories based on their detector interactions: hadrons, electrons, and muons. Every particle that enters into the background for this search belongs to one of these types. Relatively pure samples of tracks from each of these types can be formed in data by inverting the various rejection techniques in Section 10.3. Specifically, muons are selected requiring medium muon identification, electrons requiring $E/p > 1.0$ and $f_{\mathrm{EM}} > 0.95$, and hadrons requiring $E/p > 1.0$ and $f_{\mathrm{EM}} < 0.95$.

Figure 83 shows the distributions of momentum and dE/dx for these categories in data, after requiring the event level selection as well as the track requirements on p_{T}, hits, and N_{split}, as discussed in Section 10.2. Simulated signal events are included for reference. These distribution are only illustrative of the differences between types, as the rejection requirements could alter their shape. This is especially significant for momentum which enters directly into E/p and can indirectly affect muon identification. However the various types show clear differences in both distributions. The distributions of momentum are not necessarily expected to match between the various types because the production mechanisms for each type result in different kinematic distributions. dE/dx is also different between types because of incomplete isolation; although the requirement on N_{split} helps to reduce the contribution of nearby particles it does not completely remove the effect of overlaps. Muons are better isolated because they do not have the additional particle from hadronization present for hadrons and they are significantly less likely do interact with the detector and produce secondary particles compared to hadrons and electrons. Thus muons have the smallest fraction of dE/dx above the threshold of 1.8 $\mathrm{MeV g^{-1} cm^2}$; hadrons and electrons have a larger fraction above this threshold.

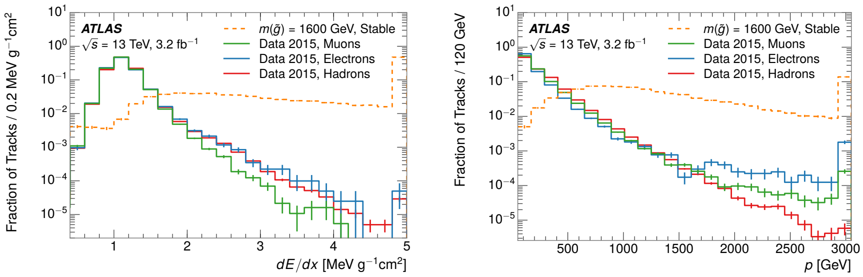

(a) (b)

Figure 83: The distribution of (a) dE/dx and (b) momentum for tracks in data and simulated signal after requiring the event level selection and the track selection on p_T, hits, and N_{split}. Each sub-figure shows the normalized distributions for tracks classified as hadrons, electrons, and muons in data and R-Hadrons in the simulated signal.

It is difficult to determine what fraction of each particle type enters into the final signal region. The background method will not have significant dependence on the relative contributions of each species, but it is useful to understand the differences between each when considering the various tests of the method.

11.2 PREDICTION METHOD

The data-driven background estimation relies on the independence between ionization and other kinematic variables in the event. For standard model particles with momenta above 50 GeV, dE/dx is not correlated with momentum; though there is a slight relativistic rise as momentum increases, the effect is small compared to the width of the distribution of ionization energy deposits.. So, the proposed method to estimate the mass distribution of the signal region is to use momentum from a track with low dE/dx (below the threshold value) and to combine it with a random dE/dx value from a dE/dx template. The resulting track is just as likely as the original, so a number of such random generations provide the expected distributions of momentum and ionization. These are then combined using the parametrization described in Section 10.4.1 to form a distribution of mass for the signal region.

Algorithmically this method is implemented by forming two distinct Control Regions (CRs). The first CR, CR1, is formed by applying the entire event selection from Chapter 10 up to the dE/dx and mass requirements. The dE/dx requirement is instead inverted for this region. Because of the independence of dE/dx, the tracks in this control region have the same kinematic distribution as the tracks in the signal region, and are used to measure a two-dimensional template of p and η. The second CR, CR2, is formed from the event selection through the dE/dx requirement, but with an inverted E_T^{miss} requirement. The tracks in this control region are expected to have similar dE/dx distributions to the signal region before the ionization requirement, and so this region is used to measure a two-dimensional template of dE/dx and η.

The contribution of any signal to the control regions is minimized by the inverted selection requirements. Only less than 10% of simulated signal events have either dE/dx or E_T^{miss} below the threshold values in the original signal region, while the backgrounds are significantly enhanced by inverting those requirements. The signal contamination is less than 1% in both control regions for all of the simulated masses and lifetimes considered in this analysis.

With those measured templates, the shape of the mass estimation is generated by first selecting a random (p, η) combination from CR1. This momentum value is combined with a dE/dx value taken from the appropriate distribution of dE/dx for the selected η from CR2. The use of η in both random samplings controls for any correlation between p, dE/dx, and η. Those values are then used to calculate a mass in the same way that is done for regular tracks in data, see Section 10.4.1. As this procedure includes all dE/dx values, the cut at 1.8 MeVg^{-1}cm^2 is then enforced to fully model the signal region. The generated mass distribution is then normalized by scaling the background estimate to the data in the region $M < 160$ GeV, where signals of this type have already been excluded [83]. This normalization uses the distributions of mass generated without the ionization requirement.

The statistical uncertainties on these background distributions are calculated by independently fluctuating each bin of the input templates according to their Poisson uncertainties. These fluctuations are repeated a large number of times, and the uncertainty on the resulting distribution is taken as the root mean square (RMS) deviation of the fluctuations from the average. As the procedure uses one million random combinations to generate the distributions, The statistical uncertainty from the actual random generations is negligible compared to the uncertainty from measuring the templates.

11.3 VALIDATION

The validity of the background estimation technique can be evaluated in both data and simulation. The underlying assumption that random combinations of dE/dx and momentum can predict a mass distribution in an orthogonal region can be tested using simulated samples where concerns like multiple particle types can be controlled. Using the same technique in another set of signal-depleted regions in data then extends this confidence to the more complicated case where several particle species are inherently included.

11.3.1 CLOSURE IN SIMULATION

The first test of the procedure is done using a simulated sample of $W \to \mu\nu$ decays. These types of events provide the ingredients required to test the background estimate, E_T^{miss} and isolated tracks, with high statistics. In this example there is no signal, so simulated events in the orthogonal CRs are used to estimate the shape of the mass distribution of the simulated events in the signal region. To reflect the different topology for W boson decays, the CRs use slightly modified definitions. In all CRs, the requirement of $p > 150$ GeV and the SM rejection requirements are removed. Additionally, for the signal region the requirement on E_T^{miss} is relaxed to 30 GeV and the corresponding inverted requirement on CR2 is also set at 30 GeV.

With these modified selections, the simulated and randomly generated distributions of $M_{dE/dx}$ are shown in Figure 84. This figure includes the mass distributions before and after the requirement on dE/dx, which significantly shapes the distributions. In both cases the background estimation technique reproduces the shape of $M_{dE/dx}$ in the signal region. There is a small difference in the positive tail of the mass distribution prior to the ionization cut, where the random events underestimate the fraction of tracks with mass above 150 GeV by about 20%. After the ionization requirement, however, this discrepancy is not present and the two distributions agree to within statistical uncertainties.

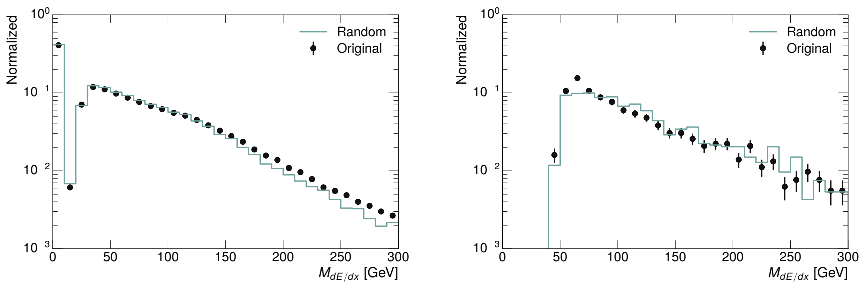

(a) (b)

Figure 84: The distribution of $M_{dE/dx}$ (a) before and (b) after the ionization requirement for tracks in simulated W boson decays and for the randomly generated background estimate.

This ability to reproduce the shape of the mass distribution in simulated events shows that the technique works as expected. No significant biases are acquired in using low dE/dx events to select kinematic templates or in using low E_T^{miss} events to select ionization templates, as either would result in a mismodeling of the shape of the mass distribution. The simulated events contain only one particle type, however, so this test only establishes that the technique works well when the the CRs are populated by exactly the same species.

11.3.2 VALIDATION REGION IN DATA

The second test of the background estimate is performed using data in an orthogonal validation region. The validation region, and the corresponding CRs, are formed using the same selection requirements as in the nominal method but with a modified requirement on momentum, $50 < p[\text{GeV}] < 150$. This allows the technique to be checked in a region with very similar properties but where the signal is depleted, as the majority of the signal has momentum above 150 GeV while the backgrounds are enhanced below that threshold. Any biases on the particle composition of the CRs for the signal region will be reflected in the CRs used to estimate the mass distribution in the validation region.

Figure 85 shows the measured and randomly generated mass distributions for data before and after the ionization requirement. The background estimate does an excellent job of modeling the actual background before the ionization requirement, with good agreement to within the statistical uncertainties out to the limit of the mass distribution. There are very few events in the validation region after the ionization requirement, but the few observed events are consistent with the background prediction. The good agreement in this validation region provides a confirmation that the technique works even in the full-complexity case with multiple particle types entering the distributions. Any bias from changes in particle composition between regions is small compared to statistical uncertainties.

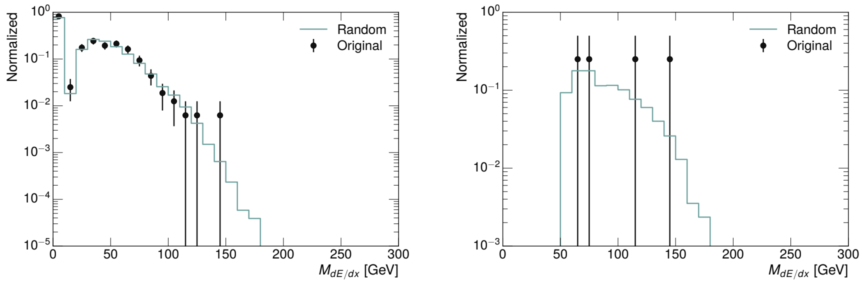

(a) (b)

Figure 85: The distribution of $M_{dE/dx}$ (a) before and (b) after the ionization requirement for tracks in the validation region and for the randomly generated background estimate.

12

SYSTEMATIC UNCERTAINTIES

A number of systematic uncertainties affect the interpretation of the results of the search. These uncertainties can broken down into two major categories, those which affect the estimate of the background using data and those which affect the measurement of the signal yield estimated with simulated events. The total measured systematic uncertainties are 7% for the background estimation and approximately 32% for the signal yield depending on lifetime. These systematic uncertainties are expected to be small compared to the statistical fluctuations of the measured yields so that measured cross-sectional limits will be dominated by statistical uncertainties. The following sections describe each source of systematic uncertainty for each of the two types.

12.1 BACKGROUND ESTIMATE

The systematic uncertainties on the background estimate come primarily from considering alternative methods for generating the background distributions. These uncertainties are small compared to the statistical uncertainties on the background estimate which come from the limited statistics in measuring the template distributions, as described in Section 11.2. They are summarized in Table 10.

Source of Uncertainty:	Value [%]
Analytic Description of dE/dx	4.0
Muon Fraction (Stable Region only)	3.0
IBL Ionization Correction	3.8
Normalization	3.0
Total (Metastable Region):	6.3
Total (Stable Region):	7.0

Table 10: A summary of the sources of systematic uncertainty for the data-driven background in the signal region. If the uncertainty depends on the mass, the maximum values are reported.

12.1.1 ANALYTIC DESCRIPTION OF DE/DX

The background estimate uses a binned template distribution to estimate the dE/dx of tracks in the signal region, as described in Section 11.2. It is also possible to fit that measured distribution to a functional form to help smooth the distribution in the tails of dE/dx where the template is driven by a small number of tracks. Both Landau convolved with a Gaussian and Crystal Ball functions are considered as the functional form and used to re-estimate the background distribution. The deviations compared to the nominal method are found to be 4%, and this is taken as a systematic uncertainty to cover the inability carefully predict the contribution from the long tail of dE/dx where there are few measurements available in data.

12.1.2 MUON FRACTION

The stable region of the analysis explicitly includes tracks identified as muons, which have a known difference in their dE/dx distributions compared to non-muon tracks (Section 11.1). To account for a difference in muon fraction between the background region and the signal region for this selection, the dE/dx templates for muons and non-muons are measured separately and then the relative fraction of each is varied in the random generation. The muon fraction is varied by its statistical uncertainty and the resulting difference of 3% in background yield is taken as the systematic uncertainty.

12.1.3 IBL CORRECTIONS

The IBL, described in Section 5.3.1, received a significant dose of radiation during the data collection in 2015. The irradiation can cause a drift in the frontend electronics and thus alter the dE/dx measurement which includes the ToT output by the IBL. These effects are corrected for in the nominal analysis by scaling the dE/dx measurements by a constant factor derived for each run to match the average dE/dx value to a reference run where the IBL was known to be stable to this effect. However, this corrective factor does not account for inter-run variations. To account for this potential drift of dE/dx, the correction procedure is repeated by varying the corrections up and down by the maximal run-to-run variation from the full data-taking period, which results in an uncertainty of 3.8%.

12.1.4 NORMALIZATION

As described in Section 11.2, the generated distribution of masses is normalized in a shoulder region ($M < 160$ GeV) where signals have been excluded by previous analyses. That normalization factor is varied by its statistical uncertainty and the resulting fluctuation in the mass distribution of 3% is taken as a systematic uncertainty on the background estimate.

12.2 SIGNAL YIELD

The systematic uncertainties on the signal yield can be divided into three categories; those on the simulation process, those on the modeling of the detector efficiency or calibration, and those affecting the overall signal yield. They are summarized in Table 10. The largest uncertainty comes from the uncertainty on the production cross section for gluinos, which is the dominant systematic uncertainty in this analysis.

Source of Uncertainty	−[%]	+[%]
ISR Modeling (Metastable Region)	1.5	1.5
ISR Modeling (Stable Region)	14	14
Pile-up Reweighting	1.1	1.1
Trigger Efficiency Reweighting	0.9	0.9
E_T^{miss} Scale	1.1	2.2
Ionization Parametrization	7.1	0
Momentum Parametrization	0.3	0.0
Electron Rejection	0.0	0.0
Hadron Rejection	0.0	0.0
μ Identification	4.3	4.3
Luminosity	5	5
Signal size uncertainty	28	28
Total (Metastable Region)	30	29
Total (Stable Region)	33	32

Table 11: A summary of the sources of systematic uncertainty for the simulated signal yield. The uncertainty depends on the mass and lifetime, and the maximum negative and positive values are reported in the table.

12.2.1 ISR MODELING

As discussed in Section 9.2, `MadGraph` is expected to reproduce the distribution of ISR in signal events more accurately than the nominal `Pythia` samples. The analysis reweights the distribution of ISR in the simulated signal events to match the distribution found in generated `MadGraph` samples. This has an effect on the selection efficiency in the signal samples, where ISR contributes to the generation of E_T^{miss}. To account for the potential inaccuracy on the simulation of ISR at high energies, half of the difference between the signal efficiency with the reweighted distribution and the original distribution is taken as a systematic uncertainty.

12.2.2 PILEUP REWEIGHTING

The simulated events were generated prior to data collection with an estimate of the average number of interactions per bunch crossing. This estimate does not match the value of pileup during actual data collection, but a large fraction of the simulated events would be discarded in order to match the distribution in data.

Therefore the simulated signal events are not reweighted for pileup by default in the analysis. The effect of the pileup on signal efficiency is not expected to depend on the mass or lifetime of the generated signal events, which allows all of the generated signal events to be used together to assess the pileup dependence. To account for the potential effect of the difference in the number of interactions per bunch crossing between data and simulation, the difference in yield between the nominal signal events and the reweighted events averaged over all masses and lifetimes is taken as a systematic uncertainty on the yield for each mass and lifetime (1.1%).

12.2.3 TRIGGER EFFICIENCY REWEIGHTING

As described in Section 10.2, the selection for this analysis does not require a sufficiently large value of E_T^{miss} to be above the plateau of trigger efficiency. Therefore, some signal events which would otherwise pass the event selection can be excluded because of the trigger requirement. These effects can be difficult to estimate in simulation, and thus are constrained by comparing data and simulated events in an alternative W boson region which uses decays to muons to find a relatively pure sample of events with missing energy. The trigger efficiency for data and simulated W events are shown in Figure 86. The comparison between data and MC in this region constrains the simulation of the trigger efficiency. The simulated signal events are reweighted by the ratio of data to simulation in the W boson decays, while the difference between the data and simulation in those decays is taken as a systematic uncertainty. This results in an uncertainty of only 0.9% as the majority of events are well above the plateau and the disagreement between data and simulation is small even below that plateau.

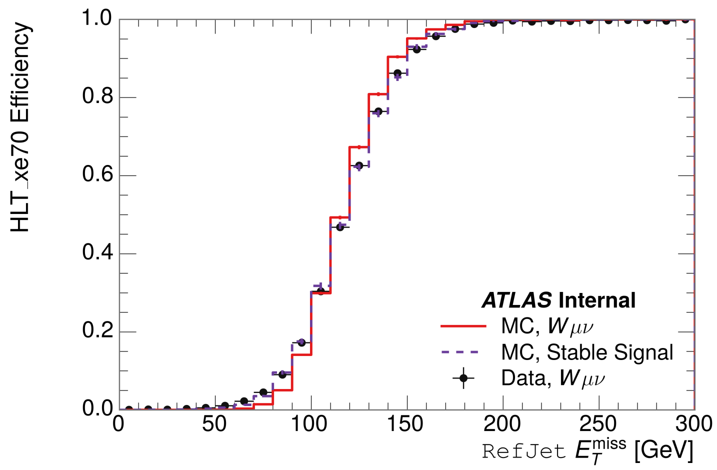

Figure 86: The trigger efficiency for the `HLT_xe70` trigger requirement as a function of Calorimeter E_T^{miss} for simulated data events with a W boson selection. Simulated signal events and simulated W boson events are also included.

Systematic Variation	−[%]	+[%]
JET_GroupedNP_1	−0.7	1.3
JET_GroupedNP_2	−0.7	1.2
JET_GroupedNP_3	−0.5	1.3

Table 12: Example of the contributing systematic variations to the total systematic for the E_T^{miss} Scale, as measured in a 1200 GeV, Stable R-Hadron signal sample.

12.2.4 MISSING TRANSVERSE MOMENTUM SCALE

The ATLAS Combined Performance (CP) group provides a default recommendation for systematic variations of jets and missing energy (**note: I'm not quite sure what to cite for this - I don't see any papers from the jet/met group after this was implemented**). These variations enter into this analysis only in the requirement on E_T^{miss}. The effect of the measured scale of E_T^{miss} is evaluated by varying the E_T^{miss} scale according to the one sigma variations provided by all CP recommendations on objects affecting event kinematics in simulated signal events. Missing energy is reconstructed from fully reconstructed objects so any systematic uncertainties affecting jets, muons, electrons, or the E_T^{miss} soft terms are included. The only non-negligible contributions found using this method are itemized in Table 12 for an example signal sample (1200 GeV, Stable R-Hadron), where the systematic is measured as the relative difference in the final signal efficiency after applying the associated variation through the CP tools. The only variations that are significant are the grouped jet systematic variations, which combine recommended jet systematic uncertainties into linearly independent variations.

As the peak of the reconstructed E_T^{miss} distribution in the signal is significantly above the current threshold for events which pass the trigger requirement, the effect of scale variation is expected to be small, which is consistent with the measured systematic of approximately 2%. Events which do not pass the trigger requirement usually fail because there are no ISR jets in the event to balance the R-hadrons' transverse momentum, so the reconstructed E_T^{miss} is low and therefore also expected to be not very sensitive to scale changes.

12.2.5 MOMENTUM PARAMETRIZATION

The uncertainty on the signal efficiency from track momentum is calculated using the CP group recommendations for tracks. In particular, only one recommended systematic variation affects track momentum, the sagitta bias for q/P. This uncertainty is propagated to the final selection efficiency by varying the track momentum by the recommended one sigma variation, and the associated uncertainty is found to be negligible (0.3%).

12.2.6 IONIZATION REQUIREMENT

The dE/dx distributions in data and simulated events have different most probable values, which is due in part to radiation effects in the detector that are not fully accounted for in the simulation. The difference does not affect the mass measurement used in this analysis, as independent calibrations are done in simulation and in data. However, it does affect the efficiency of the high dE/dx selection requirement. To calculate the size of the effect on the signal efficiency, the dE/dx distribution in signal simulation is scaled by a scale factor obtained from comparing the dE/dx distribution of inclusive tracks in data and in simulation. The difference in efficiency for this sample with a scaled dE/dx distribution, relative to the nominal case, is taken as a systematic uncertainty on signal efficiency. The uncertainty is as large as 7% for low masses and falls to a negligible effect for large masses.

12.2.7 ELECTRON AND JET REJECTION

The systematic uncertainty on the electron rejection is measured by varying the EM fraction requirement significantly, from 0.95 to 0.9. This is found to have a less than 0.04% effect on signal acceptance, on average, and so is completely negligible. Similarly, the uncertainty on jet rejection is measured by tightening the E/p requirement from 0.5 to 0.4. This is found to have no effect on signal acceptance, so again the systematic is again negligible.

12.2.8 MUON VETO

The metastable signal region requires that the candidate tracks are not identified as medium muons because the majority of R-Hadrons in the lifetime range included in that region do not reach the muon spectrometers before they decay. However, the exponential tail of the R-Hadron lifetime distribution results in some R-Hadrons traversing the muon spectrometer. These can still fail the muon medium identification because they can fail on the requirement on the number of precision hits required to pass the loose selection because they arrive late to the muon spectrometer. This can be seen in Figure 87, which shows the efficiency of the muon veto as a function of $1/\beta$, for two simulated stable R-Hadron samples.

Thus, the efficiency of the muon veto depends on the timing resolution of the spectrometer, so an uncertainty is applied to the signal efficiency to cover differences in timing resolution between data and simulation. First, a sample of $Z \to \mu\mu$ events is selected in data in which one of the muons has a late arrival time measured in the MDT. Then the reconstructed β distribution is compared to the distribution in simulated $Z \to \mu\mu$ events; the difference between these two distributions reflects the difference in timing resolution between data and simulation. To emulate this difference in simulated signal events, the magnitude of the difference is used to scale and shift the true β distribution of R-Hadrons in simulation. Signal events are then reweighted based on this varied β distribution,

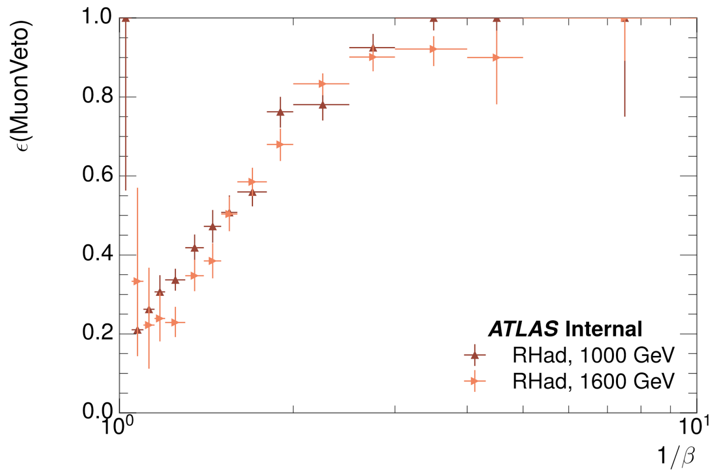

Figure 87: The efficiency of the muon veto for R-hadrons of two different masses, as a function of $\frac{1}{\beta}$ for simulated R-Hadron tracks.

and the difference in the efficiency of the muon veto selection is compared with the nominal and reweighted true β distributions. The difference in muon veto efficiency is taken as a systematic uncertainty of the muon veto.

The comparison of reconstructed β between data and simulation is performed separately in the barrel, transition, and endcap regions of the spectrometer, and the reweighting of the true β distribution in signal is done per region. The comparison of average reconstructed MDT β between data and simulation for the barrel region is shown in Figure 88 for $Z \rightarrow \mu\mu$ events. As expected, The uncertainty is found to be negligible for R-hadrons with short lifetimes, and is only significant for lifetimes above 30 ns.

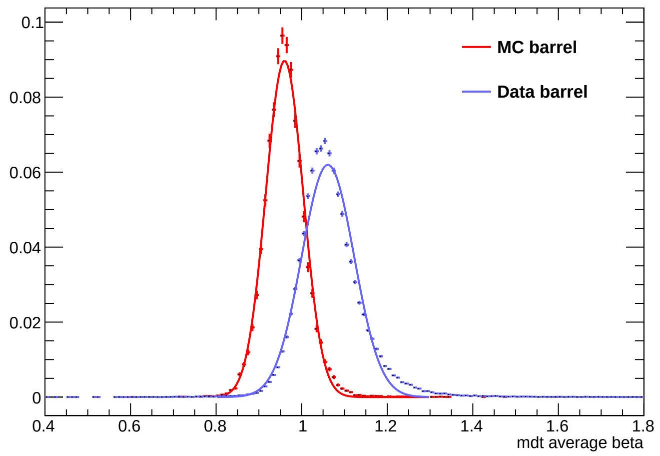

Figure 88: The average reconstructed MDT β distribution for $Z \rightarrow \mu\mu$ events in which one of the muons is reconstructed as a slow muon, for both data and simulation. A gaussian fit is superimposed.

12.2.9 LUMINOSITY

The luminosity uncertainty is provided by a luminosity measurement on ATLAS and was measured to be 5% at the time of the publication of this analysis.

12.2.10 SIGNAL SIZE

As discussed in Section 9.2, the signal cross sections are calculated at NLO in the strong coupling constant with a resummation of soft-gluon emission at NLL. The uncertainties on those cross sections are between 14% to 28% for the R-Hadrons in the range of 400 to 1800 GeV [95, 96], where the uncertainty increases with the mass.

13

RESULTS

This full analysis was performed using the 3.2 fb^{-1} from the 2015 data-taking. Using the selections discussed in Chapter 10, sixteen events were observed in the stable signal region and eleven events were observed in the metastable signal region, prior to requirements on the candidate track mass. The background estimate discussed in Chapter 11 predicts $17 \pm 2.6(\text{stat}) \pm 1.2(\text{syst})$ events for the stable region and $11.1 \pm 1.7(\text{stat}) \pm 0.7(\text{syst})$ events for the metastable region. These counts are summarized in Table 13.

The mass estimated using dE/dx (Section 10.4.1) provides the final discriminating variable, where the signal would be expected as an excess in the falling exponential tail of the expected background. The observed distribution of masses is shown in Figure 89, along with the predicted distribution from the background estimate for each signal region. Both include a few example simulated signal distributions, which show the scale of an excess were the R-Hadron signals present. Their is no statistically significant evidence of an excess in the data over the background estimation. From this distribution it is clearly possible to rule out signals with lower masses, around 1200 GeV, which have larger cross sections.

13.1 CROSS SECTIONAL LIMITS

Because there is no observed significant excess of events in the signal region, this analysis sets upper limits on the allowed cross section for R-Hadron production. These limits are set for each mass point by counting the observed events in data, along with the expected background and simulated signal events, in windows of mass. The mass windows are formed by fitting the distribution of signal events to a Gaussian distribution, and the window is then $\pm 1.4\sigma$ around the center of that Gaussian. Two examples of the windows formed by this procedure are shown in Tables 14-15, for the stable and 10 ns working points. The corresponding counts of observed data, expected background, and simulated signal for those same working points are shown in Tables 16-17. Appendix B includes the mass windows and counts for all of the considered signal points.

Selection Region	Expected Background	Data
Stable	$17.2 \pm 2.6 \pm 1.2$	16
Metastable	$11.1 \pm 1.7 \pm 0.7$	11

Table 13: The estimated number of background events and the number of observed events in data for the specified selection regions prior to the requirement on mass. The background estimates show statistical and systematic uncertainties.

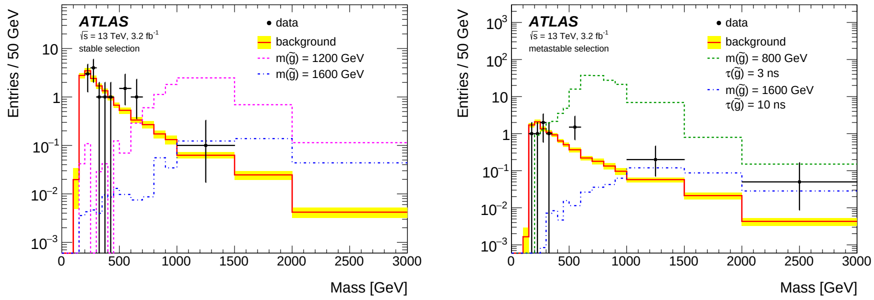

Figure 89: The observed mass distribution of events in data and the generated background distribution in (a) the stable and (b) the metastable signal region. A few example simulated signal distributions are superimposed.

$m(\tilde{g})$ [GeV]	Left Extremum [GeV]	Right Extremum [GeV]
1000	655	1349
1100	734	1455
1200	712	1631
1300	792	1737
1400	717	1926
1500	815	2117
1600	824	2122
1700	900	2274
1800	919	2344

Table 14: The left and right extremum of the mass window for each generated mass point with a 10 ns lifetime.

$m(\tilde{g})$ [GeV]	Left Extremum [GeV]	Right Extremum [GeV]
800	627	1053
1000	726	1277
1200	857	1584
1400	924	1937
1600	993	2308
1800	1004	2554

Table 15: The left and right extremum of the mass window used for each generated stable mass point.

$m(\tilde{g})$ [GeV]	Expected Signal	Expected Background	Observed Data
800	462.83 ± 14.86	1.764 ± 0.080	2.0
1000	108.73 ± 3.38	1.458 ± 0.070	1.0
1200	31.74 ± 0.95	1.137 ± 0.060	1.0
1400	10.22 ± 0.29	1.058 ± 0.058	1.0
1600	3.07 ± 0.09	0.947 ± 0.054	1.0
1800	1.08 ± 0.05	0.940 ± 0.054	1.0

Table 16: The expected number of signal events, the expected number of background events, and the observed number of events in data with their respective statistical errors within the respective mass window for each generated stable mass point

$m(\tilde{g})$ [GeV]	Expected Signal	Expected Background	Observed Data
1000	144.48 ± 5.14	1.499 ± 0.069	2.0
1100	73.19 ± 2.61	1.260 ± 0.060	2.0
1200	41.54 ± 1.41	1.456 ± 0.067	2.0
1300	22.58 ± 0.77	1.201 ± 0.058	2.0
1400	12.70 ± 0.42	1.558 ± 0.071	2.0
1500	6.73 ± 0.24	1.237 ± 0.060	2.0
1600	3.90 ± 0.13	1.201 ± 0.058	2.0
1700	2.27 ± 0.07	1.027 ± 0.052	2.0
1800	1.34 ± 0.04	1.019 ± 0.052	2.0

Table 17: The expected number of signal events, the expected number of background events, and the observed number of events in data with their respective statistical errors within the respective mass window for each generated mass point with a lifetime of 10 ns.

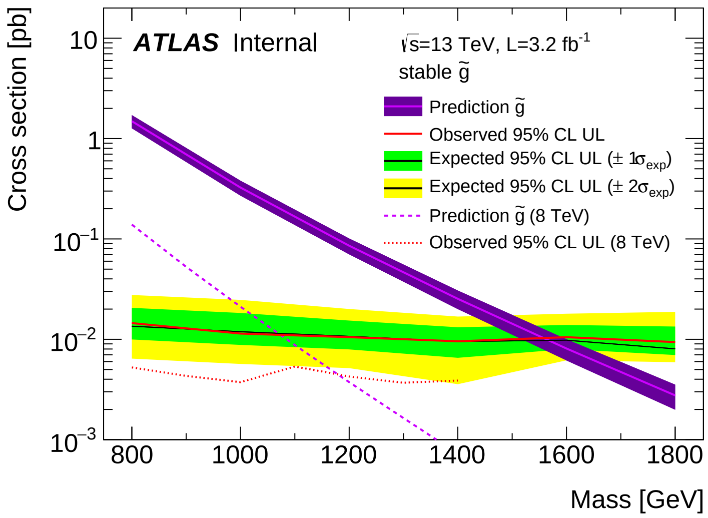

Figure 90: The observed and expected cross section limits as a function of mass for the stable simulated signal. The predicted cross section values for the corresponding signals are included.

The 95% confidence level upper limits on the cross sections for a large grid of masses (between 800 and 1800 GeV) and lifetimes (between 0.4 and stable) are extracted from these counts with the CL_S method using the profile likelihood ratio as a test statistic [100]. For this procedure, the systematic uncertainties estimated for the signal and background yields are treated as Gaussian-distributed nuissance parameters. The uncertainty on the normalization of the expected background distribution is included in the expected background events. At this point the expected cross section limit is calculated for both the metastable and stable signal region for each lifetime point, and the region with the best expected limit is selected for each lifetime. Using that procedure, the metastable region is used for lifetimes up to and including 30 ns, and the stable region for lifetimes above it.

The resulting cross-sectional upper limits are shown as a function of mass in Figure 90 and Figure 91 for each lifetime considered. The limits are interpolated linearly between each mass point, and the dependence of the limit on the mass is small as the efficiency is relatively constant for large R-Hadron masses. There is however a strong dependence on lifetime, as discussed in Section 10.5, where the probability to form a fully reconstructed track and the kinematic freedom to produce E_T^{miss} result in a local maximum in the limit at 10-30 ns. The figures also include the expected cross section for pair-produced gluino R-Hadrons for reference. For the 10 ns and stable cross section limits, both the observed limit and expected cross section for the Run 1, 8 TeV version of this analysis are included. There the cross sectional limits are lower because of the increased available luminosity, while the signal cross sections were also much lower because of the lower collision energy.

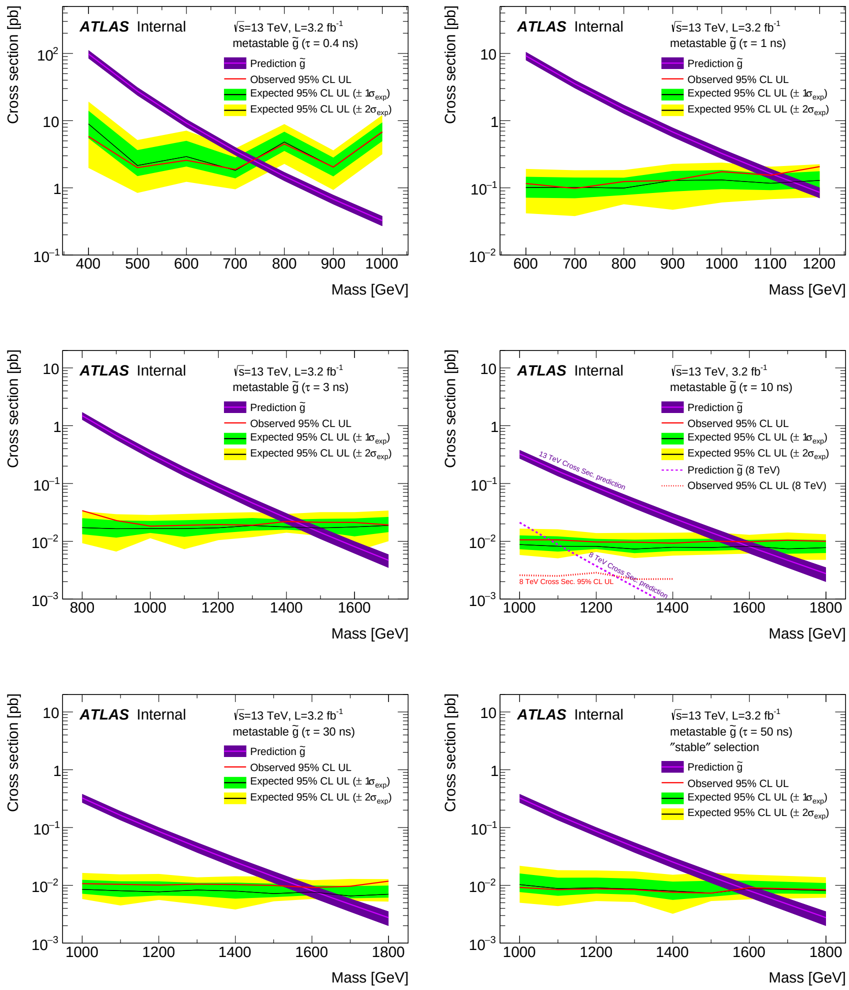

Figure 91: The observed and expected cross section limits as a function of mass for each generated lifetime. The predicted cross section values for the corresponding signals are included.

13.2 MASS LIMITS

The cross-sectional limits can then be used to derive a lower mass limit for gluino R-Hadrons by comparing them to the theoretically predicted production cross sections. These mass limits range from only 740 GeV at the lowest lifetimes considered, where the selection efficiency is very low, to up to 1580 GeV at 30 ns where the selection efficiency is maximized. The observed and expected mass limits for each lifetime point are detailed in Table 18, which also lists which selection region was used for each lifetime. These excluded range of masses as a function of lifetime is also shown in Figure 92. The Run 1 limits are included for comparison; the limits have increased by about 200 GeV on average. The search has also improved since the previous incarnation from Run 1 in optimizing the region between 30 GeV and detector-stable lifetimes by introducing the second signal region. The definition of the stable region prevents the significant drop in mass limit that occurred above 30 GeV in the Run 1 analysis.

Selection	τ [ns]	M_{obs} >[GeV]	M_{exp} >[GeV]
Metastable	0.4	740	730
”	1.0	1110	1150
”	3.0	1430	1470
”	10	1570	1600
”	30	1580	1620
Stable	50	1590	1590
”	stable	1570	1580

Table 18: The observed and expected 95% CL lower limit on mass for gluino R-Hadrons for each considered lifetime.

13.3 CONTEXT FOR LONG-LIVED SEARCHES

This search plays an important role in the current, combined ATLAS search for long lived particles. The mass limits provided by various ATLAS searches for long-lived gluino R-Hadrons can be seen in Figure 93. This search provides the most competitive limit for lifetimes between 3 ns up through very long lifetimes, where it is still competitive with dedicated searches for stable particles. The limits placed on gluino production are very similar to the limits on promptly decaying models.

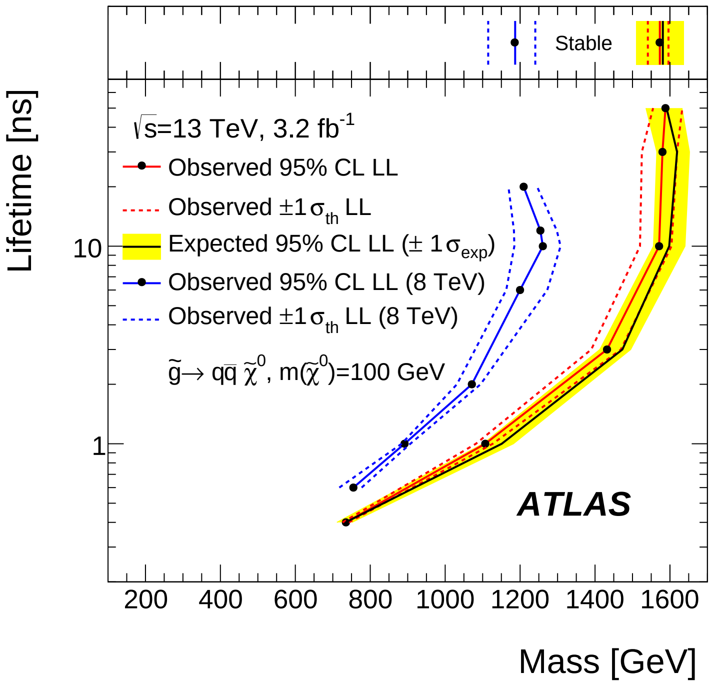

Figure 92: The excluded range of masses as a function of gluino lifetime. The expected lower limit (LL), with its experimental $\pm 1\sigma$ band, is given with respect to the nominal theoretical cross-section. The observed 95% LL obtained at $\sqrt{s}$ = 8 TeV [83] is also shown for comparison.

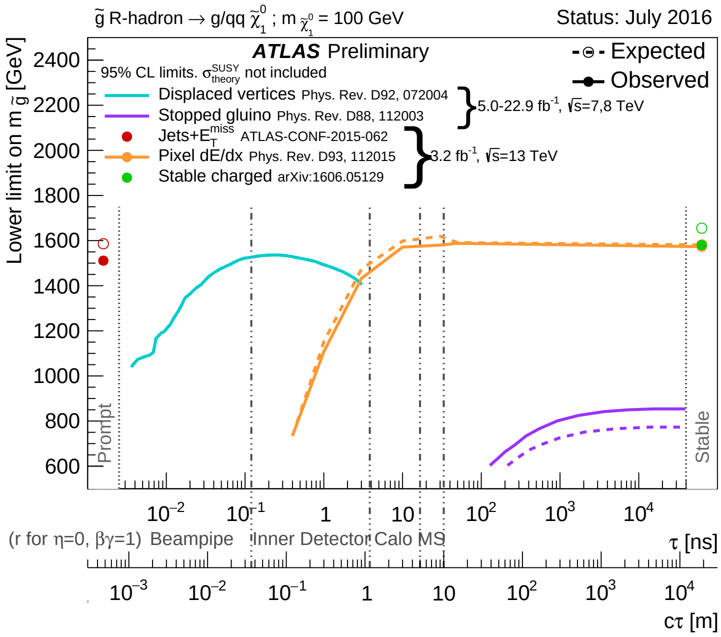

Figure 93: The constraints on the gluino mass as a function of lifetime for a split-supersymmetry model with the gluino R-Hadrons decaying into a gluon or light quarks and a neutralino with mass of 100 GeV. The solid lines indicate the observed limits, while the dashed lines indicate the expected limits. The area below the curves is excluded. The dots represent results for which the particle is assumed to be prompt or stable.

14 SUMMARY AND OUTLOOK

The search described herein targetted the unique signature of TeV-scale, charged LLPs, which are predicted in a variety of extensions to the SM including some versions of SUSY. The dataset of 13 TeV proton-proton collisions was collected during 2015 by the ATLAS detector at the LHC, with an integrated luminosity of 3.2 fb^{-1}. The specific search strategy focused on identifying massive, charged particles which propagate through the Pixel detector in ATLAS by their characteristically large ionization. Recent updates to the strategy also include a number of rejection techniques that significantly reduce SM backgrounds compared to previous iterations. The analysis also provided a data-driven background estimation method that was shown to be effective with validation tests in both simulation and actual data.

No significant excesses above the background prediction were found in the data, and so limits were placed on the production of massive, charged, LLPs. Using a benchmark model of simulated R-Hadrons, cross sections above 10-100 fb were excluded at 95% confidence level, depending on the lifetime of the R-Hadron. Together with the predicted gluino pair-production cross sections, these lead to mass limits on R-Hadrons up to 1600 GeV where the search is most sensitive. Though these specific values assume an R-Hadron LLP, the search strategy accomodates a number of other species and the limits can be interpreted for other models. The search provides a significant contribution to the combined efforts to search for LLPs in SUSY, as the current version places the largest mass limits for lifetimes starting at 3 ns and up through very long lifetimes.

These results are expected to be significantly improved in the following years, primarily because of continuing data collection at 13 TeV at the LHC. During 2016, but after the release of this analysis, ATLAS recorded an additional 35.5 fb^{-1} of collisions, and analysis of this data would significantly extend the limits presented here. The next iteration of the analysis can also provide additional interpretations of the search, by explicitly including other models like stop R-Hadrons and charginos in the limit calculations, as has been done in previous searches [83]. This strategy will continue to provide a competitive approach to discovering new LLPs throughout the lifetime of the LHC.

PART V

APPENDIX

A

INELASTIC CROSS SECTION

B

EXPANDED R-HADRON YIELDS AND LIMITS

$m(\tilde{g})$ [GeV]	Left Extremum [GeV]	Right Extremum [GeV]
1000	682	1387
1100	763	1478
1200	801	1606
1300	809	1841
1400	861	2011
1500	920	2032
1600	952	2173
1800	1017	2422

Table 19: The left and right extremum of the mass window for each generated mass point with a 50 ns lifetime.

$m(\tilde{g})$ [GeV]	Left Extremum [GeV]	Right Extremum [GeV]
1000	689	1321
1100	746	1513
1200	788	1670
1300	860	1734
1400	833	1925
1500	852	2048
1600	833	2283
1700	946	2379
1800	869	2505

Table 20: The left and right extremum of the mass window for each generated mass point with a 30 ns lifetime.

$m(\tilde{g})$ [GeV]	Left Extremum [GeV]	Right Extremum [GeV]
1000	655	1349
1100	734	1455
1200	712	1631
1300	792	1737
1400	717	1926
1500	815	2117
1600	824	2122
1700	900	2274
1800	919	2344

Table 21: The left and right extremum of the mass window for each generated mass point with a 10 ns lifetime.

$m(\tilde{g})$ [GeV]	Left Extremum [GeV]	Right Extremum [GeV]
800	531	1065
900	576	1165
1000	610	1345
1100	635	1432
1200	663	1563
1300	620	1667
1400	742	1727
1500	761	1937
1600	573	2000
1700	621	2182

Table 22: The left and right extremum of the mass window used for each generated mass point with a lifetime of 3 ns.

$m(\tilde{g})$ [GeV]	Left Extremum [GeV]	Right Extremum [GeV]
600	411	758
700	385	876
800	486	970
900	406	987
1000	408	1136
1100	555	1196
1200	516	1378

Table 23: The left and right extremum of the mass window used for each mass point with a lifetime of 1 ns.

$m(\tilde{g})$ [GeV]	Left Extremum [GeV]	Right Extremum [GeV]
400	204	510
500	295	639
600	288	702
700	323	701
800	190	771
900	277	677
1000	249	688

Table 24: The left and right extremum of the mass window for each generated mass point with a lifetime of 0.4 ns.

$m(\tilde{g})$ [GeV]	Left Extremum [GeV]	Right Extremum [GeV]
800	627	1053
1000	726	1277
1200	857	1584
1400	924	1937
1600	993	2308
1800	1004	2554

Table 25: The left and right extremum of the mass window used for each generated stable mass point.

$m(\tilde{g})$ [GeV]	Expected Signal	Expected Background	Observed Data
1000	131.18 ± 6.35	1.803 ± 0.081	1.0 ± 1.0
1100	71.11 ± 3.35	1.409 ± 0.069	1.0 ± 1.0
1200	37.18 ± 1.75	1.310 ± 0.066	1.0 ± 1.0
1300	20.76 ± 0.95	1.431 ± 0.069	1.0 ± 1.0
1400	12.63 ± 0.57	1.273 ± 0.065	1.0 ± 1.0
1500	6.57 ± 0.29	1.115 ± 0.059	1.0 ± 1.0
1600	3.56 ± 0.16	1.041 ± 0.057	1.0 ± 1.0
1800	1.27 ± 0.05	0.918 ± 0.053	1.0 ± 1.0

Table 26: The expected number of signal events, the expected number of background events, and the observed number of events in data with their respective statistical errors within the respective mass window for each generated mass point with a lifetime of 50 ns.

$m(\tilde{g})$ [GeV]	Expected Signal	Expected Background	Observed Data
1000	144.65 ± 6.34	1.328 ± 0.063	2.0 ± 1.4
1100	75.28 ± 3.27	1.255 ± 0.060	2.0 ± 1.4
1200	40.51 ± 1.75	1.193 ± 0.058	2.0 ± 1.4
1300	20.91 ± 0.93	0.997 ± 0.051	2.0 ± 1.4
1400	11.97 ± 0.51	1.131 ± 0.056	2.0 ± 1.4
1500	6.81 ± 0.28	1.111 ± 0.055	2.0 ± 1.4
1600	4.19 ± 0.16	1.193 ± 0.058	2.0 ± 1.4
1700	2.42 ± 0.09	0.963 ± 0.050	2.0 ± 1.4
1800	1.46 ± 0.05	1.138 ± 0.056	3.0 ± 1.7

Table 27: The expected number of signal events, the expected number of background events, and the observed number of events in data with their respective statistical errors within the respective mass window for each generated mass point with a lifetime of 30 ns.

$m(\tilde{g})$ [GeV]	Expected Signal	Expected Background	Observed Data
1000	144.48 ± 5.14	1.499 ± 0.069	2.0 ± 1.4
1100	73.19 ± 2.61	1.260 ± 0.060	2.0 ± 1.4
1200	41.54 ± 1.41	1.456 ± 0.067	2.0 ± 1.4
1300	22.58 ± 0.77	1.201 ± 0.058	2.0 ± 1.4
1400	12.70 ± 0.42	1.558 ± 0.071	2.0 ± 1.4
1500	6.73 ± 0.24	1.237 ± 0.060	2.0 ± 1.4
1600	3.90 ± 0.13	1.201 ± 0.058	2.0 ± 1.4
1700	2.27 ± 0.07	1.027 ± 0.052	2.0 ± 1.4
1800	1.34 ± 0.04	1.019 ± 0.052	2.0 ± 1.4

Table 28: The expected number of signal events, the expected number of background events, and the observed number of events in data with their respective statistical errors within the respective mass window for each generated mass point with a lifetime of 10 ns.

$m(\tilde{g})$ [GeV]	Expected Signal	Expected Background	Observed Data
800	362.97 ± 14.68	1.841 ± 0.080	5.0 ± 2.2
900	169.20 ± 6.69	1.710 ± 0.076	3.0 ± 1.7
1000	84.78 ± 3.23	1.727 ± 0.076	2.0 ± 1.4
1100	40.06 ± 1.60	1.679 ± 0.075	2.0 ± 1.4
1200	20.06 ± 0.81	1.598 ± 0.072	2.0 ± 1.4
1300	10.76 ± 0.43	1.851 ± 0.080	2.0 ± 1.4
1400	5.52 ± 0.22	1.374 ± 0.064	2.0 ± 1.4
1500	3.16 ± 0.13	1.355 ± 0.064	2.0 ± 1.4
1600	2.13 ± 0.11	2.235 ± 0.093	3.0 ± 1.7
1700	1.10 ± 0.06	1.995 ± 0.085	2.0 ± 1.4

Table 29: The expected number of signal events, the expected number of background events, and the observed number of events in data with their respective statistical errors within the respective mass window for each generated mass point with a lifetime of 3 ns.

$m(\tilde{g})$ [GeV]	Expected Signal	Expected Background	Observed Data
600	431.80 ± 36.60	2.418 ± 0.099	3.0 ± 1.7
700	192.77 ± 15.28	3.267 ± 0.126	3.0 ± 1.7
800	69.63 ± 5.90	2.125 ± 0.089	3.0 ± 1.7
900	28.91 ± 2.59	3.114 ± 0.121	3.0 ± 1.7
1000	13.64 ± 1.22	3.359 ± 0.129	5.0 ± 2.2
1100	6.13 ± 0.57	1.879 ± 0.081	3.0 ± 1.7
1200	3.24 ± 0.30	2.387 ± 0.098	5.0 ± 2.2

Table 30: The expected number of signal events, the expected number of background events, and the observed number of events in data with their respective statistical errors within the respective mass window for each generated mass point with a lifetime of 1 ns.

$m(\tilde{g})$ [GeV]	Expected Signal	Expected Background	Observed Data
400	181.71 ± 75.59	6.780 ± 0.238	4.0 ± 2.0
500	103.88 ± 30.05	4.310 ± 0.160	4.0 ± 2.0
600	28.34 ± 9.34	4.868 ± 0.177	4.0 ± 2.0
700	13.62 ± 4.00	3.908 ± 0.147	4.0 ± 2.0
800	2.75 ± 1.15	9.001 ± 0.308	8.0 ± 2.8
900	2.25 ± 0.71	5.045 ± 0.183	5.0 ± 2.2
1000	0.34 ± 0.19	6.026 ± 0.214	6.0 ± 2.4

Table 31: The expected number of signal events, the expected number of background events, and the observed number of events in data with their respective statistical errors within the respective mass window for each generated mass point with a lifetime of p4 ns.

$m(\tilde{g})$ [GeV]	Expected Signal	Expected Background	Observed Data
800	462.83 ± 14.86	1.764 ± 0.080	2.0 ± 1.4
1000	108.73 ± 3.38	1.458 ± 0.070	1.0 ± 1.0
1200	31.74 ± 0.95	1.137 ± 0.060	1.0 ± 1.0
1400	10.22 ± 0.29	1.058 ± 0.058	1.0 ± 1.0
1600	3.07 ± 0.09	0.947 ± 0.054	1.0 ± 1.0
1800	1.08 ± 0.05	0.940 ± 0.054	1.0 ± 1.0

Table 32: The expected number of signal events, the expected number of background events, and the observed number of events in data with their respective statistical errors within the respective mass window for each generated stable mass point

BIBLIOGRAPHY

[1] A. D. Martin, W. J. Stirling, R. S. Thorne, and G. Watt. “Parton distributions for the LHC”. In: *Eur. Phys. J.* C63 (2009), pp. 189–285. DOI: 10.1140/epjc/s10052-009-1072-5. arXiv: 0901.0002 [hep-ph].

[2] Nobelprize.org. “The 2004 Nobel Prize in Physics - Popular Information”. 2014. URL: https://cds.cern.ch/record/1165534.

[3] Prajwal Raj Kafle, Sanjib Sharma, Geraint F. Lewis, and Joss Bland-Hawthorn. “On the Shoulders of Giants: Properties of the Stellar Halo and the Milky Way Mass Distribution”. In: *Astrophys. J.* 794.1 (2014), p. 59. DOI: 10.1088/0004-637X/794/1/59. arXiv: 1408.1787 [astro-ph.GA].

[4] Savas Dimopoulos and Howard Georgi. “Softly broken supersymmetry and SU(5)”. In: *Nuclear Physics B* 193.1 (1981), pp. 150 –162. ISSN: 0550-3213. DOI: http://dx.doi.org/10.1016/0550-3213(81)90522-8.

[5] A. Djouadi et al. “The Minimal supersymmetric standard model: Group summary report”. In: *GDR (Groupement De Recherche) - Supersymetrie Montpellier, France, April 15-17, 1998.* 1998. arXiv: hep-ph/9901246 [hep-ph]. URL: https://inspirehep.net/record/481987/files/arXiv:hep-ph_9901246.pdf.

[6] K. A. Olive et al. “Review of Particle Physics”. In: *Chin. Phys.* C38 (2014), p. 090001. DOI: 10.1088/1674-1137/38/9/090001.

[7] Lawrence J. Hall, Yasunori Nomura, and Satoshi Shirai. “Spread Supersymmetry with Wino LSP: Gluino and Dark Matter Signals”. In: *JHEP* 01 (2013), p. 036. DOI: 10.1007/JHEP01(2013)036. arXiv: 1210.2395 [hep-ph].

[8] G. F. Giudice and A. Romanino. “Split supersymmetry”. In: *Nucl. Phys. B* 699 (2004), p. 65. DOI: 10.1016/j.nuclphysb.2004.11.048. arXiv: hep-ph/0406088.

[9] N. Arkani-Hamed, S. Dimopoulos, G. F. Giudice, and A. Romanino. “Aspects of split supersymmetry”. In: *Nucl. Phys. B* 709 (2005), p. 3. DOI: 10.1016/j.nuclphysb.2004.12.026. arXiv: hep-ph/0409232.

[10] Lyndon Evans and Philip Bryant. “LHC Machine”. In: *JINST* 3 (2008), S08001. DOI: 10.1088/1748-0221/3/08/S08001.

[11] C Lefevre. “LHC: the guide (English version). Guide du LHC (version anglaise)”. 2009. URL: https://cds.cern.ch/record/1165534.

[12] “LEP Design Report Vol.1”. In: (1983).

[13] ATLAS Collaboration. “The ATLAS Experiment at the CERN Large Hadron Collider”. In: *JINST* 3 (2008), S08003. DOI: 10.1088/1748-0221/3/08/S08003.

[14] S. Chatrchyan et al. "The CMS experiment at the CERN LHC". In: *JINST* 3 (2008), S08004. DOI: 10.1088/1748-0221/3/08/S08004.

[15] A. Augusto Alves Jr. et al. "The LHCb Detector at the LHC". In: *JINST* 3 (2008), S08005. DOI: 10.1088/1748-0221/3/08/S08005.

[16] K. Aamodt et al. "The ALICE experiment at the CERN LHC". In: *JINST* 3 (2008), S08002. DOI: 10.1088/1748-0221/3/08/S08002.

[17] Daniel Froidevaux and Paris Sphicas. "General-Purpose Detectors for the Large Hadron Collider". In: *Annual Review of Nuclear and Particle Science* 56.1 (2006), pp. 375–440. DOI: 10.1146/annurev.nucl.54.070103.181209. URL: http://dx.doi.org/10.1146/annurev.nucl.54.070103.181209.

[18] M Capeans, G Darbo, K Einsweiller, M Elsing, T Flick, M Garcia-Sciveres, C Gemme, H Pernegger, O Rohne, and R Vuillermet. *ATLAS Insertable B-Layer Technical Design Report*. Tech. rep. CERN-LHCC-2010-013. ATLAS-TDR-19. 2010. URL: https://cds.cern.ch/record/1291633.

[19] T. Cornelissen, M. Elsing, S. Fleischmann, W. Liebig, and E. Moyse. "Concepts, Design and Implementation of the ATLAS New Tracking (NEWT)". In: (2007). Ed. by A. Salzburger.

[20] "Performance of the ATLAS Inner Detector Track and Vertex Reconstruction in the High Pile-Up LHC Environment". In: (2012).

[21] A. Salzburger. "The ATLAS Track Extrapolation Package". In: (2007).

[22] ATLAS Collaboration. "A neural network clustering algorithm for the ATLAS silicon pixel detector". In: *JINST* 9 (2014), P09009. DOI: 10.1088/1748-0221/9/09/P09009. arXiv: 1406.7690 [hep-ex].

[23] ATLAS Collaboration. *Performance of primary vertex reconstruction in proton–proton collisions at $\sqrt{s} = 7$ TeV in the ATLAS experiment*. ATLAS-CONF-2010-069. 2010. URL: https://cds.cern.ch/record/1281344.

[24] ATLAS Collaboration. "Electron reconstruction and identification efficiency measurements with the ATLAS detector using the 2011 LHC proton–proton collision data". In: *Eur. Phys. J. C* 74 (2014), p. 2941. DOI: 10.1140/epjc/s10052-014-2941-0. arXiv: 1404.2240 [hep-ex]. PERF-2013-03.

[25] ATLAS Collaboration. *Electron efficiency measurements with the ATLAS detector using the 2012 LHC proton–proton collision data*. ATLAS-CONF-2014-032. 2014. URL: https://cds.cern.ch/record/1706245.

[26] ATLAS Collaboration. *Measurements of the photon identification efficiency with the ATLAS detector using 4.9 fb^{-1} of pp collision data collected in 2011*. ATLAS-CONF-2012-123. 2012. URL: https://cds.cern.ch/record/1473426.

[27] ATLAS Collaboration. "Muon reconstruction performance of the ATLAS detector in proton–proton collision data at $\sqrt{s} = 13$ TeV". In: (2016). arXiv: 1603.05598 [hep-ex]. PERF-2015-10.

[28] ATLAS Collaboration. "Topological cell clustering in the ATLAS calorimeters and its performance in LHC Run 1". In: (2016). arXiv: 1603.02934 [hep-ex]. PERF-2014-07.

[29] ATLAS Collaboration. *Properties of jets and inputs to jet reconstruction and calibration with the ATLAS detector using proton–proton collisions at $\sqrt{s}$ = 13 TeV*. ATL-PHYS-PUB-2015-036. 2015. URL: https://cds.cern.ch/record/2044564.

[30] Matteo Cacciari, Gavin P. Salam, and Gregory Soyez. "The anti-k_t jet clustering algorithm". In: *JHEP* 04 (2008), p. 063. DOI: 10.1088/1126-6708/2008/04/063. arXiv: 0802.1189 [hep-ph].

[31] ATLAS Collaboration. *Jet global sequential corrections with the ATLAS detector in proton–proton collisions at $\sqrt{s}$ = 8 TeV*. ATLAS-CONF-2015-002. 2015. URL: https://cds.cern.ch/record/2001682.

[32] S. Agostinelli et al. "GEANT4: A simulation toolkit". In: *Nucl. Instrum. Meth. A* 506 (2003), pp. 250–303. DOI: 10.1016/S0168-9002(03)01368-8.

[33] ATLAS Collaboration. "A study of the material in the ATLAS inner detector using secondary hadronic interactions". In: *JINST* 7 (2012), P01013. DOI: 10.1088/1748-0221/7/01/P01013. arXiv: 1110.6191 [hep-ex]. PERF-2011-08.

[34] ATLAS Collaboration. "Electron and photon energy calibration with the ATLAS detector using LHC Run 1 data". In: *Eur. Phys. J. C* 74 (2014), p. 3071. DOI: 10.1140/epjc/s10052-014-3071-4. arXiv: 1407.5063 [hep-ex]. PERF-2013-05.

[35] ATLAS Collaboration. "A measurement of the calorimeter response to single hadrons and determination of the jet energy scale uncertainty using LHC Run-1 pp-collision data with the ATLAS detector". In: (2016). arXiv: 1607.08842 [hep-ex]. PERF-2015-05.

[36] ATLAS Collaboration. "Single hadron response measurement and calorimeter jet energy scale uncertainty with the ATLAS detector at the LHC". In: *Eur. Phys. J. C* 73 (2013), p. 2305. DOI: 10.1140/epjc/s10052-013-2305-1. arXiv: 1203.1302 [hep-ex]. PERF-2011-05.

[37] ATLAS Collaboration. "The ATLAS Simulation Infrastructure". In: *Eur. Phys. J. C* 70 (2010), p. 823. DOI: 10.1140/epjc/s10052-010-1429-9. arXiv: 1005.4568 [hep-ex]. SOFT-2010-01.

[38] T. Sjöstrand, S. Mrenna, and P. Skands. "A Brief Introduction to PYTHIA 8.1". In: *Comput. Phys. Commun.* 178 (2008), pp. 852–867. DOI: 10.1016/j.cpc.2008.01.036. arXiv: 0710.3820.

[39] ATLAS Collaboration. *Summary of ATLAS Pythia 8 tunes*. ATL-PHYS-PUB-2012-003. 2012. URL: http://cds.cern.ch/record/1474107.

[40] A.D. Martin, W.J. Stirling, R.S. Thorne, and G. Watt. "Parton distributions for the LHC". In: *Eur. Phys. J. C* 63 (2009). Figures from the MSTW Website, pp. 189–285. DOI: 10.1140/epjc/s10052-009-1072-5. arXiv: 0901.0002.

[41] A. Sherstnev and R.S. Thorne. "Parton Distributions for LO Generators". In: *Eur. Phys. J. C* 55 (2008), pp. 553–575. DOI: 10.1140/epjc/s10052-008-0610-x. arXiv: 0711.2473.

[42] A. Ribon et al. *Status of Geant4 hadronic physics for the simulation of LHC experiments at the start of LHC physics program*. CERN-LCGAPP-2010-02. 2010. URL: http://lcgapp.cern.ch/project/docs/noteStatusHadronic2010.pdf.

[43] M. P. Guthrie, R. G. Alsmiller, and H. W. Bertini. "Calculation of the capture of negative pions in light elements and comparison with experiments pertaining to cancer radiotherapy". In: *Nucl. Instrum. Meth.* 66 (1968), pp. 29–36. DOI: 10.1016/0029-554X(68)90054-2.

[44] H. W. Bertini and P. Guthrie. "News item results from medium-energy intranuclear-cascade calculation". In: *Nucl. Instr. and Meth. A* 169 (1971), p. 670. DOI: 10.1016/0375-9474(71)90710-X.

[45] V.A. Karmanov. "Light Front Wave Function of Relativistic Composite System in Explicitly Solvable Model". In: *Nucl. Phys. B* 166 (1980), p. 378. DOI: 10.1016/0550-3213(80)90204-7.

[46] H. S. Fesefeldt. *GHEISHA program*. Pitha-85-02, Aachen. 1985.

[47] G. Folger and J.P. Wellisch. "String parton models in Geant4". In: (2003). arXiv: nucl-th/0306007.

[48] N. S. Amelin et al. "Transverse flow and collectivity in ultrarelativistic heavy-ion collisions". In: *Phys. Rev. Lett.* 67 (1991), p. 1523. DOI: 10.1103/PhysRevLett.67.1523.

[49] N. S. Amelin et al. "Collectivity in ultrarelativistic heavy ion collisions". In: *Nucl. Phys. A* 544 (1992), p. 463. DOI: 10.1016/0375-9474(92)90598-E.

[50] L. V. Bravina et al. "Fluid dynamics and Quark Gluon string model - What we can expect for Au+Au collisions at 11.6 AGeV/c". In: *Nucl. Phys. A* 566 (1994), p. 461. DOI: 10.1016/0375-9474(94)90669-6.

[51] L. V. Bravin et al. "Scaling violation of transverse flow in heavy ion collisions at AGS energies". In: *Phys. Lett. B* 344 (1995), p. 49. DOI: 10.1016/0370-2693(94)01560-Y.

[52] B. Andersson et al. "A model for low-pT hadronic reactions with generalizations to hadron-nucleus and nucleus-nucleus collisions". In: *Nucl. Phys. B* 281 (1987), p. 289. DOI: 10.1016/0550-3213(87)90257-4.

[53] B. Andersson, A. Tai, and B.-H. Sa. "Final state interactions in the (nuclear) FRITIOF string interaction scenario". In: *Z. Phys. C* 70 (1996), pp. 499–506. DOI: 10.1007/s002880050127.

[54] B. Nilsson-Almqvist and E. Stenlund. “Interactions Between Hadrons and Nuclei: The Lund Monte Carlo, Fritiof Version 1.6”. In: *Comput. Phys. Commun.* 43 (1987), p. 387. doi: 10.1016/0010-4655(87)90056-7.

[55] B. Ganhuyag and V. Uzhinsky. “Modified FRITIOF code: Negative charged particle production in high energy nucleus nucleus interactions”. In: *Czech. J. Phys.* 47 (1997), pp. 913–918. doi: 10.1023/A:1021296114786.

[56] ATLAS Collaboration. “Topological cell clustering in the ATLAS calorimeters and its performance in LHC Run 1”. In: (2016). arXiv: 1603.02934 [hep-ex].

[57] Peter Speckmayer. “Energy Measurement of Hadrons with the CERN ATLAS Calorimeter”. Presented on 18 Jun 2008. PhD thesis. Vienna: Vienna, Tech. U., 2008. url: http://cds.cern.ch/record/1112036.

[58] CMS Collaboration. “The CMS barrel calorimeter response to particle beams from 2 to 350 GeV/c”. In: *Eur. Phys. J. C* 60.3 (2009). doi: 10.1140/epjc/s10052-009-0959-5.

[59] J. Beringer et al. (Particle Data Group). “Review of Particle Physics”. In: *Chin. Phys. C* 38 (2014), p. 090001. url: http://pdg.lbl.gov.

[60] P. Adragna et al. “Measurement of Pion and Proton Response and Longitudinal Shower Profiles up to 20 Nuclear Interaction Lengths with the ATLAS Tile Calorimeter”. In: *Nucl. Instrum. Meth. A* 615 (2010), pp. 158–181. doi: 10.1016/j.nima.2010.01.037.

[61] ATLAS Collaboration. “Jet energy measurement and its systematic uncertainty in proton–proton collisions at $\sqrt{s} = 7$ TeV with the ATLAS detector”. In: *Eur. Phys. J. C* 75 (2015), p. 17. doi: 10.1140/epjc/s10052-014-3190-y. arXiv: 1406.0076 [hep-ex]. PERF-2012-01.

[62] Hung-Liang Lai, Marco Guzzi, Joey Huston, Zhao Li, Pavel M. Nadolsky, et al. “New parton distributions for collider physics”. In: *Phys. Rev. D* 82 (2010), p. 074024. doi: 10.1103/PhysRevD.82.074024. arXiv: 1007.2241 [hep-ph].

[63] E. Abat et al. “Study of energy response and resolution of the ATLAS barrel calorimeter to hadrons of energies from 20 to 350 GeV”. In: *Nucl. Instrum. Meth. A* 621.1-3 (2010), pp. 134 –150. doi: http://dx.doi.org/10.1016/j.nima.2010.04.054.

[64] ATLAS Collaboration. “Jet energy measurement with the ATLAS detector in proton–proton collisions at $\sqrt{s} = 7$ TeV”. In: *Eur. Phys. J. C* 73 (2013), p. 2304. doi: 10.1140/epjc/s10052-013-2304-2. arXiv: 1112.6426 [hep-ex]. PERF-2011-03.

[65] Nausheen R. Shah and Carlos E. M. Wagner. “Gravitons and dark matter in universal extra dimensions”. In: *Phys. Rev.* D74 (2006), p. 104008. doi: 10.1103/PhysRevD.74.104008. arXiv: hep-ph/0608140 [hep-ph].

[66] Jonathan L. Feng, Arvind Rajaraman, and Fumihiro Takayama. "Graviton cosmology in universal extra dimensions". In: *Phys. Rev.* D68 (2003), p. 085018. DOI: 10.1103/PhysRevD.68.085018. arXiv: hep-ph/0307375 [hep-ph].

[67] Paul H. Frampton and Pham Quang Hung. "Long-lived quarks?" In: *Phys. Rev. D* 58 (5 1998), p. 057704. DOI: 10.1103/PhysRevD.58.057704. URL: http://link.aps.org/doi/10.1103/PhysRevD.58.057704.

[68] C. Friberg, E. Norrbin, and T. Sjostrand. "QCD aspects of leptoquark production at HERA". In: *Phys. Lett.* B403 (1997), pp. 329–334. DOI: 10.1016/S0370-2693(97)00543-1. arXiv: hep-ph/9704214 [hep-ph].

[69] Herbert K. Dreiner. "An introduction to explicit R-parity violation". In: (1997). arXiv: hep-ph/9707435.

[70] Edmond L. Berger and Zack Sullivan. "Lower limits on R-parity-violating couplings in supersymmetry". In: *Phys. Rev. Lett.* 92 (2004), p. 201801. DOI: 10.1103/PhysRevLett.92.201801. arXiv: hep-ph/0310001.

[71] R. Barbieri, C. Berat, M. Besancon, M. Chemtob, A. Deandrea, et al. "R-parity violating supersymmetry". In: *Phys. Rept.* 420 (2005), p. 1. DOI: 10.1016/j.physrep.2005.08.006. arXiv: hep-ph/0406039.

[72] M. Fairbairn et al. "Stable massive particles at colliders". In: *Phys. Rept.* 438 (2007), p. 1. DOI: 10.1016/j.physrep.2006.10.002. arXiv: hep-ph/0611040.

[73] Christopher F. Kolda. "Gauge-mediated supersymmetry breaking: Introduction, review and update". In: *Nucl. Phys. Proc. Suppl.* 62 (1998), p. 266. DOI: 10.1016/S0920-5632(97)00667-1. arXiv: hep-ph/9707450.

[74] Howard Baer, Kingman Cheung, and John F. Gunion. "A Heavy gluino as the lightest supersymmetric particle". In: *Phys. Rev. D* 59 (1999), p. 075002. DOI: 10.1103/PhysRevD.59.075002. arXiv: hep-ph/9806361.

[75] S. James Gates Jr. and Oleg Lebedev. "Searching for supersymmetry in hadrons". In: *Phys. Lett. B* 477 (2000), p. 216. DOI: 10.1016/S0370-2693(00)00172-6. arXiv: hep-ph/9912362.

[76] Glennys R. Farrar and Pierre Fayet. "Phenomenology of the Production, Decay, and Detection of New Hadronic States Associated with Supersymmetry". In: *Phys. Lett.* B76 (1978), pp. 575–579. DOI: 10.1016/0370-2693(78)90858-4.

[77] A. C. Kraan, J. B. Hansen, and P. Nevski. "Discovery potential of R-hadrons with the ATLAS detector". In: *Eur. Phys. J.* C49 (2007), pp. 623–640. DOI: 10.1140/epjc/s10052-006-0162-x. arXiv: hep-ex/0511014 [hep-ex].

[78] Rasmus Mackeprang and David Milstead. "An Updated Description of Heavy-Hadron Interactions in GEANT-4". In: *Eur. Phys. J.* C66 (2010), pp. 493–501. DOI: 10.1140/epjc/s10052-010-1262-1. arXiv: 0908.1868 [hep-ph].

[79] ATLAS Collaboration. "Search for massive, long-lived particles using multitrack displaced vertices or displaced lepton pairs in pp collisions at $\sqrt{s} = 8$ TeV with the ATLAS detector". In: *Phys. Rev. D* 92 (2015), p. 072004. DOI: 10.1103/PhysRevD.92.072004. arXiv: 1504.05162 [hep-ex]. SUSY-2014-02.

[80] ATLAS Collaboration. "Search for charginos nearly mass degenerate with the lightest neutralino based on a disappearing-track signature in pp collisions at $\sqrt{s} = 8$ TeV with the ATLAS detector". In: *Phys. Rev. D* 88 (2013), p. 112006. DOI: 10.1103/PhysRevD.88.112006. arXiv: 1310.3675 [hep-ex]. SUSY-2013-01.

[81] ATLAS Collaboration. "Searches for heavy long-lived sleptons and R-Hadrons with the ATLAS detector in pp collisions at $\sqrt{s} = 7$ TeV". In: *Phys. Lett. B* 720 (2013), p. 277. DOI: 10.1016/j.physletb.2013.02.015. arXiv: 1211.1597 [hep-ex]. SUSY-2012-01.

[82] ATLAS Collaboration. "Searches for heavy long-lived charged particles with the ATLAS detector in proton–proton collisions at $\sqrt{s} = 8$ TeV". In: *JHEP* 01 (2015), p. 068. DOI: 10.1007/JHEP01(2015)068. arXiv: 1411.6795 [hep-ex]. SUSY-2013-22.

[83] ATLAS Collaboration. "Search for metastable heavy charged particles with large ionisation energy loss in pp collisions at $\sqrt{s} = 8$ TeV using the ATLAS experiment". In: *Eur. Phys. J. C* 75 (2015), p. 407. DOI: 10.1140/epjc/s10052-015-3609-0. arXiv: 1506.05332 [hep-ex]. SUSY-2014-09.

[84] ATLAS Collaboration. "Search for heavy long-lived charged R-hadrons with the ATLAS detector in 3.2 fb^{-1} of proton–proton collision data at $\sqrt{s} = 13$ TeV". In: *Phys. Lett.* B760 (2016), pp. 647–665. DOI: 10.1016/j.physletb.2016.07.042. arXiv: 1606.05129 [hep-ex].

[85] Torbjorn Sjöstrand, Stephen Mrenna, and Peter Skands. "PYTHIA 6.4 Physics and Manual". In: *JHEP* 0605 (2006), p. 026. DOI: 10.1088/1126-6708/2006/05/026. arXiv: hep-ph/0603175.

[86] ATLAS Collaboration. *Further ATLAS tunes of Pythia 6 and Pythia 8*. ATL-PHYS-PUB-2011-014. 2011. URL: https://cds.cern.ch/record/1400677.

[87] Aafke Christine Kraan. "Interactions of heavy stable hadronizing particles". In: *Eur. Phys. J.* C37 (2004), pp. 91–104. DOI: 10.1140/epjc/s2004-01946-6. arXiv: hep-ex/0404001 [hep-ex].

[88] M. Fairbairn et al. "Stable massive particles at colliders". In: *Phys. Rept.* 438 (2007), p. 1. DOI: 10.1016/j.physrep.2006.10.002. arXiv: hep-ph/0611040.

[89] W. Beenakker, R. Hopker, M. Spira, and P. M. Zerwas. "Squark and gluino production at hadron colliders". In: *Nucl. Phys. B* 492 (1997), p. 51. DOI: 10.1016/S0550-3213(97)00084-9. arXiv: hep-ph/9610490.

[90] A. Kulesza and L. Motyka. “Threshold resummation for squark-antisquark and gluino-pair production at the LHC”. In: *Phys. Rev. Lett.* 102 (2009), p. 111802. DOI: 10.1103/PhysRevLett.102.111802. arXiv: 0807.2405 [hep-ph].

[91] A. Kulesza and L. Motyka. “Soft gluon resummation for the production of gluino-gluino and squark-antisquark pairs at the LHC”. In: *Phys. Rev. D* 80 (2009), p. 095004. DOI: 10.1103/PhysRevD.80.095004. arXiv: 0905.4749 [hep-ph].

[92] Wim Beenakker, Silja Brensing, Michael Kramer, Anna Kulesza, Eric Laenen, et al. “Soft-gluon resummation for squark and gluino hadroproduction”. In: *JHEP* 0912 (2009), p. 041. DOI: 10.1088/1126-6708/2009/12/041. arXiv: 0909.4418 [hep-ph].

[93] W. Beenakker, S. Brensing, M.n Kramer, A. Kulesza, E. Laenen, et al. “Squark and Gluino Hadroproduction”. In: *Int. J. Mod. Phys. A* 26 (2011), p. 2637. DOI: 10.1142/S0217751X11053560. arXiv: 1105.1110 [hep-ph].

[94] Michael Krämer et al. *Supersymmetry production cross sections in pp collisions at* $\sqrt{s} = 7$ *TeV*. 2012. arXiv: 1206.2892 [hep-ph].

[95] Rasmus Mackeprang and Andrea Rizzi. “Interactions of Coloured Heavy Stable Particles in Matter”. In: *Eur. Phys. J.* C50 (2007), pp. 353–362. DOI: 10.1140/epjc/s10052-007-0252-4. arXiv: hep-ph/0612161 [hep-ph].

[96] Rasmus Mackeprang and David Milstead. “An Updated Description of Heavy-Hadron Interactions in GEANT-4”. In: *Eur. Phys. J.* C66 (2010), pp. 493–501. DOI: 10.1140/epjc/s10052-010-1262-1. arXiv: 0908.1868 [hep-ph].

[97] J. Alwall, R. Frederix, S. Frixione, V. Hirschi, F. Maltoni, O. Mattelaer, H. S. Shao, T. Stelzer, P. Torrielli, and M. Zaro. “The automated computation of tree-level and next-to-leading order differential cross sections, and their matching to parton shower simulations”. In: *JHEP* 07 (2014), p. 079. DOI: 10.1007/JHEP07(2014)079. arXiv: 1405.0301 [hep-ph].

[98] “dE/dx measurement in the ATLAS Pixel Detector and its use for particle identification”. In: (2011).

[99] ATLAS Collaboration. “The ATLAS Simulation Infrastructure”. In: *Eur. Phys. J.* C70 (2010), pp. 823–874. DOI: 10.1140/epjc/s10052-010-1429-9. arXiv: 1005.4568 [physics.ins-det].

[100] Alexander L. Read. “Presentation of search results: The CL(s) technique”. In: *J. Phys.* G28 (2002). [,11(2002)], pp. 2693–2704. DOI: 10.1088/0954-3899/28/10/313.

DECLARATION

Put your declaration here.

Berkeley, CA, September 2016

Bradley Axen

COLOPHON

Not sure that this is necessary.